SISSA
40!

SISSA - International School for Advanced Studies

PhD Thesis

Friction and adhesion of graphene nanoribbons on gold: an MD investigation

Candidate:
Lorenzo Gigli

Supervisors:
prof. Giuseppe Santoro
dott. Andrea Vanossi
prof. Erio Tosatti

Academic year 2018/2019

To my mother

Contents

Preface

The frictional motion of contacting bodies is an ubiquitous phenomenon in physics. It encompasses a vast range of time, energy, and length scales, ranging from the macroscale of earthquakes, down to the nanometer scale of atomically flat surfaces and Atomic Force Microscopy (AFM) experiments [1, 2]. Despite the impressive amount of data that has been obtained through the centuries concerning frictional phenomena, a complete theory of friction is still lacking. The main reason is the fact that the frictional response of an interface is determined by a large number of factors, such as the specific nature and chemistry of the surfaces in contact, the operational conditions, the ageing and the sliding history of the contact [3, 4], just to mention a few of them. Moreover, the presence of out-of-equilibrium and highly non-linear processes often occurring at ill-characterized frictional contacts makes a complete understanding of friction even more challenging [5, 6].

In this context, new opportunities have been brought about by advances in nanotechnology, where the invention of scanning tip instruments of the AFM family [7] enabled a systematic study of friction for well-characterized materials and surfaces at the nanoscale [8, 9, 10, 11].

Progresses in both the computer modeling of interatomic interactions, that made atomistic simulations of nanostructured materials more powerful and reliable [12, 13], and the development in the theory of non-linear processes [5, 14] offered new theoretical tools to understand frictional phenomena. In particular, the difficulty of dealing with extremely complex systems where friction is determined by collective phenomena involving many degrees of freedom, gave a strong impulse to the search of simplified 1D- and 2D-models, such as the Prandtl-Tomlinson (PT) [15, 16, 17] and generalized Frenkel-Kontorova (FK) models [14, 18, 19, 20] to capture the essential ingredients of friction.

To summarize, understanding frictional phenomena at the nanoscale seems of great importance now, since dealing with experimentally well-defined interfaces makes the fundamental mechanisms of friction easier to identify, possibly with the aim of merging the existing gap between nano- and macroscale friction, where many different physical actors are at play. Technological advances in this endeavor are to be considered, since controlling friction could limit wear and dissipation, with possible impacts in improving the performances of nano- and micromachines [21], as well as biological motors [22].

In this general framework, the ongoing experimental and theoretical research on nanoscale friction is covering three central topics. First of all, the study of electronic and quantum effects in friction, which happen whenever a tip or a moving agent dissipates energy by exciting local currents in the sample [2, 3]. Secondly, the study of trapped optical systems, such as driven ion chains and colloids in confined configurations [26, 27], that turned out as elegant experimental realizations of

the Prandtl-Tomlinson and the Frenkel-Kontorova model. These systems are now attracting a lot of interest because of the possibility of tuning the various parameters of the experimental setup, such as temperature, substrate corrugation and degree of commensurability between the sample and the substrate, almost freely.

At last, a very important field of research is represented by the frictional properties of layered and 2D materials, where evidence of a large reduction of friction (up to a factor 10) has been obtained in many graphene-based systems, grown on both amorphous [23, 24, 25] and metallic substrates [28, 29, 30]. The interest for graphene in this field is stimulated by its peculiar tribological features: the decrease of friction by increasing the number of graphene layers [23, 28, 31, 32], the increase of friction upon decreasing the normal load when graphene is chemically modified [33] and the use of graphene as solid lubricant [25].

In this Thesis, we are interested in gaining a deeper insight in the molecular mechanisms of dissipation in a specific type of graphene/metal interface, the graphene nanoribbons (or GNRs) on gold, inspired by the works of Kawai *et al.* [34, 35] regarding their structural and dynamical properties under the action of an external driving.

The papers that represent the basis and core of the Thesis are:

- L. Gigli, N. Manini, A. Benassi, E. Tosatti, A. Vanossi and R. Guerra, *Graphene nanoribbons on gold: understanding superlubricity and edge effects*, 2D Materials, **4**, 4 (2017)
- L. Gigli, N. Manini, E. Tosatti, R. Guerra and A. Vanossi, *Lifted graphene nanoribbons: from smooth sliding to multiple stick-slip regimes*, Nanoscale, **10**, 2073-2080 (2018)
- L. Gigli, S. Kawai, R. Guerra, N. Manini, R. Pawlak, X. Feng, K. Müllen, P. Ruffieux, R. Fasel, E. Tosatti, E. Meyer, A. Vanossi, *Detachment dynamics of graphene nanoribbons on gold*, in press in ACSNano (2018)

The Molecular Simulations that have been used for the papers [36, 37] show that the GNR/gold interface has a very low friction, with basically zero average increase upon increasing the GNR length. This property, called **superlubricity** (see chapter 3), is experimentally very rare and due to the interplay between the large in-plane stiffness of graphene and the incommensurability between the GNR and the gold substrate structure (see chapter 4).

We will show that this system is suitable to obtain a dynamical transition between low-friction smooth sliding states and violent stick-slip regimes by lifting one edge of the GNR at increasing heights, thus changing the effective GNR out-of-plane softness. Furthermore, an external driving of the GNRs along their longitudinal axis directly provides an asymmetric response of the system against pulling/pushing of the edge (see chapter 5).

In the last part of the Thesis, we will analyze the dynamical behavior of the GNRs against vertical pulling and show that an Atomic Force Microscope is able to unveil the detailed structure of the system by producing unilateral detachment of its individual unit cells. A good agreement between the experimentally recorded vertical force traces and the results of the molecular simulations shows that the GNR vertical dynamics is characterized by discrete detachments, accompanied by slips of the tail, which are responsible for the complex double-periodicity observed in the vertical force profile (see chapter 6).

Chapter 1

Introduction and motivations

Nanofriction is the field of condensed matter physics which deals with sliding of nanostructured materials, where the mechanical properties of the system, wear and dissipation are intimately related to the microscopic details of the interface, i.e. the atomic structure, the presence of defects, the lattice constants and the type of interaction between the contacting materials.

In this framework, the present Thesis aims at gaining a deeper insight into the molecular mechanisms involved in nanoscale sliding friction, by focusing on a specific type of graphene/metal interface: the graphene nanoribbons (stripes of H-passivated graphene) deposited on gold.

To understand the experimental motivations of this work and the final results, in this chapter we give a brief introduction of the field of nanofriction and discuss the key theoretical concepts and methods that are currently used in its modeling. The focus is centred on Molecular Dynamics simulations, as they have proven to play a crucial role for the understading of frictional phenomena at the nanoscale and have been extensively used for this Thesis.

1.1 Friction vs. Nano-friction

1.1.1 The Coulomb-Amontons' laws

The first attempts to understand friction between macroscopic objects by means of physical laws date back to the 15th century. With his studies of the rotational resistance of axles and the mechanics of screw threads, Leonardo da Vinci was a pioneer in the study of tribology [38, 39]. Still, it took until the 18th century for Leonardo da Vinci's observations to be synthetized in the so called Amontons' laws of friction [40].

These laws, still in use today to describe the physics of "macroscopic" dry frictional sliding (i.e. without lubrication), can be summarized as follows. First of all, a minimal force - usually called the *static friction force* F_s - is needed to set a rigid body (the slider) in relative motion with respect to a second body (the substrate). Both bodies are initially at rest, with (eventually) the additional action of a normal load (see Fig. 1.1).

A second force - the *kinetic friction force* F_D - is then needed to keep the slider in a state of uniform motion at constant velocity with respect to the substrate. The mechanical work that is generated by the action of this force is then dissipated in the excitation of the internal degrees of

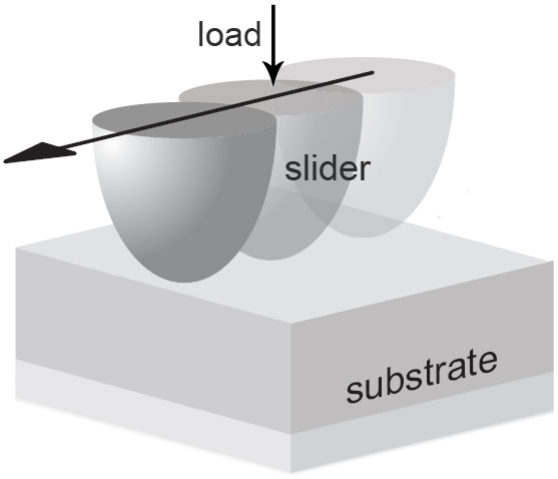

Figure 1.1: Schematic picture of a basic frictional experiment. A body initially at rest (the slider) is set into motion upon a second body (the substrate) by means of an external force, possibly with the action of a normal load.

freedom of the slider and the substrate, i.e. in Joule heat that increases the interfacial temperature.

These forces then obey the following Coulomb-Amontons' laws:

1. the static friction force F_s and the kinetic friction F_D are independent on the apparent area of contact S' between the slider and the substrate;
2. F_s and F_D are proportional to the applied normal load N: $F_s = \mu_s N$ and $F_D = \mu_D N$. The friction coefficients μ_s and μ_D only depend on the specific materials in contact and usually $\mu_s > \mu_D$.
3. the kinetic friction force F_D is independent of the sliding velocity v.

The linear proportionality to N and independence on S' are easy to understand, when we realize that practical surfaces are always rough and the real area of contact S, which is usually composed of a large number of micro-asperities, is much smaller than S' [39, 41, 42].

Both elasticity of the contacting bodies and, at higher contact pressures, their plastic response, imply that the total contact area S is approximately proportional to the total normal load N. A constant shear stress over the area of true contact then makes the friction force F linear in the area of true contact S and therefore also linear in the normal force N.

We should realize that, even for dry friction without wear, the Coulomb-Amontons' laws are no more than approximate. For example, experiments indicate that there is a finite time involved in the formation of micro-contacts between macroscopic bodies, which is derived from the observation of a logarithmic decrease of the friction force with increasing velocity, while the static friction force increases, usually with a logarithmic trend, with the time that the system has been at rest [43].

1.1.2 The breakdown of Amontons' laws at the nanoscale

The Coulomb-Amontons' laws fail when dealing with nanoscale sliding. This is quite clear in many respects, as macroscopic objects in contact are characterized by rough interfaces with a large number of asperities, that make the real area of contact orders of magnitude smaller than

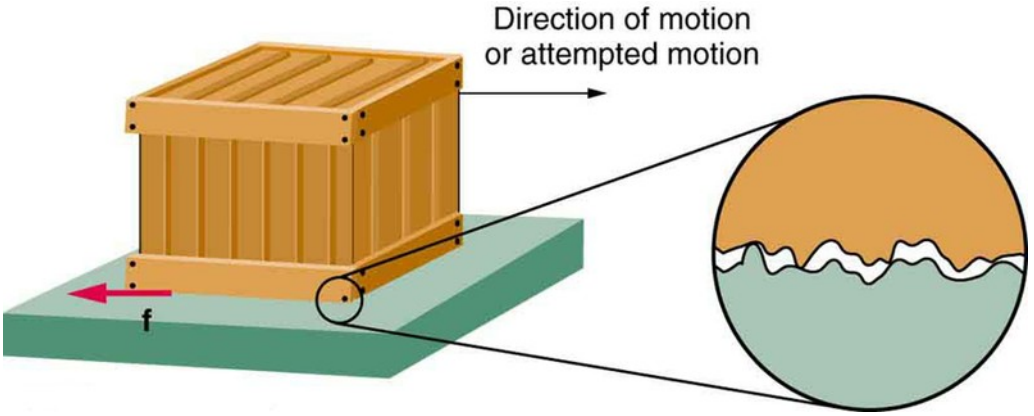

Figure 1.2: A typical macroscale interface. The zoomed-in region shows that the microscopic structure of the contact is characterized by a multitude of asperities, which dominate the frictional response.

the apparent one. As a consequence, the atomic structure and the nature of the microscopic interactions that are involved in the sliding process happen to be completely negligible with respect to the macroscopic interlockings and the deformations of those asperities.

It is in fact not surprising that the first attempts to formulate the problem of macroscopic friction with a rigorous but still simple mathematical approach, which date back to Bowden and Tabor's work [41] in 1939, used a model system characterized by randomly distributed asperities with a spherical shape.

Instead, when we deal with friction at the nanoscale, many other effects come into play. With the advent of the Atomic and Friction Force Microscope (AFM and FFM) [7] and the Surface Forces Apparatus (SFA) [44], it has become possible to explore on the molecular level the physical mechanisms operating at real sliding contacts. Particularly relevant was the possibility of directly measuring the applied lateral and normal force on atomically flat surfaces in the sliding process [6], to have a direct test of Amontons' laws for a large class of materials.

Results of the latest experimental works have shown large deviations from Coulomb-Amontons' laws in many respects. For instance, a non-linear dependence of the static friction force on the normal load has been found in [45, 46], a dependence of the kinetic friction of the tip of an FFM on the sliding velocity has been reported in [47] on a substrate of mica and on Sodium-Chloride [48]. Moreover, there are strong evidences of a dependence of the static friction force on the contact size in most nanoscale investigations [53, 54, 55]. A systematic investigation of the dependence of friction on the contact area was carried out recently for nano-sized metal clusters on graphite in ultraclean and even atmospheric conditions [56, 57], whose results indicate a size dependence of kinetic friction at very low speed which is scattered. For certain clusters, a linear scaling with area is observed, while others can be grouped in sets compatible with sublinear scaling.

These deviations from the macroscopic laws of friction are due to the fact that in nanoscale experiments the roughness of the surfaces and the interlockings between microasperities are not the main actors any more. Instead, the structural lattice mismatch between the contacting materials, generating commensurate or incommensurate configurations, their in-plane stiffness and the corrugation potential generated by the lattice structure of the substrate are dominating the frictional response and the scaling laws of static and kinetic friction [2, 56]. In this context, the study

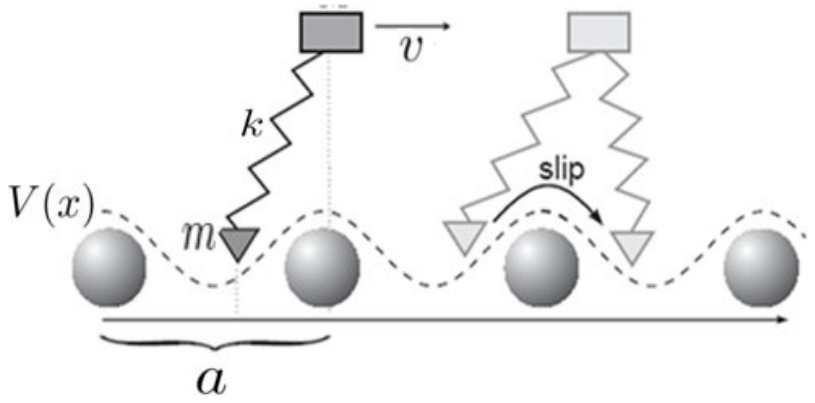

Figure 1.3: Schematic representation of the PT model.

of simplified 1D and 2D models, such as the Prandtl-Tomlinson (PT) and the Frenkel-Kontorova (FK) model (see Sec. 1.2), that explain these features with simple physical arguments has reached a great level of interest.

1.2 Modeling the physics of nanofriction

1.2.1 The Prandtl-Tomlinson model

Among the minimalistic models that are currently used to describe nanoscale friction, the Prandtl-Tomlinson (PT) model [15, 16] is so far the most successful and influential. In particular, it addresses the problem of an AFM tip which is dragged along a surface, as it is done in nanoscale experiments, to describe the dynamical states that it may reach in the sliding process.

The PT model assumes that a point mass m (mimicking the AFM tip) is dragged over a sinusoidal corrugation potential $V(x)$ representing the interaction between the tip and a crystalline substrate. The point tip is pulled by a spring of effective elastic constant k representing the cantilever stiffness which moves with constant velocity v relative to the substrate (see Fig. 1.3).

The total (time-dependent) potential experienced by the tip is then given by

$$U(x,t) = V_0 \cos\left(\frac{2\pi x}{a}\right) + \frac{k}{2}\left(x - vt\right)^2 \tag{1.1}$$

where V_0 is the amplitude of the corrugation potential and a the lattice constant of the substrate (see Fig. 1.3).

The instantaneous lateral (kinetic) friction force measured in FFM experiments is equal to the instantaneous harmonic force $F_{\mathrm{k}}(t) = \frac{k}{2}(x - vt)$ applied to the tip. In realistic experimental setups in fact, the work provided by the moving AFM is converted, through the motion of the tip against the corrugation potential, into phononic modes of the substrate and other system excitations. These modes are eventually subject to dissipation into the substrate bulk.

The PT model predicts two different modes for the tip motion, depending on the dimensionless parameter

$$\eta = \frac{4\pi^2 V_0}{k a^2} \tag{1.2}$$

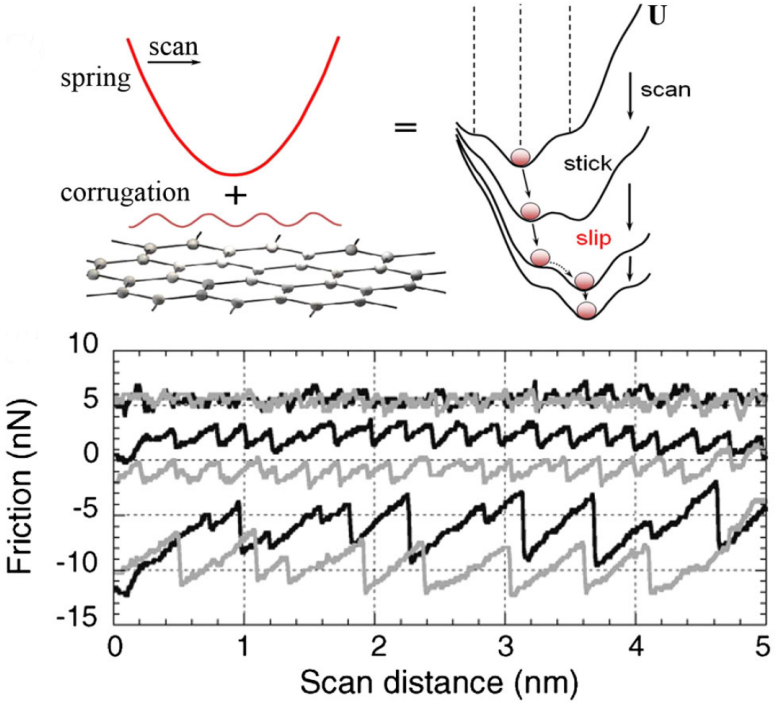

Figure 1.4: The upper panel shows the shape of the total potential experienced by the tip, given by the sum of the harmonic potential and the corrugation potential of the substrate. The lower panel shows typical lateral forces for increasing loads that are recorded in experiments, in agreement with the phenomenology of the PT model: there is a transition from smooth sliding (top) to a stick-slip motion, with single (middle) and double slips (bottom) [61].

which represents the ratio between the strength of the interaction of the tip with the substrate and the stiffness of the driving spring.

When $\eta < 1$ the total potential $U(x,t)$ has only one minimum and the tip is continuously following this minimum in the sliding dynamics. The tip is then performing a **smooth-sliding** motion.

Instead, when $\eta > 1$, two or more minima can appear in the total potential. The result is that the tip can remain stuck in one minimum for a given time interval. In the same lapse of time, the spring is elongating and the strength of the harmonic potential is increasing, until the initial metastable state becomes unstable. At this point the tip slips very fast to the new minimum (see upper panel of Fig. 1.4). The result is the so called **stick-slip** motion, which either takes place through slips of one lattice site of the substrate potential (single-slip) or an integer number of lattice sites (multiple-slip), depending on the specific value of η. In particular, the transition between the smooth-sliding state and the stick-slip motion happens for $\eta = 1$, while the possibility of observing slips of higher multiplicity occurs for values of $\eta > 4.604$ [61].

In experiments, signatures of a transition between smooth sliding and stick-slip motion (in wearless conditions) are obtained by applying a normal load to the contact, which effectively changes the corrugation potential (leaving the contact stiffness unaltered) and the value of η accordingly. FFM experiments at low normal loads indeed show that a smooth-sliding state with ultralow friction can be achieved, due to the absence of the elastic instabilities that generate multiple minima in the total energy landscape. At higher loads instead, "atomic" stick-slip takes place with the atomic periodicity of the substrate lattice, while incresing the load further leads to multiple-slip regimes [62].

As shown in Fig. 1.4 evidences of a stick-slip motion can be obtained from the shape of the force trace measured by the FFM. While increasing the normal load, the average value of the force is increasing, indicating a state with larger kinetic friction, and the profile shows a transition between a smooth behavior and saw-tooth behavior with sharp drops that mark the instants of slip. These dynamical states will also be shown in the case of interest of this Thesis (GNRs on gold), where the transition between the smooth sliding and the stick-slip motion is accompanied by an increase in the GNR softness as one of its ends is lifted up to increasing heights [37].

So far considered, the PT model does not take into account the effect of thermal fluctuations. Still, especially when dealing with very low sliding velocities, thermal effects are not negligible, as the elastic instabilities predicted by the PT model and the effective energy barriers for the slips of the particle are mitigated by thermal activation. We can include these effects in the PT model, by describing the dynamics of the point tip with a Langevin equation at finite temperature

$$m\ddot{x} + m\gamma\dot{x} = -\frac{\partial U(x,t)}{\partial x} + \hat{f}(t) \tag{1.3}$$

where $-m\gamma\dot{x}$ is a damping term that mimicks dissipation due to interactions with the internal degrees of freedom of the substrate (not explicitly treated) and $\hat{f}(t)$ is a random force that satisfies the fluctuation-dissipation theorem, i.e. it has zero average $< \hat{f}(t) >= 0$ and is δ-correlated in time:

$$\left\langle \hat{f}(t)\hat{f}(t') \right\rangle = 2m\gamma k_b T\delta(t-t') \tag{1.4}$$

where k_b is the Boltzmann constant and T is the temperature.

In the thermal PT model, described by Eqs. (1.3) and (1.4), thermal fluctuations bring out a new dimensionless parameter

$$\delta = \frac{v}{a\omega_0} \exp\left(\frac{V_0}{k_b T}\right) = \frac{\nu}{\nu_k} \tag{1.5}$$

representing the ratio between the pulling rate $\nu = v/a$ and the characteristic 'Kramers' rate of thermally activated jumps over the potential barriers $\nu_k = \omega_0 \exp(-V_0/k_b T)$ [63].

As a result, one should distinguish between two different regimes of motion:

- $\delta \ll 1$, regime of very low velocities or high temperatures, where the tip has enough time to jump back and forth across the barriers by thermal activation. In this regime, the kinetic friction is described the following law:

  $$F_{\mathrm{k}}(v, T) = \alpha(T) v + O(v^3) \tag{1.6}$$

  as suggested in [63, 64].

  Therefore the temperature dependence of the kinetic friction is such that it vanishes for $v \to 0$, a regime usually called thermolubricity.

- $\delta \gg 1$, regime of high velocities or low temperature, where thermal effects only occasionally assist the tip to cross the barrier before the elastic instabilities occur. In this regime instead, the scaling law of the kinetic friction vs. velocity is such that

  $$F_{\mathrm{k}}(v, T) = F_0 - bT^{2/3} \ln^{2/3}\left(B\frac{T}{v}\right) \tag{1.7}$$

  with $v < BT$ [65]. The kinetic friction thus tends to a finite value for $T \to 0$.

This theoretical framework has explained a number of FFM experimental results on single crystal surfaces [47, 48]. In particular, atomic stick-slip in FFM experiments has been observed at low but still finite temperatures, confirming the idea that the overall dynamics is characterized by thermally-activated slips.

Eq. (1.7) suggests that thermal effects lead to a decrease of the kinetic friction $F_{\mathrm{k}}(v, T)$ at fixed v. Recent experiments [49, 50] however exhibit a peak at cryogenic temperatures for different classes of materials, including amorphous, crystalline, and layered surfaces.

Recent studies based on generalizations of the thermal PT model [51, 52] demonstrated that the friction force may indeed exhibit a peak in the interval of temperatures corresponding to a transition from a multiple-slip regime of motion, at low T, to the single-slip regime at higher T. In this picture, interplay between thermally activated jumps over potential barriers and the reduction of the slip spatial extension with T may lead to a nonmonotonic temperature dependence of friction.

1.2.2 The Frenkel-Kontorova model

The Frenkel-Kontorova (FK) model is the simplest model used in the context of nanofriction to describe the sliding dynamics of crystalline interfaces. Despite its simplicity, it has been introduced to describe a variety of non-linear phenomena, such as the propagation of charge-density

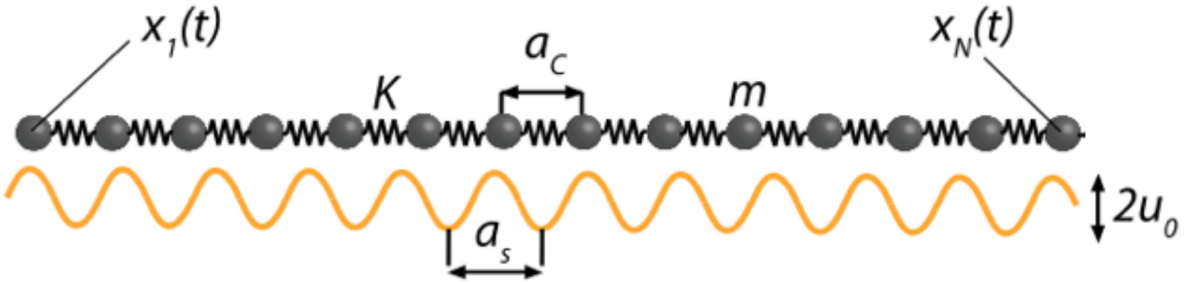

Figure 1.5: The FK model.

waves, dislocation in solids, commensurate-to-incommensurate phase transitions and the presence of domain-walls in magnetically ordered structures [14].

Here we briefly summarize the main features of the 1D FK model, whose main predictions are well confirmed in our case study of graphene nanoribbons on gold [36, 37], as we will point out in chapter 4 and 5.

The standard FK model describes a 1D linear chain of N harmonically coupled "classical" atoms subject to a sinusoidal potential (see Fig. 1.5). The hamiltonian is thus given by

$$H = \sum_{i=1}^{N} \left[\frac{m}{2}\dot{x}_i^2 + \frac{K}{2}(x_{i+1} - x_i - a_c)^2 + u_0 \cos\left(\frac{2\pi x_i}{a_s}\right) \right] \tag{1.8}$$

The first term in eq. (1.8) describes the total kinetic energy of the chain, the second one describes the harmonic interactions between nearest-neighbours in the chain with elastic constant K and equilibrium distance a_c. The last term describes the corrugation potential, which is periodic with lattice constant a_s and depth u_0. Let

$$\eta = K a_c^2 / u_0 \tag{1.9}$$

be the ratio between the stiffness of the chain and the corrugation potential of the substrate.

In this context, static friction is probed by driving all atoms with an extra adiabatically increasing force F until sliding initiates.

A crucial role in the FK model is played by **incommensurability**. Let the substrate period a_s and the period of the chain a_c be such that, in the limit of an infinite system's length, their ratio $\theta = a_s/a_c$ is an irrational number. This case corresponds in realistic interfaces to mismatched lattice spacings between two crystalline materials.

In this case, there exists a critical value of η, or equivalently a critical value of the chain stiffness K for a fixed corrugation u_0, such that the static friction F_s vanishes for $\eta > \eta_C$ (or $K > K_c$) and the kinetic friction becomes very small. This phenomenon is known as the *Aubry transition* [66, 67, 68, 69].

The great practical importance that the existence of this transition has achieved in the field of nanotribology since its discovery lies on the fact that it addresses the concept of **superlubricity**, the property for which the static friction for stiff and incommensurate interfaces increases with a power that is lower than one (sublinear scaling) with the contact area (see chapter 3).

This effect can be understood as follows. If the chain stiffness is sufficiently large, the chain will

not undergo significant deformations as a result of the interaction with the substrate. Moreover, since the chain and the substrate periodicities are mismatched, each particle of the chain in the ground state will sample a different phase of the substrate, from the minima up to the maxima. As a result, lateral forces acting on the particles cancel out and the chain slides for an arbitrarily small applied force (superlubric state). A detailed explanation on this delicate mechanism of lateral force cancellation will be given in Sec. 3.2.

The precise value of η_C that determines the Aubry transition strongly depends on the incommensurability ratio θ, defining the interface. It has been shown mathematically that the minimum value of η_C is reached for the irrational golden mean ratio

$$\theta = \frac{1+\sqrt{5}}{2} \tag{1.10}$$

In the case of a *commensurate* configuration, which takes place whenever θ is a rational number, this cancellation of lateral forces fails, since there exists a common periodicity between the substrate potential and the chain. In other words, there always exists a pair of integer numbers N and M, such that $Na_c = Ma_s$, so that the sampling of the phases of the substrate is not uniform any more. The static friction force F_s then becomes finite.

The static friction still remains finite in the case of an incommensurate configuration but below the Aubry critical point, i.e. for $\eta < \eta_C$. In this case in fact the strength of the corrugation potential is large compared to the chain stiffness, so the chain undergoes important elastic deformations with respect to its unperturbed state as a result of the interaction with the substrate; consequently there will be zero probability of finding particles close the maxima of the substrate potential, resulting in a finite static friction [70].

So far, we have described the static properties of the FK model, but it is worth recalling the basic predictions of the model when the applied force F overcomes the static friction barrier ($F > F_s$), i.e. when depinning of the chain occurs.

The dynamics of the system after depinning is mainly ruled by non-linear excitations of the chain, the so called *solitons*. Consider for instance the simple case of a commensurate ground state, where the number of atoms of the chain is equal to the number of minima of the substrate potential ($\theta = 1$). In this case adding/substracting one atom in the chain results in a configuration with one kink/antikink, i.e. a local compression/extension of the chain separating two regions that are locally commensurate with the substrate. If there is a non-zero probability of finding particles of the chain on the maxima of the substrate potential, these kinks are unpinned and can move along the chain with an arbitrarily small applied force, otherwise they are pinned and generate a static friction barrier [70].

The kinks move along the chain far more easily than atoms in the chain, since their activation energy, the so called Peierls-Nabarro barrier ϵ_{PN}, is much smaller than the corrugation potential u_0. Even for perfectly commensurate configurations, the first step to initiate sliding in a FK chain is the creation of a kink-antikink pair, e.g. by thermal activation. Once depinned, the kink and the antikink start to move along the chain in opposite directions with a velocity which is much larger than the overall sliding speed. One complete run of the kink along the chain results in a total displacement of the chain equal to one lattice spacing of the substrate a_s.

The type of motion that results from the propagation of a kink-antikink pair depends on the

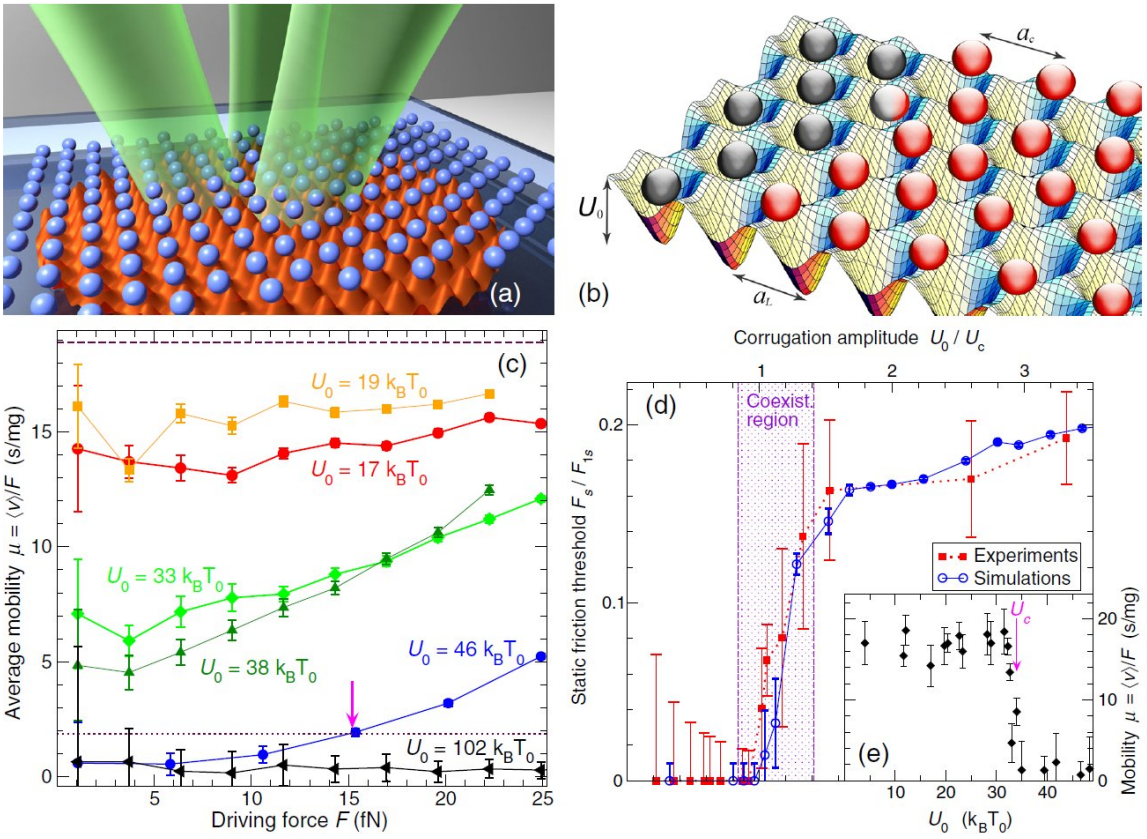

Figure 1.6: Observation of the Aubry transition in a incommensurate colloidal monolayer of micron-sized polystyrene particles in an optical lattice [73]. Panel (a) shows a sketch of the experimental setup and (b) the simulated model. Panel (c) shows the dependence of the measured average mobility of the monolayer $< \mu >= v/F$ on the driving force F for different values of the corrugation potential. Three different regimes are highlighted: the red and orange symbols correspond to a superlubric state, for which the mobility is large even for $F \to 0$. The blue and black symbols correspond to a statically pinned state ($\mu \to 0$ for $F_s \to 0$) and the green symbols to a state of coexistence of pinned and unpinned regions. Panel (d) shows the behavior of the static friction for increasing corrugation in the experiments and theoretical predictions; the shaded area marks the coexistence region across which the Aubry transition takes place.

static friction barrier. In fact, if $\eta > \eta_C$ (above the Aubry transition) the kinks are unpinned and free to move and the depinned state of the chain is a steady smooth sliding state; if the interface is commensurate or $\eta < \eta_C$, the kinks experience a finite Peierls-Nabarro barrier and the result is a spatially non-uniform dynamics, where the inhomogeneity is determined by the solitonic structure.

A direct test of the predictions of the FK model has recently become possible (since 2011) thanks to the experimental micromanipulation of colloidal monolayers.

In particular, the use of interfering laser beams to create trapping optical lattices, as shown in panels (a) and (b) of Fig. 1.6 for charged polystyrene particles has brought up the brand new opportunity of tuning the corrugation potential and the lattice periodicity of the substrate to directly observe the presence of kinks and antikinks in an incommensurate 2D monolayer [26] and to detect signatures of the Aubry transition [73].

Fig. 1.6 shows the results obtained in the measurement of the monolayer average mobility $< \mu >= v/F$ as a function of the driving force F, for increasing values of the corrugation potential

u_0, as well as the static friction force F_s as a function of u_0. v in this case represents the velocity that the slider reaches in the steady state after depinning has occured.

The static friction force profile shows that, in this 2D incommensurate case, the static friction force F_s decreases by decreasing u_0 and vanishes for a finite value of u_0, with a first-order phase transition. The dashed region in panel (d) highlights the presence a coexistence phase within which the static friction grows up finite and the Aubry transition takes place.

These results are confirmed by the behavior of the average mobility. For the superlubric state (region where $F_s(u_0) = 0$) the mobility is in fact finite even for $F \to 0$ (see red and orange symbols of panel (c)). On the other hand, the black and blue symbols correspond to a pinned state, as the corrugation is large and the mobility vanishes for small values of F. The green curves represent an intermediate regime, corresponding to the coexistence phase.

Further experimental observations of superlubric states in 2D layered and graphene-based interfaces that are relevant for this Thesis will be described in chapter 3.

1.2.3 Molecular Dynamics Simulations

The minimalistic models that we have introduced in Secs. 1.2.1 and 1.2.2 provide useful tools to understand many aspects of friction. To address subtler features, such as the dependence of the static and kinetic friction forces on the temperature, the relation between the frictional response and the intrinsic properties of the materials in contact, such as their in-plane or bending elasticity, one has to account for the precise atomic structure of the interface. Such an approach is provided by Molecular Dynamics (MD) Simulations.

The advantage of Molecular Dynamics is that it provides a realistic modeling of the systems that are chemically synthetized in experiments, but at the same time it allows to monitor many microscopic physical quantities that are not accessible in the experimental setups. It is then possible to relate the frictional response of the system to its atomistic dynamics, providing insight in the fundamental understanding of nanofriction.

MD (classical) simulations represent controlled computational experiments where the dynamics of all atoms is obtained by numerically solving Newton or Langevin equations of motion based on suitable interaction potentials and the corresponding interatomic forces [12]. In other words, the system is modelled by means of a total potential energy function of the form

$$U = U(\vec{r}, \vec{r_1}, \vec{r_2}, ..., \vec{r_N}) \tag{1.11}$$

which depends on all-atom coordinates $\vec{r_i}$ $(i = 1, .., N)$ and the actual position $\vec{r}$. The force $\mathbf{F}_i$ acting on atom i is then evaluated as the gradient of the interatomic potential U with respect to the coordinate $\vec{r_i}$:

$$\mathbf{F}_i = -\nabla_{\vec{r_i}} U \tag{1.12}$$

The dynamics of the system at a given temperature T is obtained by numerically solving the Langevin equation

$$m\ddot{\vec{r}_i} + m\gamma\dot{\vec{r}_i} = \vec{\xi_i}(t) + \mathbf{F}_i + \mathbf{F}_i^D(t) \tag{1.13}$$

where $-m\gamma\dot{\vec{r}_i}$ is a damping term and $\vec{\xi_i}$ $\delta-$correlated random forces that obey the fluctuation-dissipation theorem:

$$\langle \xi_{i\alpha}(t)\xi_{j\beta}(t')\rangle = 2m\gamma k_b T\delta_{ij}\delta(t-t')\delta_{\alpha\beta} \tag{1.14}$$

where γ is the damping coefficient, k_b the Boltzmann constant, δ_{ij} and $\delta_{\alpha\beta}$ Kronecker deltas and $\delta(t-t')$ the Dirac delta. The term $\mathbf{F}_i^D(t)$ that appears to the right-hand side of eq. (1.13) refers to external driving forces. For instance, a uniform external force that acts on the slider can be adiabatically ramped up until the static friction threshold is reached. This procedure is used to calculate the static friction force of the interface.

In a different scheme, $\mathbf{F}_i^D(t)$ can be provided by a spring moving at constant velocity v (as depicted in panel (a) of Fig. 1.7) and attached to the slider. In this way, the slider reaches a steady state after depinning, usually a smooth sliding or stick-slip motion, in which the average value of the external force, measured by the average spring elongation, equals the average kinetic friction.

The use of the Langevin equation in nanofriction is necessary to simulate at the same time a finite temperature (where needed) and to describe dissipation through microscopic degrees of freedom that are not explicity taken into account in the dynamics, typically phonons within the bulk-substrate, the production of local currents in metallic interfaces and the spin in magnetic materials.

A critical issue in simulating molecular systems concerns the characteristic time-scales necessary to observe frictional phenomena. In fact, the typical times that a medium-size MD simulation can handle are of the order of some μs, depending on the system size, which is normally of the order of $N = 10^5$ atoms. This computational limit is essentially determined by the choice of the MD-timestep, since the integration of the fastest degrees of freedom of the system has to be performed.

This timescale has to be compared with the typical times, sizes and speeds of tribology experiment.

If we wish to address macroscopic sliding experiments for instance, typical speeds would be in the 0.1 to 10 m/s range: in $1\,\mu$s the slider advances by 0.1 to $10\,\mu$m, i.e., approximately 10^3 to 10^4 typical lattice spacings, enough for a fair statistics of atomic-scale events. In a nanoscale FFM experiment however the tip advances at a far smaller average speed (i.e. $1\,\mu m/s$) and we can simulate 1 pm advancement in a typical run, far too short to observe even a single atomic-scale event.

This huge difference between theory and experiment can be overcome by adjusting the free parameters of the simulation, e.g. the damping rate γ or the amplitudes of the microscopic interactions, as it is done in chapter 6 in order to have a qualitative agreement with the experimental data.

The choice of an appropriate potential U which can faithfully describe the system of interest is in general a quite complicated task, especially when dealing with friction. This many-body function is in fact determined by the quantum mechanics of electrons, which is not explicitly treated in

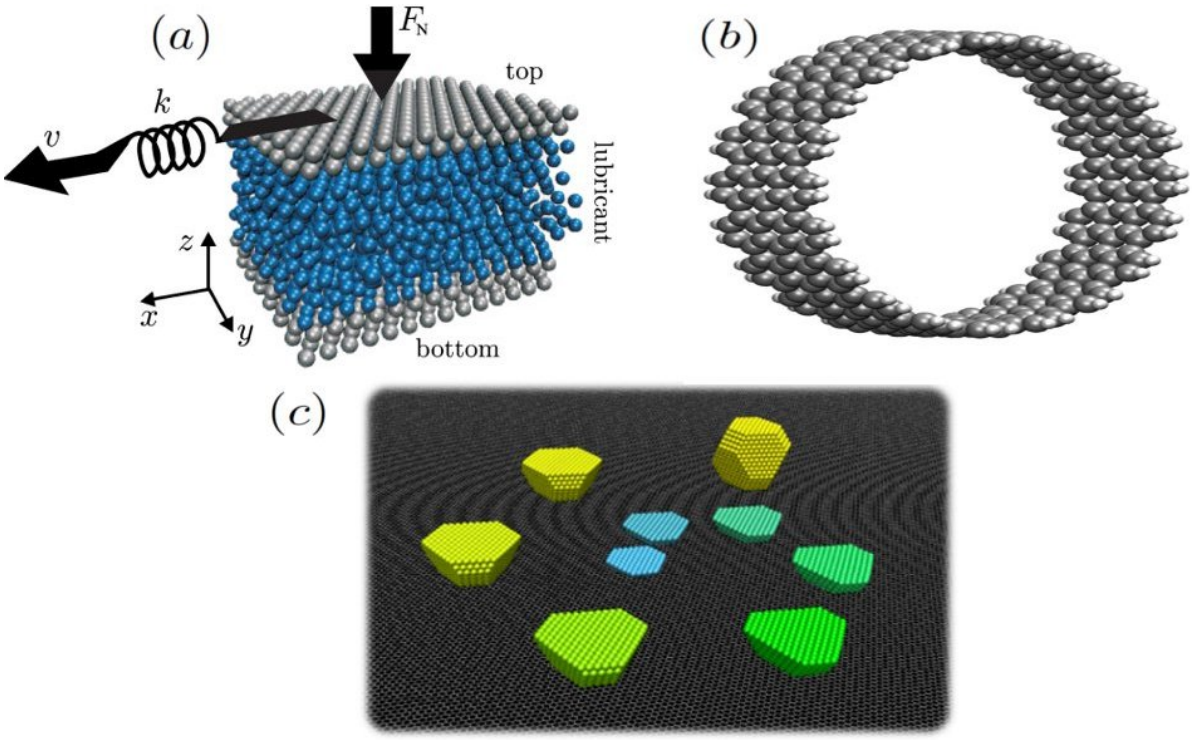

Figure 1.7: Model systems used in typical MD simulations. Panel (a) shows a sheared boundary-lubricated interface. Periodic boundary conditions are applied in the $(x-y)$ directions and a normal load F_N is applied to the top substrate in the z- direction (adapted from [1]). Panel (b) shows a relaxed H-passivated graphene nanoring used for energy minimization calculations. Panel (c) shows a spirally-arranged sequence of gold-on-graphite simulated nanosystems (from [75]), used to prove that the transition from a 2D gold island to a 3D octahedral gold cluster promotes superlubricity.

classical MD. *Ab-initio* MD schemes, of the Car-Parrinello type [74], address this task in general by explicitly solving for the fast quantum dynamics of the electrons and then taking into account their effect on the slow "classical" dynamics of the much heavier ions. The motion of the ions is then determined by an effective potential energy due to the ion-ion interaction and the interaction between the ions and the electron charge density surrounding them.

These schemes have not been of use so far in the context of nanofriction, since they can handle the dynamics of a limited number of atoms, typically in the range of hundreds, and for very short times ($<$ 1ns).

To simplify this rather complicated problem, most MD "frictional" simulations make use of empirical interatomic potentials (the *force fields*), ranging from sophisticated energy surfaces coming from Density Functional Theory (DFT) calculations, to angle-dependent many-particle potentials that are found to reliably describe the properties of specific materials (such as the Embedded-Atom-Model for gold clusters and hydrogen-defect interactions in metals [76, 77] or the AIREBO potential for hydrocarbons [78]), to simple pairwise potentials (e.g. the Lennard-Jones and the Morse potential).

The use of the force fields in general allows a qualitative understanding of the microscopic phenomena that happen in a sliding interface. However, a quantitative agreement with experiment is usually hard to obtain. For instance, in a violent frictional process such as wear, atoms may

change substantially their coordination, their chemistry and their charge. All these changes may involve a complete reparametrization of the interatomic forces and drastically change the outcome of the MD simulations.

A promising approach to solve this problem is provided by the so-called reactive potentials [78, 79], capable of describing chemical reactions and interface wear, without accounting for the full quantum dynamics of electrons.

1.2.4 Joule heat dissipation in MD simulations

As anticipated in Sec. 1.2.3, MD simulations of nanofriction usually require to solve Langevin equations, where the presence of a thermal bath is needed to both simulate an environment at finite temperature T and describe dissipation channels that are not explicitly included in the dynamics.

Let us consider for instance the effect of an external elastic force of the form

$$\mathbf{F}^{\mathbf{D}}_{\mathrm{tot}} = \sum_{i=1}^{n} \mathbf{F}_i^D(t) = -k \sum_{i=1}^{n} (\vec{v}t - \vec{r}_i(t)) \tag{1.15}$$

acting on a slider on top of a rigid substrate, where k is the stiffness of the applied spring, $\vec{v}$ the velocity of pulling and $\vec{r}_i(t)$ the position of the atoms $i = 1, .., n$ that are attached to the moving spring.

Let the slider be initially at rest and let the spring start its motion. The elastic applied force will increase linearly with time in this initial pinned state until the static friction threshold is reached. At this point, the slider moves.

What happens now during sliding? The moving spring is pumping mechanical energy into the system, which is partly converted into kinetic energy of the slider and partly into phononic vibrations. If the excess energy brought by these phononic modes is not removed through some dissipation channel, the interface temperature increases causing overheating, as a straightforward consequence of Joule heat dissipation. Secondly, the slider does not reach a steady state, but rather starts accelerating.

Usually in real experimental systems this energy is brought away from the interface by phonons that are propagating through the bulk of the substrate and the slider, or by electronic excitations in metallic interfaces. Instead, since in MD simulations we usually work with small-size systems where the substrate crystalline structure contains just a few layers, the excitations that are generated at the interface by the driving force propagate and are then backreflected by the cell boundaries rather than properly dispersed away.

To avoid overheating and to attain a frictional steady state, the Joule heat must be removed, by using standard equilibrium thermostats, such as velocity rescaling [80], Nosè-Hoover [81] or Langevin dynamics [82].

In this way, the atoms are not following their conservative trajectory any more. They are instead performing an unrealistic damped dynamics and the features of the steady state motion strongly depend on the exact value of the damping parameter γ. In the Prandtl-Tomlinson model for instance damping is known to modify kinetics and friction, both in the stick-slip regime (including the multiple slips observed in atomic force microscopy) and in the smooth sliding state [61]. This

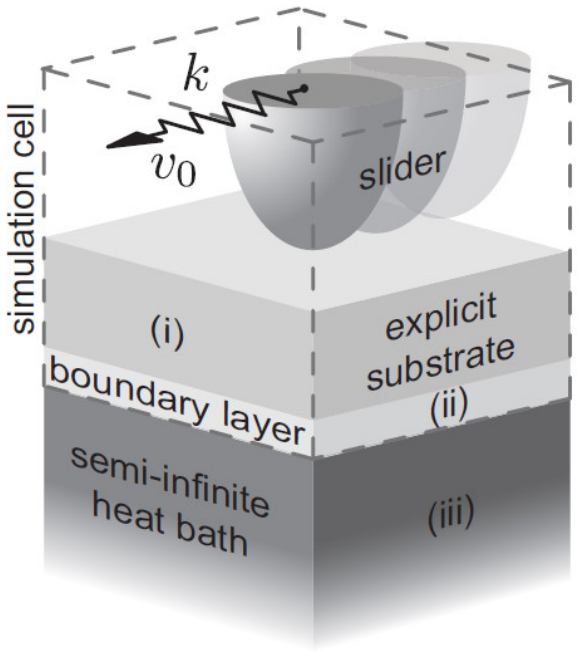

Figure 1.8: Ideal block-scheme of a MD simulation of friction. To account properly for heat dissipation, the infinitely-thick substrate is divided into three regions: (i) a "live" slab comprising layers whose atomic motion is fully simulated by Newton's equations; (ii) a dissipative boundary zone, coincident with the deepmost simulated layer, whose dynamics includes effective damping (e.g., non-Markovian Langevin-type) terms; (iii) the remaining semi-infinite solid, acting as a heat bath, whose degrees of freedom are integrated out. From [89].

lamentable state of affairs is common to all frictional MD simulations, where only the equilibrium configuration of the system happens to be independent of the damping rate.

The use of the Langevin equation to simulate friction with MD was introduced by Robbins and coauthors in a series of works [83, 84, 85, 86, 87]. In these works, they limit the problem of the arbitrariness in the choice of γ (see Eq. 1.13) by applying the Langevin damping only on the degrees of freedom that are perpendicular to the sliding direction. They in fact claimed that thermostatting them, leaving the motion in the direction of sliding undamped, does not the affect the final steady state.

A more rigorous approach to address this complicated task has been introduced in [88, 89]. Consider a simple tribological system characterized by a slider, for instance a 1D chain, which is driven by a laterally moving spring on a 2D semi-infinite crystalline substrate. In this case, the ideal infinitely thick substrate is divided, as sketched in Fig. 1.8, into three regions: (i) an explicit portion of the substrate of N_z layers that are simulated with standard Newton's dynamics; (ii) a dissipative boundary layer and (iii) the remaining semi-infinite solid as a phonon adsorber, which can be modelled as an harmonic solid. Under not too restrictive assumptions, the heat-bath degrees of freedom can be integrated out to let a small simulation cell, namely (i)+(ii), account exactly for the energy dissipation as due to a semi-infinite substrate. Integrating out those degrees of freedom leaves an additional term in the equation of motion of the boundary layer, which is now subject to a non-Markovian dissipative noise [90, 91, 92, 93].

1.3 MD simulations vs. experiments

MD simulations have proven very useful to describe a variety of phenomena in nanotribology. Here we report some selected MD results from the growing simulation literature.

1.3.1 Friction of rare gas adsorbates on metals

One of the major successes of Molecular Dynamics comes from the simulation of adsorbed monolayers (e.g. noble gases of Kr and Xe) on metallic substrates, such as Au or Ag. Most simulations of the friction between adsorbed layers and substrates have been motivated by the pioneering Quartz Crystal Microbalance (QCM) experiments of Krim *et al.* [94, 95].

The main idea of a QCM experiment is the following: a quartz crystal is coated with metal electrodes that are used to excite resonant shear oscillation in the crystal. When atoms adsorb onto the electrodes, the increased mass causes a decrease in the resonance frequency. Instead, when the QCM is made to slide beneath an adsorbate the result is friction and a broadening of the resonance. Therefore, by measuring the resonance frequency of the crystal and the width of resonance peak we can evaluate the static friction per atom. The fact that the peak of the resonance for the bare quartz crystal is extremely sharp guarantees the high sensitivity of this apparatus.

In most experiments by Krim *et al.* the electrodes are the noble metals Ag or Au. The interactions within these noble metals are typically much stronger than the Van der Waals interactions between the electrodes and the adsorbed molecules. Thus, to a first approximation the substrate remains unperturbed in the sliding dynamics and can be replaced by a simple periodic potential, where the substrate atoms are kept fixed at lattice sites [96, 97].

The interaction potential U_{sub} between an adsorbate atom and a rigid substrate can then be expressed as a (1st order) Fourier expansion in the reciprocal-lattice vectors $\vec{Q}$ of the substrate surface:

$$U_{\text{sub}}(\vec{r}, z) = U_0(z) + U_1(z) \sum_l \cos(\vec{Q}_l \cdot \vec{r}) \tag{1.16}$$

where $\vec{r}$ is the position within the plane of the surface and the sum is performed over symmetrically equivalent vectors $\vec{Q}$. Steele *et al.* [98] have demonstrated that if the interaction between the substrate and the adsorbate is modelled through a simple $(6, 12)$ Lennard-Jones interaction of the form

$$U(r) = 4\epsilon \left[\left(\frac{\sigma}{r}\right)^{12} - \left(\frac{\sigma}{r}\right)^{6} \right] \tag{1.17}$$

where r is the distance between each pair of substrate/adsorbate atoms and ϵ and σ the adsorption energy and distance respectively, the higher harmonics in the Fourier-expansion give a contribution which is exponentially small with $|\vec{Q}|$ and can thus be neglected. This is a quite important result from the point of view of MD simulations, since the Lennard-Jones potential is reliable to describe the adsorption properties of weakly interacting rare gas islands on metallic substrates [99], as it is the case for these simple nanofriction experiments.

The interaction between adsorbed atoms is modelled with a Lennard-Jones potential too. For noble gases ϵ typically ranges between $2 - 20$ meV while σ ranges between $2.75 - 4$ Å.

One of the greatest disadvantages of the Lennard-Jones potential though is that it just takes into account pairwise interactions, leaving only two free parameters to be fitted with the experimental data. This brings about the difficulty of both fitting the per-atom adhesion (or adsorption energy) and the lateral corrugation of the substrate, as we will show in chapter 6.

With this setup, it is possible to access the different regimes predicted by the FK model. The simplest case is the limit of low corrugation which is obtained by reducing the amplitude of the oscillating part of the potential of eq. (1.16) and a fluid or incommensurate solid state of the adsorbed layer.

As expected from the theory of the Aubry transition in the FK model (see Sec. 1.2.2), the monolayers do not experience a static friction and the kinetic friction is proportional to the velocity $F_{\mathrm{k}} = -\Gamma v$ [100, 101]. The constant of proportionality Γ gives the slip-time $t_s = m/\Gamma$, which is the characteristic time of momentum transfer between the adsorbate and the substrate. It can be directly measured in the simulations either by calculating the average velocity of the adsorbate as a function of the external force that is needed to reach a steady state after depinning [102] or by giving to all atoms an initial velocity (with no Langevin thermostat) and then using its exponential decay in the subsequent "viscous" dynamics [103].

Commensurate monolayers or incommensurate ones but with a large corrugation exhibit a completely different behavior. As expected from the predictions of the 1D FK model, these systems have a static friction. Unfortunately the Aubry transition in QCM experiments has not yet been discovered since the static friction is too high to be measured with this technique.

Some insights can still be obtained from simulations. For instance, Persson *et al.* [100] considered a two-dimensional model of Xe on a (100) silver substrate. Depending on the corrugation strength he found fluid, 2x2 commensurate and incommensurate phases. They studied the behavior of $1/\Gamma$ as the commensurate phase was reached by lowering the temperature in the fluid phase (fluid to commensurate transition) or either by decreasing the coverage area, i.e. the density of the adsorbate on the substrate, in the incommensurate phase. This last technique is an artificial way to obtain an incommensurate to commensurate transition.

In both cases, it was found that $1/\Gamma$ went to zero at the boundary of the commensurate phase, implying that there was no flow in response to any external force and indicating the presence of a pinned state.

When the static friction is exceeded in one of these commensurate states, the dynamics of the adsorbate becomes absolutely non-trivial. It was shown that sliding causes a transition from a commensurate crystal to a fluid layer and a further increase in the force determines a first-order phase transition to an incommensurate one. Decreasing the force back leads again to a fluid phase, but the initial commensurate state is regained only when the applied force is well below the static friction barrier, indicating hysteresis.

In a more recent paper [104] an incommensurate and ideally superlubric Kr/Pt(111) interface is studied. The results for hexagonally and circularly shaped islands indicate that the finite size of the system can introduce a residual pinning of the monolayer, due to the lack of sampling of the incommensurability, as predicted by the FK model. The barrier's relative role and importance and the ensuing static friction are found to decrease with increasing the island's size and temperature. Since then the static friction is edge-originated, its scaling law with the island's area $F_s \propto A^{\gamma_s}$ is not only sublinear $\gamma_s < 1$, but also sublinear with respect to the island's perimeter, i.e. $\gamma_s < 1/2$,

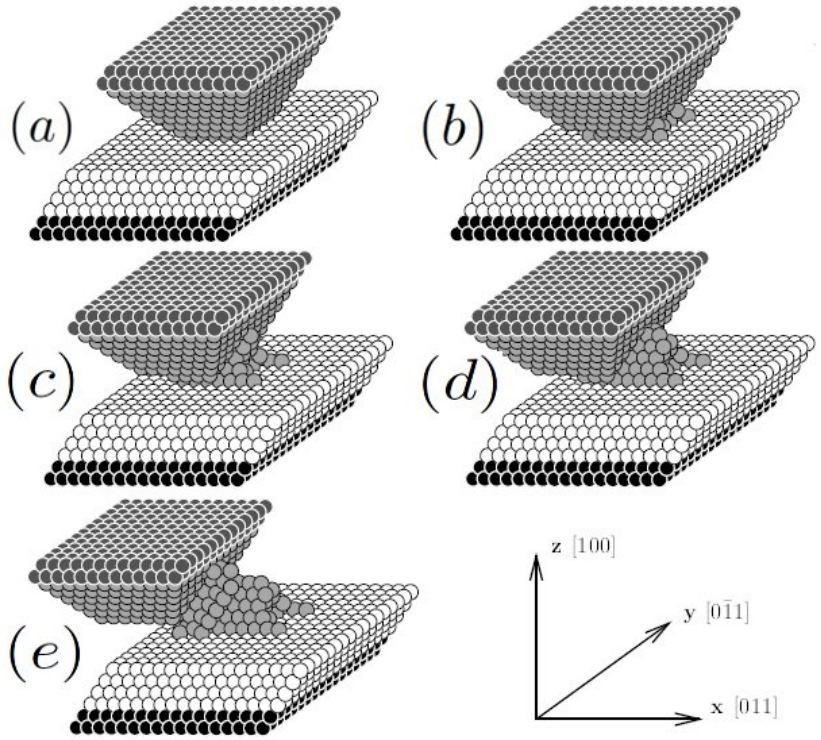

Figure 1.9: Sliding dynamics of a Cu(100) tip on a Cu(100) substrate along the [011] direction, indicated as the x-axis. The interlayer shear between (111) planes in the Cu-tip induces plastic deformation and wear. Adapted from [105].

indicating that only a zero-measure subset of edge points are responsible for pinning.

1.3.2 Wear in single asperity contacts

As anticipated in Sec.1.1.1 dry friction between macroscopic objects is strongly determined by surface roughness. In particular, the tribological response of an interface is mediated by asperities and multi-contacts that typically have the size of 1μ m.

This size is much larger than the atomic scale. However, simulations of atomic-scale contacts can provide information about the effect of contact area and wear on friction in well-controlled interfaces and accurate models for sliding of the AFM tips used in experiments.

Sørensen *et al.* [106] performed simulations of sliding (111) and (100) Cu-tips in contact with Cu-substrates with the same crystalline structure, as shown in Fig. 1.9. The top-layer of the tip and the bottom-layer of the substrate are treated as rigid units, while all the other layers are free to move. Interatomic forces and energies were calculated using semiempirical potentials derived from effective medium theory [107].

At finite temperatures, the outer layer of the Cu-tip is coupled to a Langevin thermostat. The tip is then made to slide on the substrate at constant velocity.

In the commensurate (111) case, the tip performs an atomic-scale stick-slip motion due to finite static friction. The zig-zag trajectory of the tip indicates that the tip jumps between regions with fcc and hcp stacking. A detailed analysis of these jumps shows that the slips of the tip take

place through a dislocation mechanism. Kinks are formed in the front part of the tip due to lateral compression and antikinks are formed in the tail; their nucleation and propagation across the whole area of contact enable sliding. This depinning mechanism is common in many simulated systems, but a direct observation of kinks and antikinks was feasible in experiments only recently in the case of colloidal crystals driven on different types of ordered substrates [26].

In this commensurate state, no wear was observed as the (111) surfaces are the preferred slip planes in fcc metals.

Adhesive wear was instead observed in the case of a (100) Cu-tip sliding in the [011] direction, as shown in Fig. 1.9. The commensuration between the (100) top plane of the substrate and the bottom one of the tip leads to a strong pinning. Since then the inter-plane sliding takes place between adjacent (111) planes, the result is a plastic deformation, where a trail of atoms are left behind the tip during sliding. This effect was confirmed by an increase of the adhesive energy between the tip and the substrate as a function of the sliding distance, due to an increased contact area.

This constant evolution of the tip due to wear keeps the dynamics from being periodic. Still, due to the strong adhesion of the tip, an atomic-scale stick slip motion is present.

Sørensen *et al.* [106] also studied the dynamics in an incommensurate Cu(111) tip/substrate configuration, that was obtained by a rotation of the tip by 16.1° around the [100] direction, i.e. the axis perpendicular to the substrate. The dynamics depends on the size of the tip and on the applied vertical load F_N. For a small tip (5x5 atoms) an Aubry transition between a smooth sliding state with no static friction and a stick-slip motion with a finite static friction was observed by increasing F_N. Increasing F_N further leads to inter-layer sliding in the tip and plastic deformation, since the pinning at the interface becomes stronger. Larger tips, for instance a 19x19 atom tip, did not show any Aubry transition and smooth sliding was observed in the whole range of applied loads.

This result indicates that small tips are never truly incommesurate, as a source of pinning is represented by the corners of the tip. This effect is common to many simulated system, where finite size effects inhibit lubricity.

1.3.3 Extreme temperature and speed conditions

Molecular Dynamics provides the opportunity to simulate systems in conditions that are difficult or even impossible to reach in experiment. One example is the high interfacial temperature that is reached by local Joule heating due to wear of the contacting surfaces [41]. MD simulations of solids close to the melting point show that the outermost layers of the solid, even in equilibrium conditions, undergo surface melting [109]. The presence of a solid-vapor interface, where the thickness of the vapor layer grows without limit as $T \to T_m$, makes it hard to access the frictional behavior of an interface close to the melting point in AFM experiments.

In fact, the liquefied surface layers jump to contact as the AFM approaches the sample causing a wetting of the tip long before it reaches nominal contact. The result is the formation of a liquid neck between the surface and the AFM tip and the motion of the AFM starts once the rupture of this neck is achieved [110].

However, some crystalline surfaces, such as the NaCl(100), do not exhibit surface melting and

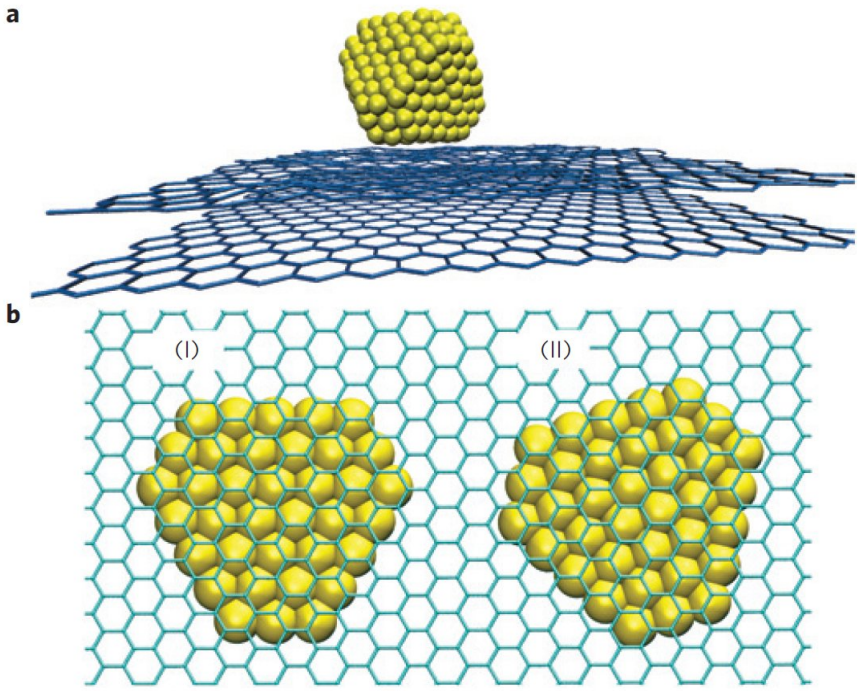

Figure 1.10: Simulated gold nanocluster on a graphite substrate. a) A truncated octahedron Au_{459} cluster sliding with its 36-atom (111) facet over a mobile graphite substrate. b) In-registry (I) and out-of-registry (II) geometries for the cluster's (111) contact facet and the graphite substrate. From [112].

thus AFM friction could in principle be explored. MD simulations of a rigid diamond tip sliding on a NaCl(100) surface have been performed in [111]. The apex of the tip is modelled as a 400-atom rigid cone to explore the regime of indentation and deep wear, whereas it has a flat circular shape with a contact size of ~ 200 atoms to explore the superficial wearless sliding regime.

These two regimes show a completely different phenomenology. In the first case, the tip apex plows into the NaCl substrate and the kinetic friction, initially very large at low temperature, drops at the melting point. Close to the solid-liquid transition, the AFM motion itsself is causing local melting in the substrate and the tip is moving followed by a tiny liquid droplet.

In the wearless regime instead the opposite behavior is predicted. Here kinetic friction is very small at low temperature and increases by raising the temperature. This happens because the substrate is more flexible at high temperatures, leading to a larger average friction.

A second example is high-speed nanofriction, where a tip or a surface-deposited nanocluster is sliding on a crystalline substrate at velocities that are many orders of magnitude larger than the ones obtained in experiments. An example of such a system is provided by Guerra *et al.* in [112], where the dynamics of an octahedral gold nanocluster on a mobile graphite substrate is simulated (see Fig. 1.10). In this paper, Guerra *et al.* predict that the nanocluster dynamics is mainly dominated by diffusion at weakly applied external forces. The result is a low-speed drift regime where the slip time (i.e. the characteristic time of diffusion $\tau = m\mu$, with m the mass and μ the cluster mobility) increases with the temperature.

In the high-speed limit instead, which is reached when the initial nanocluster velocity is set

above 10 m/s, a completely different regime is found. The system performs in this case a ballistic "straight" trajectory and the slip time is expected to decrease with temperature. In fact when the cluster is sliding at such high speeds, the substrate corrugation is averaged out and the cluster is subject to a viscous slowdown. The initial kinetic energy of the cluster is thus transferred to the substrate via the interaction of the cluster with the thermal excitations of the graphite substrate. Since the out-of-plane square displacements in the graphite substrate have a magnitude $< u_z^2 > \propto k_b T$, where k_b is the Boltzmann constant and T the temperature, the interactions with these random thermal corrugations give rise to an effective damping coefficient which increases with T. The slip time and distance are then predicted to decrease as $1/T$, a behavior which has been confirmed by the MD simulations.

Chapter 2

Nanofriction in the experiments

The field of nanofriction has gained impulse over the last decades through the invention and successive development of novel experimental techniques, that brought up the opportunity of studying fundamental aspects of friction at atomic-scale interfaces. Notable examples of these techniques, which are currently used to measure frictional and adhesive forces at the nanoscale, are represented by Atomic/Friction Force Microscopy (AFM/FFM) [7], the Surface Force Apparatus (SFA) [44] and the Quartz Crystal Microbalance (QCM) [94, 95].

In this chapter, we briefly review the operating principles of these techniques, focusing on the importance they had in the growth of this fascinating field of research.

2.1 Atomic/Friction Force Microscopy (AFM/FFM)

2.1.1 Force sensing

In AFM/FFM experiments, a small sharp tip (with a radius typically between $10 - 100\,\text{nm}$) is attached to the end of a compliant cantilever, as shown in Fig. 2.1, and then brought into contact with a sample surface.

The forces acting between the tip and the sample during approach and lateral sliding of the tip will cause a deflection of the cantilever. In particular, the cantilever bends vertically (i.e. towards or away from the sample) in response to an attractive or repulsive interaction with the substrate. The result in this case is a tensile load applied on the tip. During sliding instead the tip is subject to lateral forces that cause a twisting of the cantilever from its equilibrium position.

Thus, in order to simultaneously measure the normal and lateral forces (F_n and F_l respectively) acting on the tip, the deflection of the cantilever needs to be monitored. This is achieved with the so called *optimal beam deflection method*, where a laser beam is reflected from the back of the cantilever into a position-sensitive quadrant photodetector, as sketched in panel (a) of Fig. 2.1. The spot of the laser beam will be displaced upwards/downwards whenever there is an increase/decrease of the applied tensile load and right/left as a result of a lateral force.

This method measures the angles by which the cantilever is bent by applied forces, which for small angles are linearly proportional to the tip deflections.

As an example, panel (b) of Fig. 2.1 shows a typical "approach-retraction curve", where the

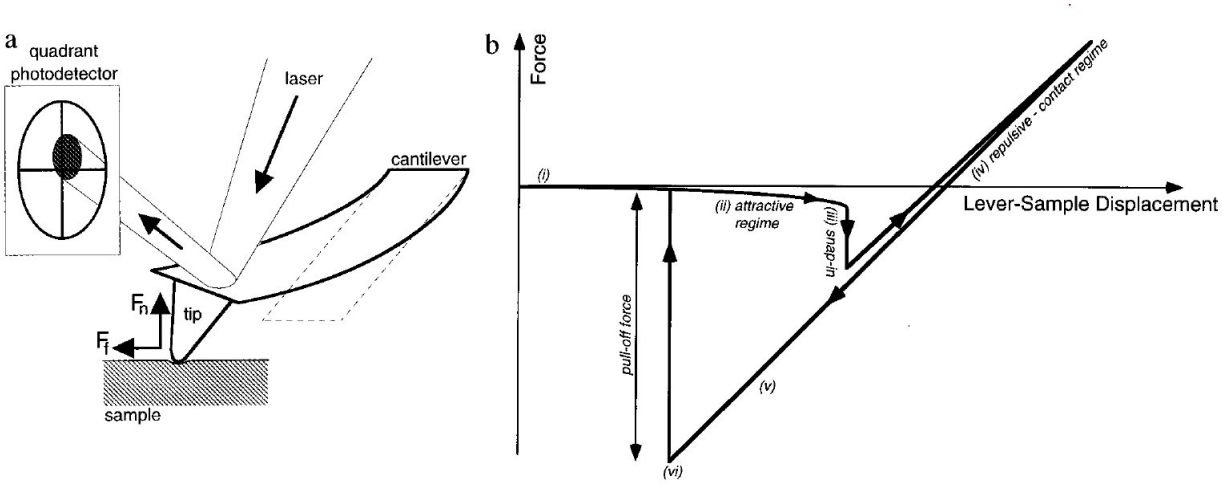

Figure 2.1: Panel (a) shows a schematic view of a typical AFM experiment: the deflection of the cantilever is used to measure the normal and the lateral forces (F_n and F_f respectively) acting on the tip due to the tip-sample interaction. Panel (b) shows a typical "approach curve", where the cantilever bending is reported as a function of the lever-sample displacement, i.e. the distance between the sample and the rigidly held rear end of the cantilever. The curve (i)-(ii)-(iii)-(iv) represents the tip-to-sample approach, while (iv)-(v)-(vi) the retraction. From [113].

tensile load F_n acting on the tip is reported as a function of the lever-sample distance. At point (i) the tip and the sample are far apart and no forces act. As the cantilever approaches the sample (ii), the tip enters an attractive regime (negative force) due to long-range tip-sample interactions. At point (iii) the tip experiences a large force drop (jump to contact), which takes place once the vertical force gradient is larger than the cantilever stiffness. A further approach to the sample causes the force to increase due to repulsive interactions (iv). The result is then an applied (positive) load on the sample. If we now reverse the tip motion and displace the cantilever upwards a similar curve is obtained: the tip passes from a repulsive to an attractive regime (v) until the tensile load overcomes the adhesion of the tip (vi). Once this happens, the tip jumps out of contact and the force suddenly drops to zero.

It is important to notice here that the curves that pertain to the approach and the retraction of the tip do not coincide. This is a result of the fact that the jump-to-contact and the pull-off of the tip do not happen for the same applied load, indicating an hysteretic behavior. The result is that there is an energy loss in the procedure due to tip-sample "non-conservative" interactions.

2.1.2 Atomic-Scale Stick-Slip Behavior with AFM

The most striking results that have been obtained with experiments in nanotribology through Atomic Force Microscopy concern the observation of stick-slip behaviors with atomic-scale resolution [115]. Typical force traces recorded with an Atomic Force Microscope are shown in Fig. 2.2. In their study, Morita *et al.* [114] observed atomic-scale stick-slip between a MoS_2 substrate and a Si_3N_4 tip.

As seen in panels (a) and (b) of Fig. 2.2, both lateral and longitudinal deformations of the cantilever occur, due to the frictional forces that act parallel to the sample surface. By analyzing these signals, the paths that the tip traces out across the sample can be determined, see panel (c).

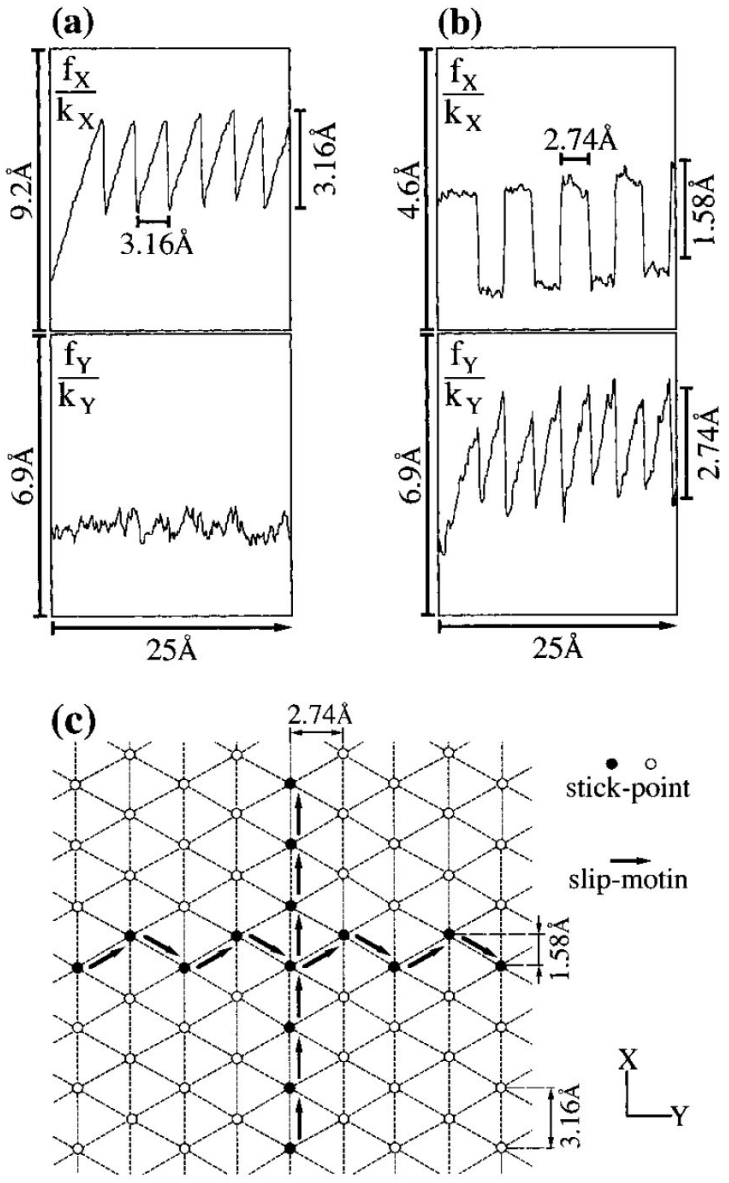

Figure 2.2: AFM data of lateral lever twisting (f_x/k_x) and longitudinal buckling (f_y/k_y) due to frictional forces between a MoS_2 and a silicon nitride tip. From [114].

This is possible because, in the case of an ordered sample, the tip of the AFM prefers to the reside on the lattice positions that are in-registry with the lattice periodicity of the substrate, i.e. to minima of the potential energy surface. These positions correspond to stick points of the AFM.

In the stick configurations, the tip stands still and the cantilever is deflected producing a longitudinal and a normal force. Once the bending energy of the cantilever is larger than the energy barrier to AFM sliding, the tip slides until a new stick point (e.g. the next lattice site of the substrate) is reached and the recorded force drops to its minimum. After that, a new stick-slip cycle occurs.

This means that one can extract information about the lattice periodicities of the substrate from a direct measurement of the lateral twisting (f_x/k_x) and the longitudinal buckling (f_y/k_y) of the cantilever.

The longitudinal axis of the lever in this experiment is parallel to the $y-$axis. In panel (a), the lever is displaced along the $x-$direction indicated in panel (c), i.e. perpendicular to its long axis. Stick-slip behavior along this direction is accompanied by a lateral twisting of the lever and no appreciable longitudinal buckling is observed. The result is then a "straight" stick-slip motion with a period $a_{xx} = 3.16\,\text{Å}$ corresponding to the lattice periodicity of the substrate along the $x-$axis.

In (b) instead the lever is displaced along the $y-$direction indicated in (c), i.e. parallel to its longitudinal axis. In this case, longitudinal buckling and lateral deflection are observed, with two different periodicities: $a_{yy} = 2.74\,\text{Å}$ in the $y-$direction (perpendicular to the scanning direction) and $a_{yx} = 1.58\,\text{Å}$ in the $x-$direction. The result is then a zig-zag motion.

2.1.3 Frictional anisotropy

Another yet unsolved problem in experimental nanotribology is the directionality dependence of friction. Does for instance a slip event for a sliding AFM occur more easily in particular crystallographic directions? Is friction anisotropy a material-dependent feature? Does it change with the topographic orientation of the sample?

In this context, Bluhm *et al.* [116] study the dependence of friction on the FFM scan direction on a surface of cleaved (010) tryglicine sulfate (TGS). Specifically, the sample is a ferroelectric material that presents domains with positive and negative polarity. Within single domains, terraces of half unit-cell step heights divide portions of the sample that are chemically equivalent, but structurally rotated by 180°.

In this work, the sliding FFM is first used to distinguish the frictional domains with different polarity by obtaining a frictional contrast, i.e. a different tribological response when the tip is sliding on top of a positive or negative domain. The FFM images show that this is possible because the opposite polarities are associated to a a different etching of the domains: positive domains contain a large number of etch holes and islands, while the negative ones are almost free of them.

Within one single domain instead, a frictional contrast is observed when the tip passes between regions that are separated by steps of half the unit cell of the TGS structure, as it is shown in Fig. 2.3. No appreciable difference is seen at this point between the forward and the backward scan, except at the edges of the etch islands (see panels (c) and (d) of Fig. 2.3). This is contrary to conventional friction force measurements, where the frictional contrast should be identical between

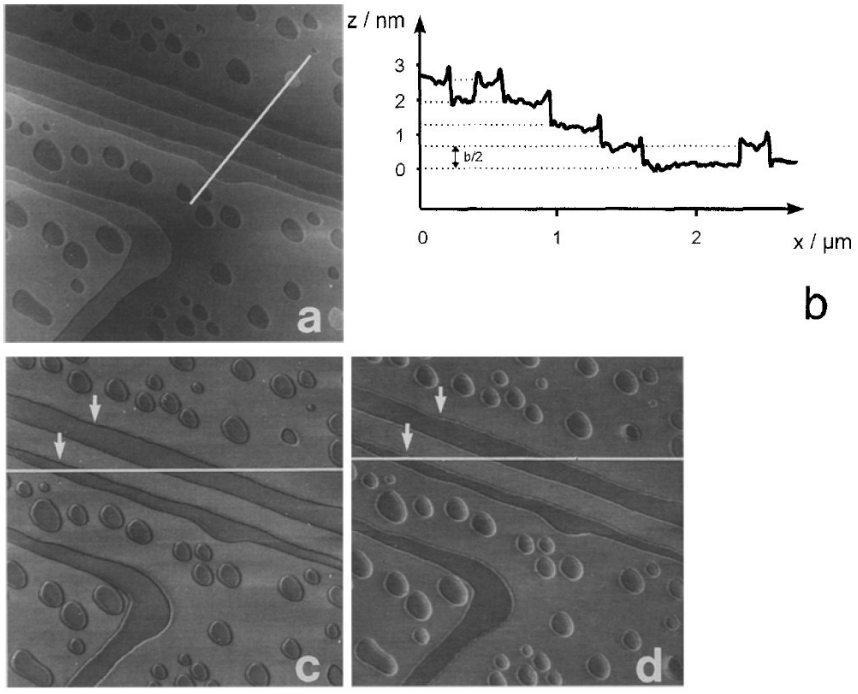

Figure 2.3: Panel (a) shows the $5 \times 5 \mu m^2$ topographical image of a positive domain of the Triglycine Sulfate (TGS) sample used in [116]. Sub-domains separated by steps of height equal to half the unit cell b of the TGS crystalline structure are clearly visibile. Panel (b) shows the $z-$profile along the white line indicated in (a), while panels (c) and (d) show the frictional contrast observed with the FFM between the forward (c) and backward (d) motion of the tip.

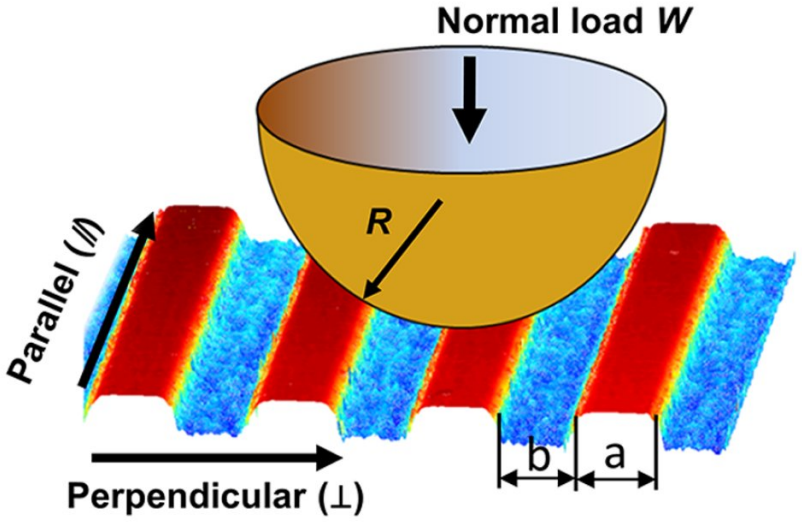

Figure 2.4: Schematic view of two characteristic surface orientations with respect to the relative motion directions. The bank width a and groove width b are shown. From [117].

the two scans but with reversed sign. This result indicates a directional dependence of friction [116].

This idea is strengthened by the results of FFM scanning of the sample at different orientations. It is shown that the frictional contrast is identical but with reversed sign when the sample is rotated by 180°. In between 0° and 180° the contrast is almost zero.

Given the two-fold symmetry relation between the two cleavage surfaces, this means that friction is highest when scanning parallel to a particular molecular structure and lowest when scanning anti-parallel to it. This also confirms the identical kinetic friction traces that were obtained in the forward and backward motion of the tip at a fixed orientation.

The system of interest in [116] demonstrated that a ferroelectric material can provide frictional anisotropy. Another interesting system where directional dependence of friction has been detected is described in [117]. In particular, Yu *et al.* studied how the frictional characteristics of grooved surfaces of different materials depend on the topographic orientation. This type of friction anisotropy is gaining increasing attention due to its importance to innovative designs of frictional interfaces and surface-texturing.

A sketch of the experimental setup, made up of an AFM tip of radius R and a surface with bank width a and groove width b, is shown in Fig. 2.4. The frictional response of the system in this case is discussed in terms of the groove pattern size, the sliding direction, the material and the external load.

The results first indicate that the AFM tip motion in the direction that is perpendicular to the groove pattern (see Fig. 2.4) follows the periodicity of the texture profile, highlighting the frictional anisotropy. An increase of the average kinetic friction in the perpendicular direction for surfaces with wider groove patterns is also registered, as higher energy barriers have to be overcome in the sliding process due to the extended contact size between the tip and the surface. In contrast, friction in the parallel direction is larger for samples with a narrow groove width, as a result of the reduced contact stiffness (inversely proportional to the surface deformation) between the AFM tip and the sample in the perpendicular direction. This friction anisotropy appears to be independent of the material; however, the transition point, i.e. groove width for which the average friction in the perpendicular motion becomes larger than in the parallel one is closely material-dependent.

2.2 The Surface Force Apparatus (SFA)

The Surface Force Apparatus consists of a pair of atomically smooth surfaces, usually mica sheets, which are mounted on crossed cylinders that can be pressed together to form a circular contact under pressure. The two mica surfaces can be then displaced horizontally and vertically by springs to apply and measure compressive and shear forces on liquid films trapped between them. Actuators attached to the surface supports enable a control of the vertical distance between the mica sheets down to the Angstrom level.

The contact area and the relative separation of the surfaces can be measured with optical methods.

When white light passes through the mica sheets, which are coated with a semi-transparent metal film (usually silver), Fabry-Perot interference fringes of color are created when the wavelength

matches the local separation. In this way an image of the contact geometry can be obtained. A spectrometer reveals the interference pattern and from the displacement of the fringes one can measure the vertical separation between the sheets.

Lateral displacements of the mica sheets are possible, allowing for friction and viscosity measurements.

The SFA is ideally suited for the study of the atomic structure and layering of liquid films under compression. For example, it has been shown that when simple fluids, such as linear hydrocarbons, are compressed between atomically flat surfaces deposited on mica, the squeeze-out dynamics of the liquid is mainly determined by the hard repulsive interaction between the liquid and the hard walls. The result is that the fluid is subject to a stepwise thinning, so that by smoothly increasing the load the distance between the mica sheets decreases in steps, when the number of molecular layers is sufficiently small. This indicates a fluid layering, where every single layer can substain an applied load before being squeezed out, suggesting a solid-like behavior [118].

These conclusions have been proven by the measurements of Klein and Kumacheva in [119]. They studied the shear properties of a layered liquid film made of octamethylcyclotetrasiloxane (OMCTS) and found that its tribological response when it is made of seven or more layers is viscous-like. In other words, they observed a smooth-sliding of the driven mica sheet in contact with the liquid, where the kinetic friction is proportional to the relative velocity.

Instead when the number of layers is decreased to just six by applying a vertical load, the result is an abrupt and irreversible transition to a solid-like behavior, confirming the observation of [118]. In this solid-like state the film is initially not responding to an applied shear stress, but then it suddenly performs a slip. The resistance to shear induced by this liquid-to-solid transition increases by even seven orders of magnitude just by removing one molecular layer.

In direct contrast with the results of [119], Damirel and Granick [120] observed a monotonic increase in the shear relaxation time, elastic modulus, and effective viscosity of an OMCTS film for separations of less than about 10 molecular diameters between the mica surfaces, with a smooth transition to solidity. This is clear from panel (b) of Fig. 2.5: the effective friction coefficient of the sample decreases as a function of the thickness and approaches the hydrodynamic limit for thicknesses that are about 8 molecular layers.

The discrepancy between these two experimental results highlights some important weaknesses of the SFA instrument. These include the difficulty of ensuring the surface parallelism between the mica sheets and preventing the attachment of foreign particles that may become trapped in the contact area between the sample and the mica sheets that is several micrometers in diameter. Trapped particles of subwavelength size and contaminant molecules do not affect the visible light interference fringes and can thus falsify the distance measurement. Still, all these results demonstrate the very high sensitivity of this apparatus to the molecular structure of the film and the resulting mechanical response.

The layering transition observed in the case of the OMCTS appears also when studying the shear viscosity of water between mica sheets. Zhu and Granick [121] used the SFA to provide controlled shear oscillations in the water film. An anisotropic frictional response was here observed upon changing the relative orientation angle between the mica sheets when the film is made up of less than three monolayers. For films of larger thicknesses, the intrinsic liquid structure of the film dominates friction.

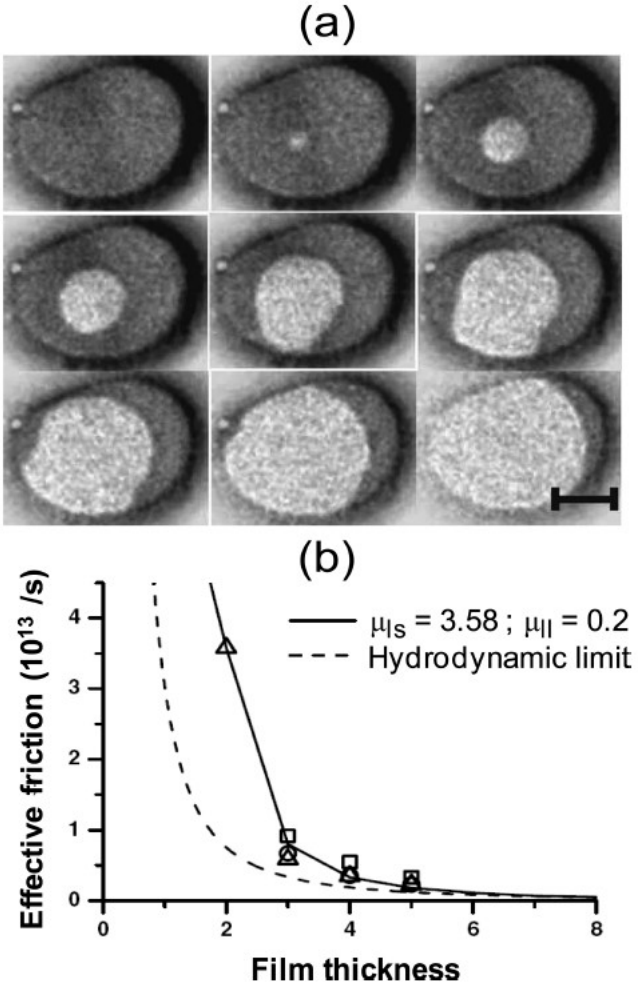

Figure 2.5: Panel (a) shows a sequence of optical images where time-evolution of the squeeze-out dynamics of an OMCTS film. The bright spot in the center is created by the expulsion of one single layer of the film. Panel (b) shows how the effective friction depends on the thickness of the material (measured in units of the thickness of one monolayer). μ_{ls} represents the kinetic friction coefficient between the solid boundary and the first layer of liquid, while μ_{ll} the same quantity measured between adjacent liquid layers. From [122].

2.3 The Quartz Crystal Microbalance (QCM)

The Quartz Crystal Microbalance (QCM) is a familiar tool for monitoring the growth of thin films. The basic operating principle of a QCM is the following: a quartz crystal is coated with metal electrodes which can excite resonant shear oscillations in the crystal. When atoms of the thin film deposit on the crystal, the increased mass causes a decrease in the resonance frequency. In addition, shear between the quartz sheet and the growing film causes dissipation, whose main result is a broadening of the resonance peak.

Therefore by measuring the frequency shift of the QCM and the width of the resonance, we can extract information about the mass of the adsorbed film and the damping due to dissipative forces acting to oppose the inertial force of adsorbates.

The QCM derives its great sensitivity from the sharp resonance frequency of the quartz oscillator due to its large Q-factor, which makes it possible to measure mass changes caused by the adsorption of submonolayer amounts of adsorbates.

Krim and co-workers [94, 95] were the first to realize that the quality factor of the oscillator decreases if there is a frictional shear between the sliding atoms and the substrate. From their measurements, they were able to determine a *slip-time* τ, i.e. the characteristic time (typically in the order of ns) over which friction acts to reduce the relative velocity between the adsorbate and the substrate, as a function of the the adsorbate coverage. From the slip time, it is possible to derive the damping coefficient η as

$$\eta = \frac{1}{\tau} = 4\pi \frac{\delta f_0}{\delta Q^{-1}} \tag{2.1}$$

where δf_0 is the frequency shift of the QCM and δQ^{-1} the variation of the inverse quality factor.

This fine temporal resolution allows for the study of dissipation through phonon and electronic degrees of freedom in the adsorbate.

In [94], Krim *et al.* studied with QCM the adsorption of Kr on a Au substrate at 77.4 K and specifically observed that the quality factor, as well as the slip time, changes with the Kr pressure. They found that this technique is sensitive to phase transformations of the film: the solid monolayer exhibits longer slip times than the liquid, that is the solid slides more easily on Au than liquid Kr. Modeling and simulations by Cieplak *et al.* [86] indicate that such behavior can be explained by the effect of the structure of the monolayer. In the solid phase, the Kr atoms lock into an ordered structure which is incommensurate with the Au substrate and slide more easily than the liquid counterpart.

Chapter 3

Superlubricity: theory and experimental observations

Every-day experience tells us that a finite force, the static friction force F_s, has to be overcome in order to initiate sliding of a solid body against another. Once depinned, a second force, the kinetic friction F_k has to be applied in order to maintain the first body in motion.

Conversely, when dragging a solid body in a fluid medium, there is no static friction at all, in that every applied force would cause a motion of the body. One just has to apply a force to keep the solid in motion relative to the fluid, which has to counteract the effect of the viscous drag (proportional to the velocity).

This simple empirical observation indicates that the presence of a finite static friction can be considered in principle as a way to distinguish a solid-solid to a solid-liquid interface. For this reason, it came as a surprise when Hirano and Shinjo in [123] discovered that sliding states in a solid-solid contact with vanishing friction could be achieved, a physical phenomenon which took the name of **superlubricity**.

Despite this might seem counterintuitive, it does not violate classical mechanics. If one considers for instance a slider and a substrate as perfectly flat homogeneous surfaces, the total free energy of the system does not vary in the sliding process as a result of trivial translational invariance. Consequently, no net work has to be done to substain a relative motion, implying, at least in principle, the possibility of a very low friction state.

In practice, we will see that in the case of crystalline interfaces superlubric states can be obtained as a result of a force-cancellation due to the lattice mismatch or an orientational misalignment between the contacting materials. This generates a potential energy landscape where each atom in the contacting surfaces has only one mechanically stable site in the vicinity of its current position while the center of mass of one solid is displaced with respect to the other one.

The concept of superlubricity is central in this Thesis, as many of the static and dynamic features of the graphene nanoribbon/Au(111) interface observed in our recent papers [36, 37] happen to be an indirect confirmation of its superlubric character. In this chapter, we will give a brief overview of this intriguing frictional phenomenon and will present some of the most relevant experimental observations of superlubricity in real nanoscale contacts.

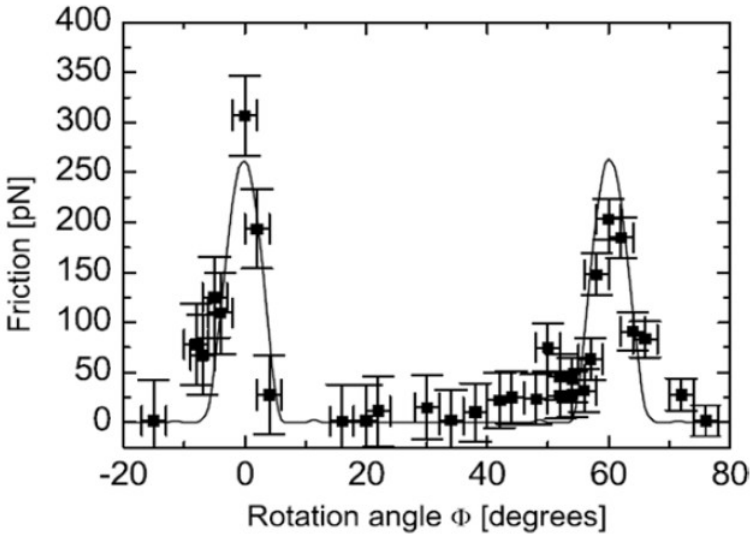

Figure 3.1: Average friction force between an Si_3N_4 tip and a graphite substrate for different orientation angles of the sample. From [126].

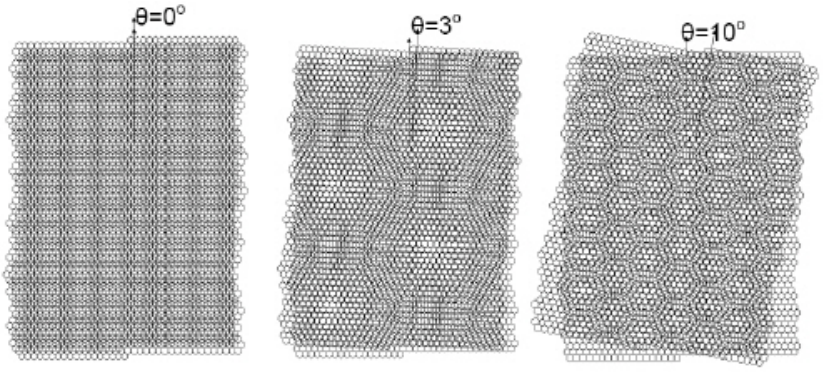

Figure 3.2: Schematic view of two twisted graphite layers corresponding to three different configurations of Fig. 3.1. $\theta = 0^\circ$ corresponds to two perfectly aligned layers giving rise to a frictional peak, $\theta = 3^\circ, 10^\circ$ instead correspond to mismatched configurations with vanishing friction.

More detailed information about how this complex phenomenon affects friction can be found in [6, 125].

3.1 Definition of superlubricity

Defining superlubricity in a mathematically rigorous way is not straightforward.

In experiments, superlubricity refers to the phenomenon where the static friction of an interface is reduced to a very low value below the instrument noise level, as a result of special properties of the interface. In the case of crystalline interfaces, a crucial role is played by the commensurability of the lattice structures: if the two lattices have different periodicities, or if they are misoriented by an angle, the result is that geometrically mismatched regions of the interface start to emerge, potentially leading to states with very low static friction. This effect is also known as *structural lubricity*.

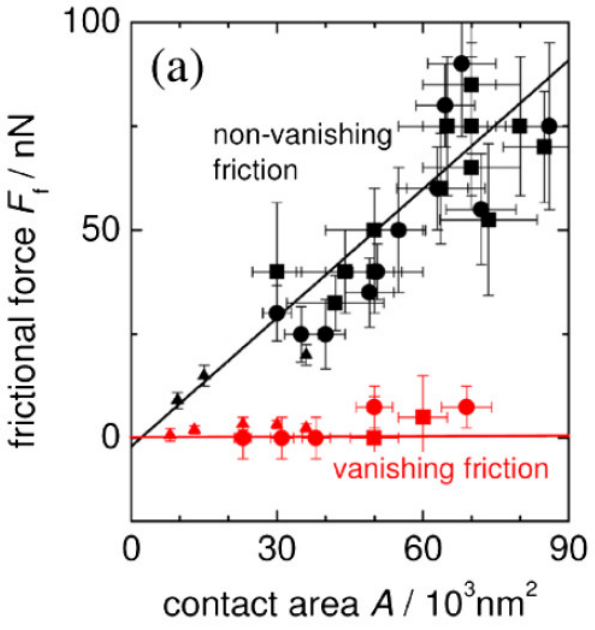

Figure 3.3: Size-scaling of the average friction force for the case of antimony nanoparticles on graphite studied in [55].

In particular, Hirano *et al.* in [124] found a modest reduction (up to a factor 4) in friction between mica surfaces after rotating two sheets with respect to each other. A similar result, often considered as one of the most striking observations of superlubricity in a crystalline contact [126], is shown in Fig. 3.1. In their experiment, Dienwiebel *et al.* studied the average friction of a Si_3N_4 tip sliding on top a graphite sample with a given orientation angle θ.

Two narrow peaks of high friction were found for $\theta = 0°$ and $\theta = 60°$, while for every other value of the angle essentially no kinetic friction was observed. This result can be explained as a consequence of the presence of a graphene flake attached to the tip: for $\theta = 0°$ and $\theta = 60°$, the graphite flake and the substrate are in-registry and commensurate, as shown in Fig. 3.2 and the result is a frictional peak. For every other angle instead the two stiff lattices are mismatched and incommensurate and the result, in agreement with the theoretical predictions of the incommensurate FK model (see Sec. 1.2.2), is a state with vanishing friction within the experimental error.

These case studies suggest the idea that a superlubric state is a "low-friction" state determined by incommensurability and high contact stiffness, which is the basic definition provided by the phenomenology of the FK model.

Another interesting way to define friction comes from the works by Dietzel *et al.* [55] and Cihan *et al.* [57]. In [55] sliding of antimony nanoparticles on a pyrolitic graphite substrate is considered. To distinguish between different frictional regimes of the nanoparticles, the area-dependence of the average kinetic friction is computed. The results show a surprising "frictional duality" (see Fig. 3.3): a subset of the nanoparticles slide with zero average friction, indicating superlubric sliding in the whole range of areas (red line of Fig. 3.3), another subset instead shows a growth of the frictional force with the contact area which follows Amontons' law $F_s \propto A$. This is most probably due to the presence of contaminating particles trapped between the nanoparticle and the graphite substrate. Their presence indeed destroys the incommensurability between the nanoparticles and

the graphite substrate and produce an additional source of pinning in the system [58].

The idea of using a size-scaling to analyse the frictional behavior of an interface is also used in [57], where sliding of gold islands on graphite is considered. The gold-graphite interface is incommensurate due to lattice mismatch, as it is case also for the system of interest of this Thesis, characterized by graphene nanoribbons on gold.

The main result of this work is the fact that the static friction force grows with the size of the contact with a *sublinear* trend $F_s = F_0 A^{\gamma}$, where $\gamma = 0.16$ is the scaling exponent and depends on the details of the specific interface. This result, which can again be considered as a definition of superlubricity, is still confirming the phenomenology of the FK model. In fact, a sublinear increase of the static friction force is compatible with a force which vanishes in the thermodynamic limit $(N \to \infty)$ $F_s \to 0$ for an incommensurate and stiff interface.

Signals of superlubricity also appear in colloidal systems. As we have pointed out in Sec. 1.2.2 when describing experimental realizations of the FK model with trapped polystyrene particles in an optical lattice, the advantage is that it is possible to directly tune the amplitude of the corrugation potential u_0 and consequently cross the Aubry transition, provided that the colloidal monolayer is incommensurate with the substrate. In this case, signals of superlubricity come from monitoring the static friction force F_s as a function of u_0 and the average mobility of the monolayer $< \mu >= v/F$ (see Fig. 1.6) as a function of the driving force F.

The results show that the static friction for weak corrugations u_0 is vanishing within the experimental error and experiences a sharp increase at the Aubry point, separating the superlubric and the statically pinned state. In the superlubric state the average mobility turns out to be finite for any applied force F, while in the pinned state the mobility vanishes for any driving force that is smaller than the (finite) static friction force $F < F_s$ of the system.

3.2 Cancellation of lateral forces

As we have anticipated at the beginning of this chapter, superlubricity between solid bodies seems surprising, as for macroscopic objects we would always expect a finite static friction. As we will see in this section though, superlubricity can be naturally explained as a result of a systematic cancellation of lateral forces due to the lattice mismatch between the surfaces in contact. The argument that we will discuss is valid for perfectly crystalline materials with no defects, revealing also why this frictional phenomenon never takes place for macroscopic objects, where the interface roughness, the presence of defects and out-of-plane deformations completely inhibit lubricity.

When studying lateral forces exerted between two surfaces, symmetries are crucial. For instance, if we consider two perfectly flat and rigid bodies that share a common periodicity, so that discrete translational invariance is obeyed, the friction coefficient is independent on the contact area, or, more in general, indipendent of the number of atoms N in contact with the substrate. The reason is that the forces exterted on the individual atoms in the slider add upp in a systematic fashion in commensurate interfaces. Conversely, for flat, rigid and incommensurate solids there is a systematic annihilation of the lateral forces, similar to the destructive interference in optics. Translational invariance is no more satisfied and the atoms of the slider all sample a different phase of the substrate potential, as we have pointed out in Sec. 1.2.2.

Finally there is the case of disordered surfaces, which describes the friction between glassy materials. Lateral forces in this case have random direction or random sign, consequently they add up in a stochastic way so that the lateral force only grows with $\sqrt{N}$ and the static friction coefficient $\mu_s \propto 1/\sqrt{N}$.

Let us start by considering a minimalistic model of two flat, crystalline solids in contact. It consists of a rigid substrate, which we model as a periodic potential with period b and a slider with lattice constant a. The atoms of the slider are connected to their equilibrium positions by springs of stiffness k_1 and to their neighbours by springs of stiffness k_2. To explore the effects of symmetry to a zero degree order, we will assume that both types of springs are infinitely stiff.

This is essentially a FK model as the one shown in Fig. 1.5, where in addition to the springs in the lateral direction we couple each atom to a vertical spring that connects it to its lattice site.

If the substrate is purely periodic, we can expand the total potential energy of the slider with the substrate in Fourier series as:

$$\begin{aligned} V &= \sum_{m=-\infty}^{+\infty} \tilde{V}(G_m) \sum_{n=0}^{N-1} e^{iG_m(x_0+na)} \\ &= \sum_{m=-\infty}^{+\infty} \tilde{V}(G_m) e^{iG_m x_0} \begin{cases} N & \text{if } aG_m/2\pi \text{ is an integer} \\ \frac{1-e^{iNG_m a}}{1-e^{iG_m a}} & \text{otherwise} \end{cases} \end{aligned} \tag{3.1}$$

Here, G_m are the reciprocal lattice vectors of the substrate with $G_m = \frac{2\pi m}{b}$, $\tilde{V}(G_m)$ are the coefficients of the Fourier expansion of the substrate potential and $x_0 + na$ is the position of atom n in the chain (x_0 is a displacement of the whole slider). The sum over m in Eq. (3.1) runs over the different harmonics of the substrate potential, while the one over n sums the contribution of the N particles of the chain.

This equation is general and holds for every 1D periodic system. Now, further simplifications are obtained when we ensure that V is a real function, which implies that $\tilde{V}(-G_m) = \overline{\tilde{V}(G_m)}$, and when we consider just the low-order harmonics ($m = 0$ and $m = \pm 1$), to obtain:

$$V = NV_0 + V_1 \sum_{n=1}^{N} \cos\left[\frac{2\pi}{b}(x_0 + na) + \phi_1\right] \tag{3.2}$$

where $\tilde{V}(G_0) = V_0$ and $\tilde{V}(G_1) = \frac{V_1}{2} e^{i\phi_1}$, with V_1 real valued. Now, this potential energy landscape depends on the positions of all the atoms of the slider. If we now displace the slider by smoothly varying x_0, we can obtain the lateral force exerted by the substrate on the slider as

$$F = -\frac{dV}{dx_0} = \frac{2\pi}{b} V_1 \sum_{n=1}^{N} \sin\left[\frac{2\pi}{b}(x_0 + na) + \phi_1\right] \tag{3.3}$$

In Eq. (3.3) we have just considered the first harmonic of the Fourier series for reasons of simplicity. We will now explore the effects of symmetry on the way in which F grows with the system size.

3.2.1 Case of a commensurate interface

Two surfaces are called commensurate when the ratio between the lattice constants of the slider and the substrate a/b is a rational number. In this case, there exist two natural numbers p and q, such that

$$\mathcal{L} = pa = qb \tag{3.4}$$

where $\mathcal{L}$ is the smallest common period of the two surfaces. Let us consider now Eq. (3.1): the terms of the Fourier expansion that give a contribution proportional to the system size, or equivalently to the number of atoms in the slider N, are the ones for which $aG_m/2\pi = n$, where n is a natural number.

This leads to the condition $ma = n\mathcal{L}$, so that only the Fourier wavenumbers that are integer multiples of $2\pi/\mathcal{L}$ add up systematically, while the others interfere destructively. Now, for sufficiently large interfaces, the terms that grow proportionally with N dominate and we can approximate the corrugation potential V with

$$V = N \sum_{m,\, \frac{aG_m}{2\pi} \in \mathbb{Z}} \tilde{V}(G_m) e^{iG_m x_0} = N v(x_0) \tag{3.5}$$

where $v(x_0)$ can be considered as an average atomic potential. Typically, the expansion coefficients in the corrugation potential decay exponentially fast with increasing index m and this justifies to keep only the first term in the expansion, which is related to the smallest common period. The first non-constant and non-vanishing term of Eq. (3.1) is the one for which $m = p$ and the corresponding wavenumber is $G_p = 2\pi p/b = 2\pi\mathcal{L}/ab$. So we may finally approximate the total potential energy of the system as

$$V \approx N V_p \cos\left(\frac{2\pi p}{b} x_0 + \phi_p\right) \tag{3.6}$$

where $V_p = 2\tilde{V}(G_p)e^{-i\phi_p}$ is a real number. So we conclude that the corrugation potential and the lateral force F experienced by the slider grow linearly with N, giving rise to a finite static friction force. This rather simplified argument shows that in a commensurate interface, where we completely neglect the effect of the elastic deformation of the slider and the presence of defects, static friction is expected to obey Amontons' law.

3.2.2 Case of an incommensurate interface

When the ratio a/b cannot be expressed by a rational number, the surfaces are said to be incommensurate. One may argue that the two surfaces have a common period $\mathcal{L}$ that is infinite and given the argument that the corrugation potential vanishes exponentially with $\mathcal{L}$, one may conclude that the corrugation potential per surface atom v/N tends to zero for large N.

Alternatively, considering again eq. (3.1), there is no term in the corrugation potential that would increase with the system size, because $aG_m/2\pi = ma/b$ can never take on integer values and Eq. (3.5) has to be replaced with

$$V = v_{\text{inc}}(N, x_0) \tag{3.7}$$

where v_{inc} can be calculated from eq. (3.1). While v_{inc} does not vanish exactly, one can see that it does not grow systematically with N, because the fractions that appear to the right-hand side are rapidly oscillating functions of N and only the first few terms contribute in a significant way.

Keeping only the first term related to $m = \pm 1$, one can see that the maximum lateral force per atom and hence μ_S vanishes with $1/N$ for increasing system sizes or alternatively the net friction force F is independent of N:

$$F_s \propto N^0 \tag{3.8}$$

This is the phenomenon of superlubricity. Since there is no common periodicity between the slider and the substrate, there are no harmonics that interfere constructively to produce a static friction that grows with the system size. Physically, this means that each atom of the slider samples a different relative phase of the substrate corrugation, giving rise to a vanishing lateral force in the thermodynamic limit.

3.3 From vanishing friction to superlubricity in experiments and MD simulations

3.3.1 Frictionless sliding in the PT model

In Sec. 3.1 we have shown that states with superlow friction in the experiments can be achieved by lattice mismatch or an orientational misalignment between two contacting surfaces [124, 126]. Still, the first experimental signatures of superlubricity came from studying the transition between stick-slip motion and continuous sliding of a tip driven with constant velocity on a crystalline substrate, consistently with the phenomenology of the PT model.

As discussed in Sec. 1.2.1, the model predicts two different tip modes, depending on the precise value of the dimensionless parameter $\eta = 4\pi^2 V_0/(ka^2)$, where V_0 represents the corrugation potential of the substrate, k the stiffness of the spring applied to the tip and a the substrate lattice parameter.

In this case a frictionless regime marked by a continuous sliding of the tip is obtained for $\eta < 1$, so that the corrugation potential is small compared to the spring stiffness, whereas for $\eta > 1$ a stick-slip motion of the tip appears.

In the experiments, a tip attached to a silicon cantilever is dragged at constant velocity $v = 3\,\text{nm/s}$ on a NaCl(001) substrate along the (100) direction [62].

Tuning the value of η is possible by effectively changing the tip-sample interaction via a variation of the normal load F_N applied to the tip. The tip slides forwards and backwards while the lateral force is recorded, so that frictional loops for different values of the applied load F_N are obtained, as shown in Fig. 3.4. The total applied load is the sum of the externally applied load and the attractive force between the tip and the sample, which has been determined to be 0.7 nN measuring the force required to pull the tip out of contact.

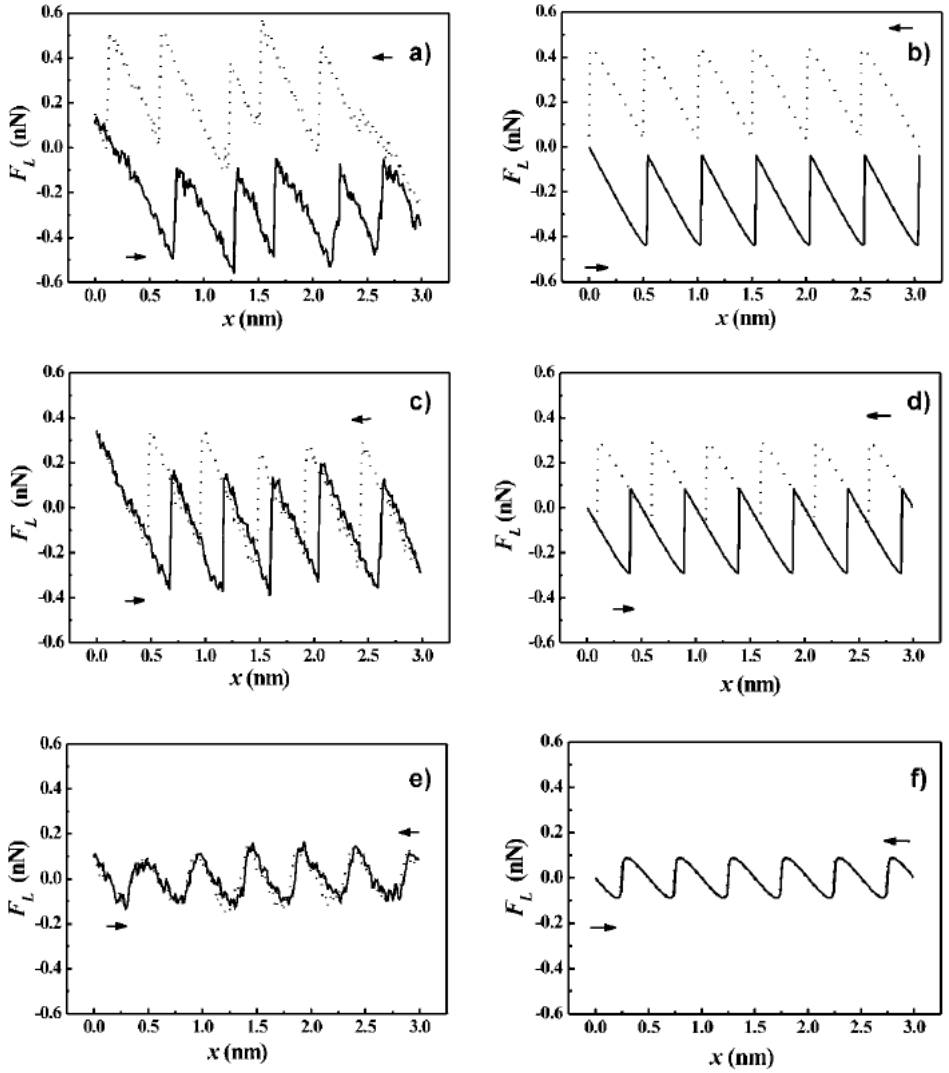

Figure 3.4: Measurements of the lateral force F_L acting on the tip sliding forward and backward on a NaCl(001) surface for different values of the external load: (a) $F_N = 4.7\,\mathrm{nN}$, (c) $F_N = 3.3\,\mathrm{nN}$ and (e) $F_N = -0.47\,\mathrm{nN}$. Numerical evaluation of the lateral force from the Tomlinson model for (b) $\eta = 5$, (d) $\eta = 3$ and (f) $\eta = 1$. From [62].

For an applied load of $F_N = 4.7\,\text{nN}$ the lateral force shows two opposite sawtooth profiles when scanning forwards and backwards. The sawtooth modulation has the periodicity of the crystal lattice along the (100) direction and is characteristic of a stick-slip process. The area enclosed in this hysteresis loop is the energy dissipated in one cycle. When the externally applied load is lowered to 3.3 nN the dissipated energy decreases resulting in a partial overlap of the curves for the forward and the backward scan. In fact, the lateral force changes its sign in the slip event (Fig. 3.4c).

A different picture is found when the load is further reduced. For normal loads below a certain threshold, the hysteresis loop closes and so the dissipation disappears within the sensitivity of the experimental apparatus (Fig. 3.4e). The sawtooth modulation of the lateral force is transformed into a continuous modulation of perfect match between forward and backward scan, still showing the atomic periodicity of the surface lattice.

The observed force loops show excellent agreement with the transition to frictionless sliding that is predicted by the one-dimensional PT model.

Following the definition given in Sec. 3.2, in principle we should not refer to this state of near-frictionless sliding at low normal loads as true superlubricity (or structural lubricity), since it does not involve the cancellation of the lateral forces on individual atoms that makes the barrier to sliding vanish in an extended 2D contact.

3.3.2 Superlubricity of graphene nanoflakes on graphene

In agreement with the experimental results obtained by Dienwiebel *et al.* in [126], superlubric sliding of free graphene nanoflakes on graphene was demonstrated by Feng *et al.* in [127].

In their initial 'equilibrium' state after the sample preparation, the nanoflakes were found to have the same lattice orientation as the underlying graphene monolayer, indicating commensurability. Successive images of the sample morphology recorded with a Scanning Tunneling Microscope (STM) indicated that in a time lapse of 20 minutes some of the flakes were able to diffuse away from their initial position; the displacements of those flakes involved both translations and 60° rotations with respect to the initial equilibrium configuration, while the sliding directions were random and not correlated with the scanning direction, suggesting that the flakes reached a free sliding state before pinning.

To understand the diffusion process, it is necessary to consider the potential energy landscape of the graphene flakes as they move on the graphene layer. The easiest sliding path in fact should be the one for which the flakes experience the lowest possible corrugation and this necessarily involves incommensurate states. For instance, Shibuta *et al.* in [59] used a Lennard-Jones potential to calculate energy profiles for displacements along various directions between two graphene layers (Fig. 3.5b) and obtained a barrier of $0.15\,\text{meV/atom}$ for translations along the zig-zag direction while between incommensurate states (with a rotational angle $10° < \theta < 50°$) the corrugation of the energy landscape is smaller than $0.02\,\text{meV/atom}$.

So it is clear that the motion of a flake along $\theta = 0°$ is energetically more expensive than in a path that connects only incommensurate states. In [127] it is then proposed that the nanoflake first switches from a commensurate to an incommensurate registry (the superlubric state), which is followed by free sliding accompanied by random rotations of the flake until a new commensurate

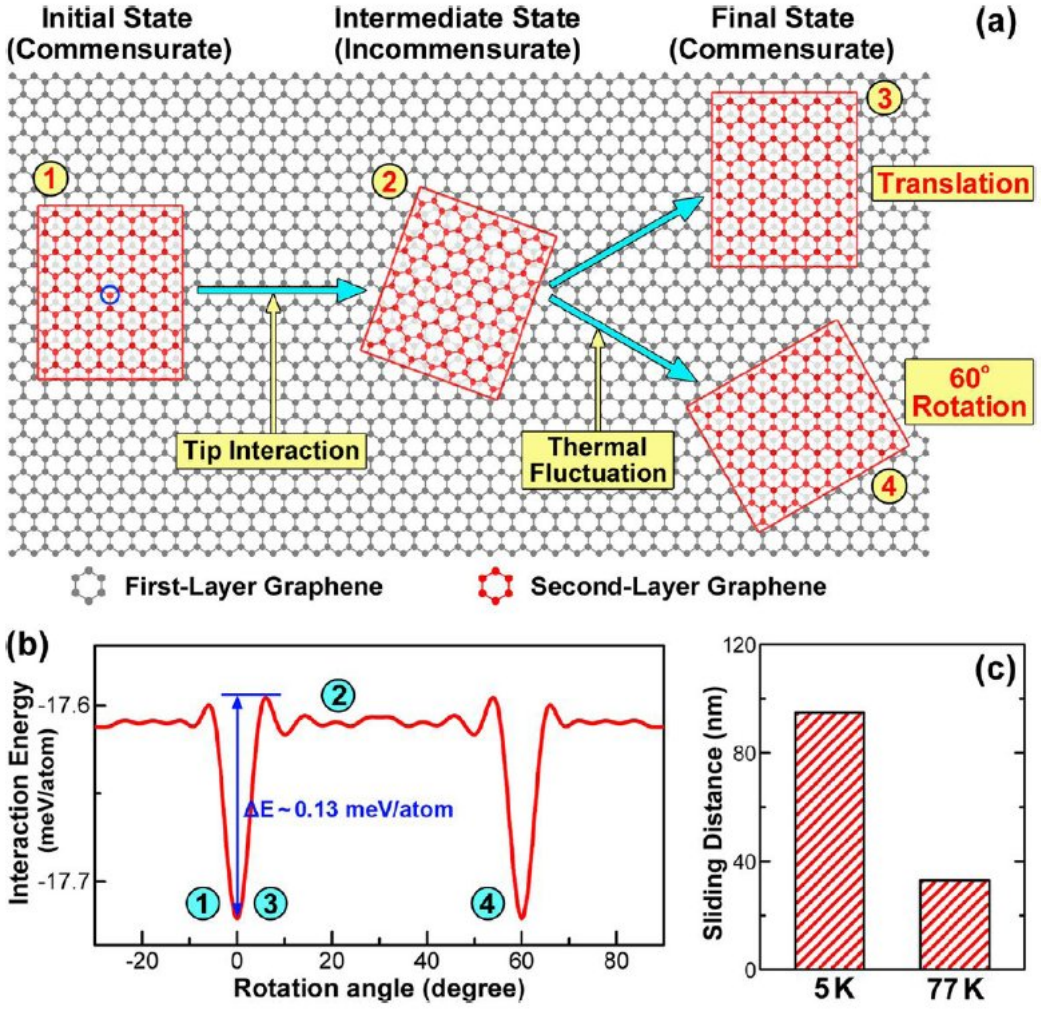

Figure 3.5: Superlubric sliding of graphene nanoflakes on graphene. Panel (a) shows that a flake rotates out of registry, reaching an incommensurate state (the superlubric state) where it can slide until a new commensurate position is reached with either the same orientation or rotated by 60°. The commensurate-incommensurate transition is driven by Van der Waals interactions with the STM tip while the return to a commensurate state is triggered by thermal fluctuations. Panel (b) shows the interaction energy of a graphene nanoflake and a graphene surface as a function of the rotation angle (from [59]). Panel (c) shows the average sliding distance of the flakes at 5 and 77 K. From [127].

state is finally reached (Fig. 3.5a). The rate-limiting step of this diffusion process is the initial commensurate-incommensurate transition.

An important question in this context relates to the mechanism of depinning of the flakes, which can take place either by thermal activation or by interaction with the STM tip. The first experiment was performed at a temperature $T = 77\,\mathrm{K}$, corresponding to a thermal energy $k_b T = 6.6\,\mathrm{meV}$, which is much lower than the commensurate to incommensurate transition barrier for flakes of the size used for this study. This means that thermal agitation is unlikely to activate the depinning process. To confirm this, a second experiment performed at a temperature $T = 5\,\mathrm{K}$ showed that the flakes still performed free sliding.

Instead, it was found that the flake displacements mostly depended on the tip-sample distance: the smaller the distance, the larger the displacements. So it is clear that the Van der Waals interaction between the flake and the tip is responsible for depinning. This interaction in fact results in a vertical displacement of the flakes and a weakening of the interlayer binding, facilitating in this way the transition to incommensurate states.

Once activated to the incommensurate states, the flakes can diffuse before reaching a new equilibrium configuration. Their random sliding directions indicate that the motion of the flakes is not correlated with the scanning direction anymore, but is instead dominated by statistical fluctuations.

A measurement of the stability of the superlubric state is obtained by measuring the average sliding distance of the flakes. Surprisingly, it turns out that the average displacement increases when lowering the temperature.

The lifetime of the superlubric state and the sliding distance are indeed determined by the rate of transition back to the commensurate ground state. Theoretical studies [60] indicate that the stability of the superlubric state depends on the temperature and the flake size, with lower temperature and larger flake size being favourable for superlubric sliding. This is consistent with the observation of a longer sliding distance at lower temperature.

The reason is that thermal excitations increases the statistical fluctuations in the sliding state, so that the flake is more likely to reach commensuration with the underlying monolayer.

3.3.3 The effect of the slider thickness on lubricity

As predicted by the FK model, superlubricity of a nanoscale contact can be achieved if the interface is stiff and incommensurate. In [75], Guerra *et al.* use a realistic nanoscale interface, a gold cluster with a varying number of atomic layers, on graphite, to study how different properties of the slider, such as its thickness and its size, affect the static friction. In particular, they uncover a drop of the static friction both as a function of the slider thickness and the lateral contact size.

The former is in fact related to an increased effective slider rigidity, which improves lubricity of the interface as it reduces the interdigitation between the slider and the substrate. The latter instead is due to the fact that an increased contact area can accomodate a larger number of solitons of the incommensurate moiré pattern, leading to lateral force cancellation, as we will also observe in chapter 4 for our studies of GNRs on gold.

The moiré pattern compensation of regions of smaller and larger interaction energy in fact provides a sampling of the incommensurability of the interface, with the mechanism described in Sec. 3.2, ultimately leading to superlubricity.

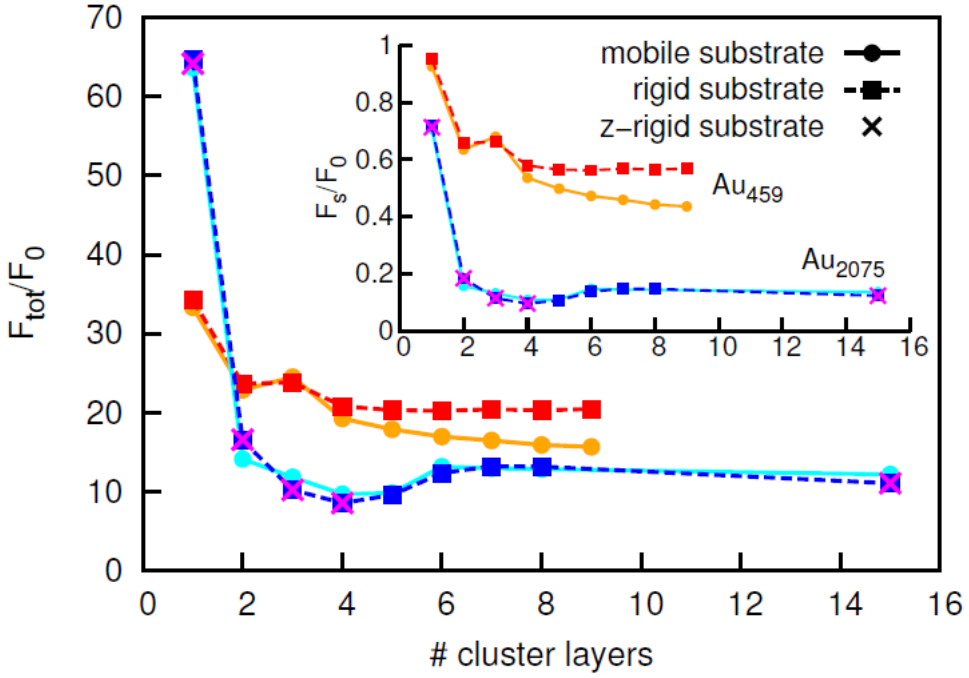

Figure 3.6: Total (main panel) and per-atom (inset) depinning force for $N_1 = 36$ (red/orange curve) and $N_1 = 90$ (blue/cyan curve) as a function of the number of layers from the 2D island up to the 3D cluster ($N = 459$ and 2075 respectively). From [75].

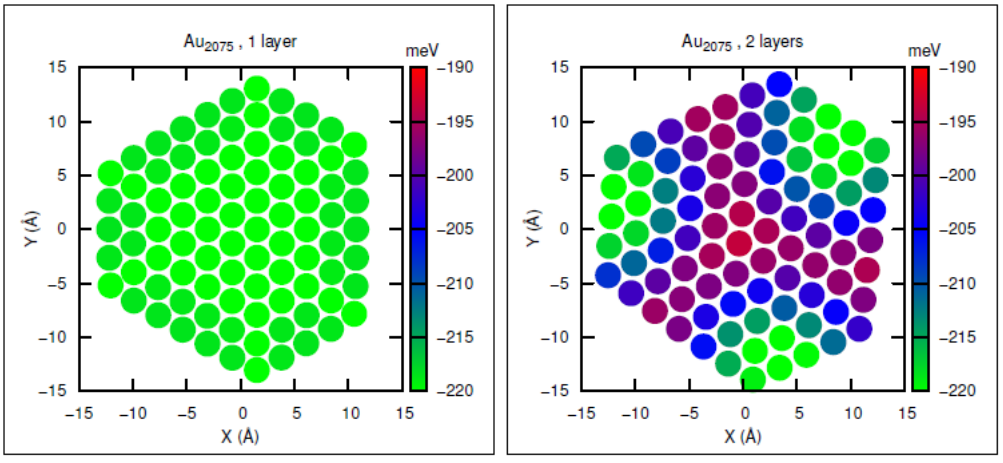

Figure 3.7: Potential energy map of the 90-atom contact of the fully relaxed and force-free Au-C monolayer island ($l = 1$, left) and bilayer ($l = 2$, right). From [75].

The study presented in this section is based on MD simulations of Au nanosliders such as the ones depicted in Fig. 1.7 on graphite. The initial slider is a 2D crystalline Au monolayer of N_1 (ranging from 36 to 90) atoms with a triangular lattice and an hexagonal shape. Subsequently a second atomic layer with N_2 atoms is added on top of the first; then a third layer on top of the second and so on until a full cluster is formed, with $N = N_1 + N_2 + \ldots + N_l$ atoms forming a 3D truncated octahedron deposited on an atomistically simulated graphite substrate.

The structure is first relaxed at a temperature $T = 0$; subsequently an external driving force f_{ext} evenly applied to each Au atom, resulting in a total driving force $F_{\text{ext}} = N f_{\text{ext}}$, is linearly increased with time until depinning takes place at some threshold value $F_{\text{ext}} = F_{\text{tot}}$. In Fig. 3.6 they observe the behavior of the total and per-atom depinning force as a function of the number of cluster layers, reported in units of the single gold atom depinning force $F_0 = 55\,\text{pN}$. The main result here is a striking drop of the static friction with increasing thickness, an effect which is more and more pronounced as they increase the contact area between the cluster and the substrate.

In particular, a reduction of a factor 5 of the total static friction is caused by adding a second layer on top of the contact layer, while further added layers have a much smaller effect. The small increase that they observe by passing from $l = 5$ and $l = 6$ arises from accidentally maximizing te Au-C commensurate regions of the moiré pattern within the size of the contact.

Is is also worth noticing that the effect of the substrate mobility is very limited, as shown by comparison of totally rigid, partially rigid and fully mobile carbon atoms. This suggests that the main effect causing the reduction of the friction force is a decrease of the contact-induced strain in the Au/graphite interface, as shown also by the potential energy map of Fig. 3.7. An Au monolayer appears to be flexible and soft enough to create an almost commensurate configuration with the substrate, while a bilayer, due to its increased rigidity, already generates a moiré pattern characterized by locally commensurate (green) and incommensurate (purple) regions that tend to compensate. This effect is at the origin of the drop in the static friction barrier.

We also notice that the bilayer displays a slightly tilted configuration (by an angle $\theta = 5.5°$) with respect to the monolayer. This effect corresponds to a characteristic Novaco-McTague rotation, whose function is to release part of the misfit compressional stress of the nanoslider into a shear stress, with the final result that the system reaches a more stable equilibrium configuration. A similar phenomenology has also been observed in [36] in the case of graphene nanoribbons (GNRs) on gold, as we will describe in greater detail in chapter 4.

In conclusion, this thickness-dependent static friction force, in particular the strong drop that one observes by just passing from a Au monolayer to a bilayer, suggests the possibility of having an "Aubry-like" transition between a pinned soft island and the much more lubric multilayer cluster by effectively increasing the contact rigidity. This effect of course can take place only for sufficiently extended contact sizes, so that the interface really develops a moiré pattern, whose pinned and unpinned regions can compensate giving rise to a state of low friction.

To further inspect this point, in [75] Guerra *et al.* also studied the dependence of the static friction on the contact size, for an Au island monolayer up to 500 atoms and for clusters with a size up to 2000 atoms. The first result is that, at small contact sizes (up to 200 atoms), Au islands and clusters are commensurate and aligned with the graphite substrate, resulting in a strong pinning. This is confirmed by an initial increase of the static friction force as a function of the contact size.

Once the linear size of the contact roughly corresponds to the typical soliton-soliton distance,

i.e. the distance between locally mismatched and incommensurate regions of the contact area, the static friction rise levels out. In this way both islands and clusters turn incommensurate and much more lubric.

The soliton spacing turns out to be larger in the monolayer than in the case of the multilayer clusters, as a result of the larger compliance of the monolayers with the graphite substrate. This is the reason while e.g for a contact size of $N_1 = 90$ atoms, the 2D island is still pinned, while the 3D cluster is already lubric.

Chapter 4

Graphene nanoribbons on gold: superlubricity and edge effects

The study of the structural and mechanical properties of graphene nanoribbons (GNRs) deposited on gold has been subject of recent intense experimental investigation [34]. Following the basic definition of superlubricity given in Sec. 3.1, Kawai *et al.* have shown via AFM measurements that the average static friction force for GNRs on a Au(111) substrate does not increase with the GNR length, providing an experimental indication of the superlubric character of the interface.

In this chapter, the atomistic nature of the static friction along the longitudinal axis of this system against sliding is studied. By means of numerical simulations and modeling we confirm that the GNR interior is structurally lubric so that the static friction is dominated by the front/tail regions of the GNR, where the residual uncompensated lateral forces arising from the interaction with the underneath gold surface opposes the free sliding. As a result of this edge pinning the static friction does not grow with the GNR length, but oscillates around a fairly constant mean value. These friction oscillations are explained in terms of the GNR-Au(111) lattice mismatch: at certain GNR lengths close to an integer number of the beat (or moiré) length there is good force compensation and superlubric sliding; whereas close to half odd-integer periods there is significant pinning of the edge with larger friction. These results make qualitative contact with these recent state-of-the-art AFM experiments, as well as with the sliding of other different incommensurate systems. Moreover, they highlight the deep connection existing between the longitudinal static friction and the emerging interface moiré pattern. The content of this chapter is part of the published paper *"Graphene nanoribbons on gold: understanding superlubricity and edge effects"*, 2D Materials, **4**, 4, 2017 [36].

4.1 Introduction and experimental motivations

When deposited on a clean flat crystal surface, nano-sized objects usually provide a well-defined mechanical contact. For this and other reasons, systems of this kind have been the subject of extensive nanofriction investigation in recent years both in experiments [55, 56, 126, 127, 132, 133, 134, 135, 136, 137, 138] and in simulations [139, 140, 141]. The gold-graphite interface constitutes an especially smooth and lubric contact, characterized by tenuous lateral forces, which make it an ideal

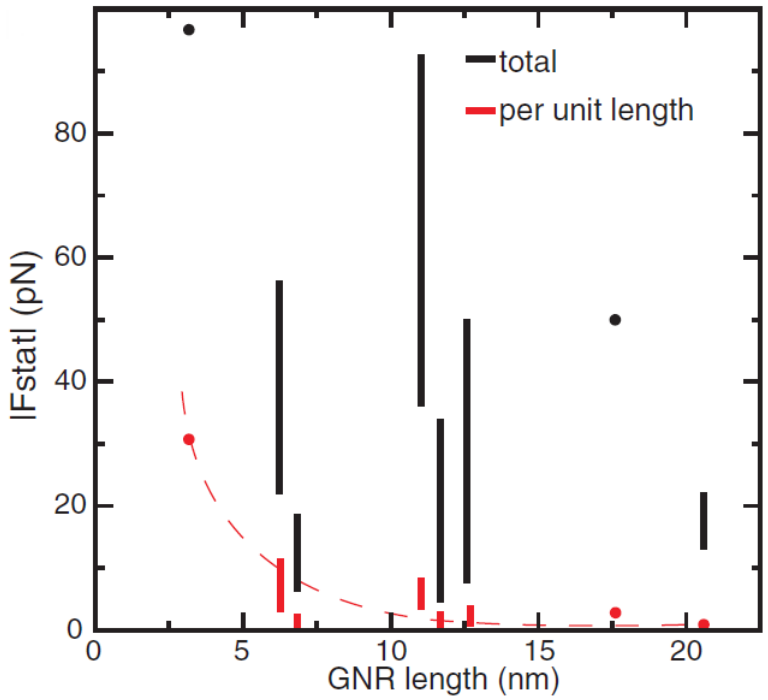

Figure 4.1: Length dependence of the total static friction (black error bars) and the static friction per unit length (red curve) as measured in [34]. The rough independence of the static friction on the GNR length indicates superlubricity.

workhorse system for basic tribological studies. In particular the controlled movements of gold and antimony nanoclusters deposited on the graphite surface provided elegant realizations of structural lubricity [1, 5, 142], leading to interfaces with sliding friction forces growing sublinearly with the contact area [56, 138]. Unfortunately the control over gold nanocluster size and structure is, at best, statistical, and this limitation prevents a precise control of the interface geometry and orientation. More recent work focused on the specular, but better controlled, sliding of graphitic adsorbates, e.g., in the form of graphene nanoribbons (GNRs), on gold substrates, and in particular on the Au(111) surface [34, 143]. State-of-the-art on-surface synthesis techniques allow the construction of GNRs of controlled shape on the gold surface [143, 144], where size and orientation of the nano object can be monitored with atomic resolution by means of tip-scanning microscopy in clean conditions of ultra-high vacuum and low temperature. In addition, the tip of an AFM can easily induce displacements of the GNRs on the surface, thanks to the very smooth GNR-gold interaction. These forced sliding displacements were exploited by Kawai *et al.* [34] to probe the frictional properties of this interface at very-low temperature (4.8 K). That work provides initial evidence for a weak length dependence of static friction, defined as the minimum external force needed to start the longitudinal sliding of the GNRs along their long direction, as shown in Fig. 4.1.

That data are however affected by large error bars, which prevent the clear-cut attribution of the frictional properties. An intervention of theory is therefore called for to clarify the ideal frictional behavior to be expected for these systems.

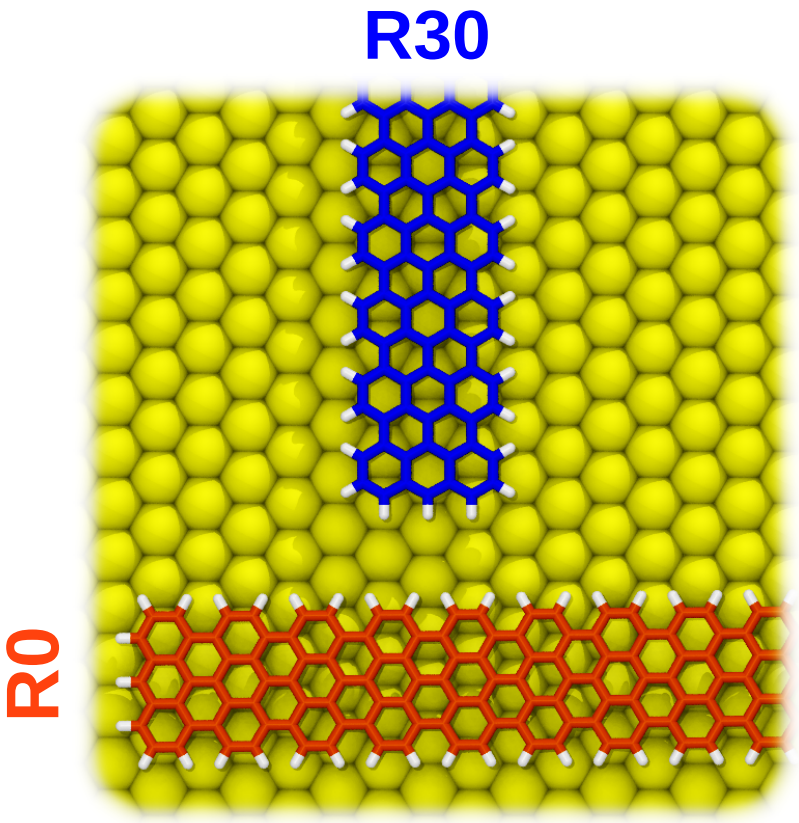

Figure 4.2: Top-view sketch of the R0 (orange) and R30 (blue) alignments of the GNR deposited on the Au(111) substrate (yellow). Broken carbon bonds at front, back, and side edges are passivated by hydrogen atoms (white).

4.2 System and Methods

4.2.1 Lattice structure of the interface and simulation details

Mimicking the experimental geometry [34], we simulate armchair GNRs consisting of a stripe of alternating triplets and pairs of carbon hexagons, as sketched in Fig. 4.2. The resulting GNR width is $\simeq 0.7\,\mathrm{nm}$, while for the GNR length L we investigate the experimentally significant range from $L \simeq 4.2\,\mathrm{nm}$ (10 unit cells, $N_\mathrm{C} = 140$ C atoms) to $L \simeq 60.3\,\mathrm{nm}$ (144 unit cells, $N_\mathrm{C} = 2016$ C atoms).

Our goal is to determine by simulation, and to explain by theory, the static friction force which resists the longitudinal sliding of these ribbons on gold. One complication of real gold (111) surfaces may be represented by reconstruction, both the primary $(22 \times \sqrt{3})$ reconstruction, and the secondary herringbone long-period one [147, 148, 149]. By ignoring these reconstructions (not always present), we extract the simplest and fundamental length dependence of friction on unreconstructed Au(111), represented here by a rigid monolayer triangular lattice with spacing $a_\mathrm{Au} = 288.38\,\mathrm{pm}$.

We investigate mainly two relative alignments of the GNR with the substrate: the R0 epitaxial orientation, in which the GNRs are aligned with the long axis parallel to Au$[1, -2, 1]$ ($\theta = 0$), and the R30 orientation with the GNRs rotated by 30° (or equivalently 90°) relative to R0, namely along

the Au$[-1, 0, 1]$ direction ($\theta = 30°$), see Fig. 4.2. Within our model, depending on the GNR length, the R0 angular alignment turns out to be only weakly locally stable against global rotations, with an essentially flat $T = 0$ total energy landscape over an angular range of approximately $\theta \simeq \pm 5°$. This flatness is probably due to the interplay and mutual cancellation of the spontaneous interface angular misalignment prescribed by the Novaco-McTague theory [72, 145, 146], that for a full graphene monolayer would demand an energy minimum at some small $\theta \neq 0$, and the finite size and elongated shape of the GNR overlayer, favoring perfect alignment at $\theta = 0$. In practice, while in the experiment of [34] the commonest GNR orientation is the R30 alignment, the R0 arrangement seems to be favored in the case of graphene flakes grown, with a different technique, on Au(111) [150]. It is also possible that for the GNRs of [34] the edges might play a role and tilt the tight energy balance in favor of the R30 orientation. We also note that the R30 case is close to a commensuration of 2/3, fostering energetics beside reducing the needs of out-of-plane adjustments (see Fig. 4.4 colorbars). Alternatively, the prevalence of R30 might be a purely kinetic effect of the synthesis method adopted for the GNR [143, 144]. With our model forces, and for large lengths L, the R30 orientation is a local energy minimum of marginally higher energy, approximately 0.008 meV/atom, relative to the R0 orientation. At any rate, we simulate the static friction of both orientations and compare the outcomes.

In our model, the GNR atomistic dynamics is determined by the force field based on the Reactive Empirical Bond Order (REBO) C-C and C-H interaction potential [78] as implemented in LAMMPS [159], plus a 2-body Lennard-Jones (LJ) potential describing the C-Au interaction. Following Refs. [34, 151] we take $\sigma_C = 274$ pm and $\varepsilon_C = 2.5$ meV for the C-Au LJ parameters, which is best adapted to model the mutual corrugation energy of graphitic materials with Au(111) when the latter is represented by a single rigid layer. As is generally the case in experiment, where broken bonds are immediately saturated, we assume all broken bonds of the peripheral C atoms to be H-passivated. Our tests proved that, even within an empirical force modeling where electrons are absent, the lack of H passivation, assumed earlier [34], would produce significantly shorter C-C bond lengths of the graphitic edge, thus compromising a realistic moiré superstructure as well as static friction which, as we shall see, is edge-related. The less important H-Au interaction is also described by a LJ potential with $\sigma_H = \sigma_C$ and $\varepsilon_H = 1.0$ meV. We verified that a variation, by a factor of 2 or 3, in ε_C and ε_H does not affect the overall trend of friction versus size, simply rescaling the overall static-friction curves almost rigidly by the same factor. We also verified that increasing the number of Au layers representing the fcc bulk structure of the gold substrate leads to relatively small changes in the model output, so that these changes can mostly be compensated by a small adaptation of the LJ C-Au and H-Au parameters to fit the experimentally observed frequency shifts profiles recorded during the AFM scans [34]. While the adopted model is far from perfect (in particular the real Au-C interaction is likely more complicated than a simple LJ), we are confident that the most important features are captured by the present model.

To obtain the fully relaxed initial configuration of each GNR on gold we run a Langevin simulated thermal annealing by decreasing the target temperature from $T = 50$ K down to 0 K in 300 ps, at a rate of -0.17 K/ps, and a subsequent damped relaxation at $T = 0$ for a further 200 ps. To prevent thermally-induced rotations of R0 GNRs during this annealing protocol, we cancel their out-of-plane angular momentum during the relaxation dynamics. In addition, the robustness of the relaxation procedure is tested against in-plane displacements of the initial center-mass position, adopting the resulting lowest-energy GNR arrangement as the fully relaxed initial configuration

for the subsequent friction simulations.

Starting from these relaxed configurations, we then evaluate the static friction by means of zero-temperature molecular-dynamics (MD) simulations, by applying an adiabatically increasing external force F^{tot} directed along the GNR main axis. The force can be applied to the GNR center of mass or, it could be applied (as a pulling force), to the GNR leading edge. By directly testing that an edge-driven simulation protocol does not lead to fundamentally different outcomes, as expected for this kind of large material stiffness and small length size [152], we choose here a uniform center-of-mass driving of the GNR, with the same force $F = F^{\mathrm{tot}}/N$ equally acting on all $N = (N_{\mathrm{C}} + N_{\mathrm{H}})$ atoms of the adsorbate. Our protocol is to increase adiabatically F in small incremental steps $dF \simeq 8 \cdot 10^{-5}\,\mathrm{pN/atom}$, letting the system structure relax and the kinetic energy be absorbed after each step before the next. This relaxation procedure is implemented via a viscous damping rate γ, whose specific value (here, $2\,\mathrm{ps}^{-1}$), we checked, does not affect the outcome of the simulated tribological response. We finally estimate the static friction force F_s^{tot} as the smallest force F^{tot} leading to a freely sliding configuration, with the GNR center-mass speed experiencing a frank increase in the pulling direction exceeding $10^{-4}\,\mathrm{m/s}$ in simulation.

4.2.2 Fine-tuning of the parameters

A crucial step in providing a correct MD description of the static properties of an interface and its frictional behavior in turn is the fine-tuning of the parameters to be used in the simulation. The goal is to obtain a correct modeling of the system, which implies a reasonable agreement between the phenomenology resulting from the simulations and the one observed in experiment and a numerical correspondence of some physical quantities with existing data, that can be used as a benchmark.

In the case of the GNRs on gold, the free parameters that have to be fixed are the LJ amplitudes ε_C and ε_H of the C-Au and H-Au interaction, the characteristic lengths σ_C and σ_H of the C-Au and H-Au interaction and the damping γ of the $T = 0$ Langevin bath.

Following the procedure used in [34], the value of $\sigma_C = 274\,\mathrm{pm}$ allows to reproduce the GNR adsorption distance on gold $d = 320\,\mathrm{pm}$ obtained from previous DFT calculations with van der Waals corrections [153]. The same procedure will be used also in chapter 6 to obtain a good agreement between the pull-off forces measured in the simulated and the experimental vertical dynamics of GNRs on gold.

In principle, the value of σ_H could be set independently of σ_C. Still, it turns out that the hydrogenation of the edges is only relevant to reproduce the correct C-C bond length along the GNR long edges, that are sensitive to saturation effects. It was indeed observed that the absence of the hydrogens tends to produce a significant increase of the C-C average equilibrium distance close to the edges, with a total distorsion of the moiré superstructure. However, it was found that a change of the σ_H in a reasonably wide range of values ($1.0\,\mathrm{meV} < \sigma_H < 2.5\,\mathrm{meV}$) does not significantly affect the simulated frictional response, in particular the observed moiré-related periodicities of the static friction curves.

Setting the values of the LJ amplitudes $\varepsilon_C = 2.5\,\mathrm{meV}$ and $\varepsilon_H = 1.0\,\mathrm{meV}$ is in general a more problematic task. In this case it is possible to exploit the information related to the frequency shift traces coming from experiment. As we will see in greater detail in chapter 5, the procedure

used in the experiment to produce depinning and subsequent lateral sliding of the GNR consists in using an AFM tip attached to one short edge of the GNR to lift it up to a given height upon the gold substrate and then drive it laterally forward or backwards. Recording the frequency shift of the AFM during the lateral driving makes the information related to the instantaneous kinetic friction force available.

The values of the C-Au and H-Au LJ amplitudes are then set in such a way as to obtain a quantitative agreement between the amplitude of the simulated and the experimental frequency shift trace (see Fig. 5.2). More details on how this procedure is performed will be given in 5.

With these precise values of ϵ_C and ϵ_H however we greatly underestimate the adhesive energy per C-atom of the GNR. This issue suggests that modeling the adhesive interactions of GNRs on gold with pure two-body Lennard-Jones potentials is in general not sufficient to obtain a full quantitative agreement with experiments. This is because the small number of free parameters of these potentials do not allow to match independently the binding energy and the corrugation of an interface. More complex and possibly anisotropic potentials of interaction have been proposed to tackle this delicate issue for graphene/h-BN heterostructures [158].

Still it is important to note that the static friction forces that result from the simulation with these values of ϵ are of the same order of magnitude of the ones obtained in the experiment, i.e. in the range of tens of pN, as confirmed by Fig. 4.3a.

Moreover, it was checked that a change in ε_C and ε_H just produces an overall shift of the average static friction force behavior as a function of the GNR length. where an increase in ε_C and ε_H increases the average friction. However, the independence of the static friction force on the GNR length is still satisfied upon changing the value of ε_C and so the superlubric character of the interface, thus confirming that LJ interactions still allow a qualitative agreement between theory and experiment for our case study.

Since in this work we are dealing with the static "equilibrium" properties of the GNR/gold interface, the precise value of the damping parameter γ should not be a major concern. In fact, it was checked that a change of this value does not produce any significant difference in the values of the measured static friction forces.

Still, the large value of $\gamma = 2\,\mathrm{ps}^{-1}$ makes the observation of the depinning transition of some GNRs problematic. In particular, the GNRs whose length correspond to minima of the static friction force in Fig. 4.3a depin with a very low and γ-dependent speed. In fact, even in the case of a pure viscous motion the GNRs would reach a state of uniform motion at constant velocity equal to $v_{\mathrm{lim}} = F/\gamma M$, where F is the uniform force applied on the GNR and M the total mass of the GNR. This means that choosing a large value of γ might even cause the depinning velocity to be smaller than the cutoff velocity $v_{\mathrm{cut}} = 10^{-4}\,\mathrm{m/s}$ used to detect a freely sliding configuration.

This is what happens in practice for the most lubric GNRs. For these specific GNRs it is necessary to slightly change the simulation protocol to detect the depinning force: the value of the damping parameter is decreased by 5 times, while at the same time we impose that the GNR is displaced by the applied force by a distance of at least three unit cells of the gold substrate after depinning. This makes the depinning transition far more abrupt in the simulations, while the constraint applied on the total displacement really ensures that GNR has reached a freely sliding state.

4.3 Static friction of GNRs on gold

4.3.1 Size-scaling of the static friction force

Fig. 4.3a reports the total static friction force, $F_s^{\rm tot}$, as a function of the GNR length for the R0 and R30 orientations. These results show that the R0-oriented GNRs exhibit a small static friction ($\sim 20-50\,$pN), which nonetheless is always systematically larger compared to R30-oriented GNRs ($\sim 5\,$pN). Interestingly, for both orientations, Fig. 4.3a displays periodic-like oscillations of $F_s^{\rm tot}$ as a function of L, without any systematic increase. Compatible with the experimental observations of [34], this result is consistent with a *per atom* $F_s = {\rm const}/L$. Static friction per particle decreases as a function of the GNR length, indicating an asymptotically vanishing friction per unit area of contact, the characteristic hallmark of a superlubric tribological contact. For the graphene-gold interface, characterized by a fairly weak graphene-Au(111) interaction, very stiff in-plane C-C bonds, and mutually mismatched periodicities, one does indeed expect a structurally lubric behavior, which here emerges even for GNRs, finite-width graphene ribbons. The independence of the total static friction for the whole GNR from the length L shows that there is no term linearly proportional to the contact area, the very definition of superlubricity [1, 5].

4.3.2 Static friction periodicities and relation with the moiré pattern

The observed oscillation of $F_s^{\rm tot}$ can be explained as a consequence of ribbon-specific moiré pattern induced by the lattice-spacing mismatch. Fig. 4.4 shows typical moiré patterns, those of a 30 nm-long relaxed GNR physisorbed along both R0 and R30 orientations. Here the moiré gives rise to, and is mapped by, vertical displacements z of the individual C atoms. They are mapped in contrasting colors, exhibiting quasi-periodic color patterns whose average periods $\lambda_m^{\rm R0} = 2.64\,$nm and $\lambda_m^{\rm R30} = 4.86\,$nm are highlighted. Lower-z regions (red) contribute more, and higher up segments (blue) contribute less to the total (negative) binding energy E_b of the physisorbed GNR. Due to the overall periodicity of the moiré-pattern envelop, in the GNR "bulk" interior these oscillations compensate, so that, on average, E_b grows linearly with L. There remains a residual oscillating contribution ΔE_b to E_b, which depends on the length of the short terminating section, namely the GNR part exceeding an integer number of moiré average wavelengths λ_m. It is precisely this short residual section of the GNR, whose contribution to energetics does not grow with L, that dominates the static friction force $F_s^{\rm tot}$. Indeed, periodically in L, the GNR terminations explore configurations ranging from a locally best matching (a minimum of ΔE_b, with larger $F_s^{\rm tot}$) or compensated (equally weighting red/blue areas, generating a local maximum of ΔE_b, and a small $F_s^{\rm tot}$) arrangement. The anticorrelation of $F_s^{\rm tot}$ with ΔE_b atom is illustrated by comparing the panels of Fig. 4.3.

The moiré patterns arise out of the mismatch between the GNR lattice spacing, $a_{\rm GNR} = 420.00\,$pm, and the spacing of the gold surface being $a_{\rm Au} = 499.49\,$pm for R0, and $a_{\rm Au} = 288.38\,$pm for R30. The resulting mismatch ratios are $\rho_{\rm R0} = 0.8408 \simeq 1$ and $\rho_{\rm R30} = 1.4564 \simeq 3/2$, respectively. The wavelengths of the R0 and R30 moiré oscillation patterns [70, 146, 160, 161] are $\lambda_m^{\rm R0} = a_{\rm GNR}/(1-\rho_{\rm R0}) \simeq 2.64\,$nm, and $\lambda_m^{\rm R30} = a_{\rm GNR}/(3-2\rho_{\rm R30}) \simeq 4.82\,$nm. For the R0 orientation, the oscillation period should be approximately $\lambda_m^{\rm R0} \simeq 6\,a_{\rm GNR}$; however, the main friction oscillation observed in Fig. 4.3a exhibits a period $\frac{1}{2}\lambda_m^{\rm R0} \simeq 3\,a_{\rm GNR}$. The zig-zag nature of the R0 moiré patterns (see Fig. 4.4) explains this discrepancy: the projection of moiré pattern along the

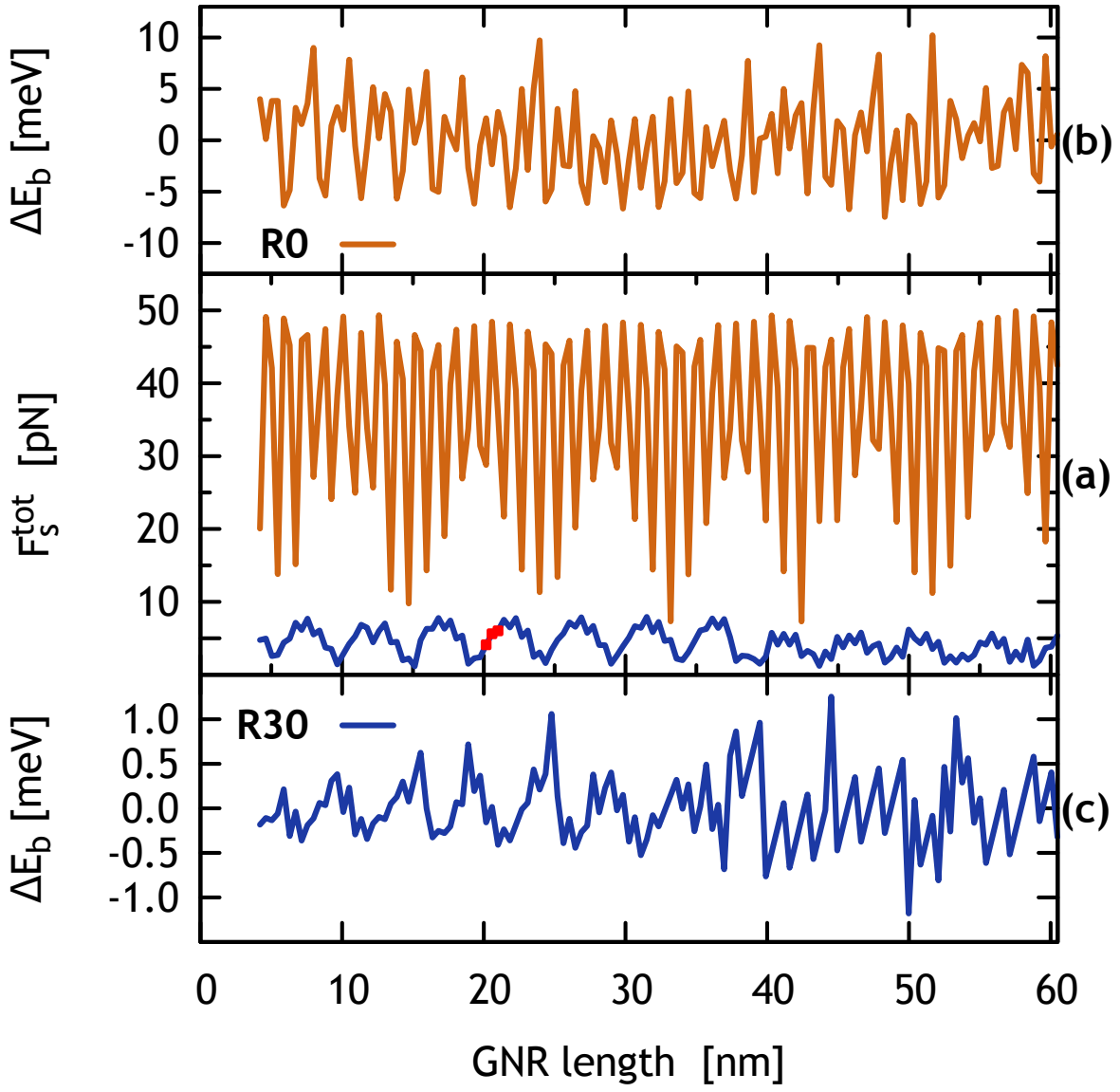

Figure 4.3: Dependence on the GNR length L of the computed total static friction force (a), and of the variation of the total adsorption free energy with respect to its linear fit (b) and (c). The GNR orientations are R0 (orange, $\theta = 0$) and R30 (blue, $\theta = 30°$). The linear fits are $E_b = pL + q$, with $p = -345.735$ / -345.891 meV/nm and $q = -34.5197$ / -21.1741 meV for R0 / R30 respectively. Red symbols mark the values for the GNRs of Fig. 4.6.

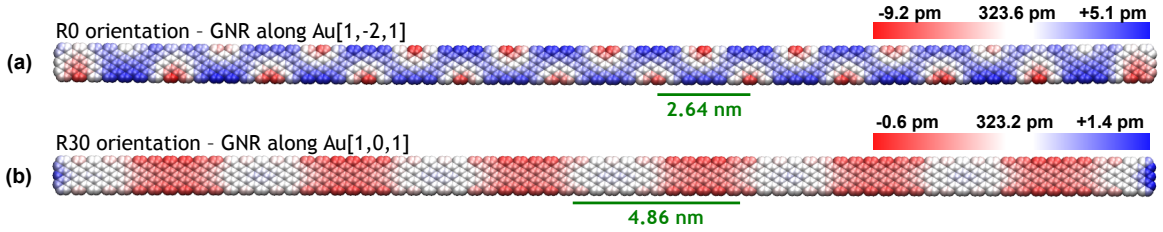

Figure 4.4: The relaxed GNR configuration of the 30 nm-long GNR in the R0 (a) and R30 (b) orientations relative to the underlying Au(111) surface (not shown). The color of the C atoms maps their vertical displacement relative to the GNR average height (passivating H atoms are not shown). The wavelength λ_m of the moiré pattern, as extracted from the lattice-mismatch value, is indicated for each orientation.

GNR axis leads to an halved periodicity. For the R30 case, the moiré wavelength λ_m^{R30} accounts for the relatively slow oscillation in F_s^{tot} and ΔE_b displayed in the blue curves of Fig. 4.3.

One can model the dependence of F_s with the GNR length L, as if it was solely related – as in a purely rigid system – to the uncompensated part of the moiré pattern of period λ_m [162, 163]. In the GNR, whose bulk is superlubric, this part is exclusively related to the nanoribbon edges – chiefly the front and the trailing edges, as the effect of the side edges for longitudinal applied driving turns out to be negligible. We can model this uncompensated length, and thus its contribution to the friction force, with a simple sinusoidal oscillation of period λ_m as a function of L [163]:

$$F(L) = \alpha + \beta \sin\left(\frac{2\pi L}{\lambda_m} - \delta\right), \tag{4.1}$$

where α, β, δ, and λ_m are fitting parameters. Fig. 4.5 reports the curves of 4.1 best-fitting the F_s data of Fig. 4.3a. For the R0 and R30 cases the fit yields $\lambda_m = 1.32\,\mathrm{nm}$ and $\lambda_m = 4.86\,\mathrm{nm}$ respectively, indeed matching the measured moiré nominal wavelengths (see Fig. 4.4). The long-wavelength modulations seen for R0 in Fig. 4.3a are now explained clearly by the simple sinusoidal fitting function of Fig. 4.5a: these modulations are the trivial result of a poor sampling rate close to the Nyquist limit, an aliasing-type effect due to $\frac{1}{2}\lambda_m^{\mathrm{R0}}$ being close, but not quite equal, to $3\,a_{\mathrm{GNR}}$. In the R30 orientation, this effect is not visible since sampling is much denser, $\lambda_m \gg a_{\mathrm{GNR}}$, preventing any aliasing effect.

We note that the close correspondence of the nominal mismatch with the moiré "periodicities" in real systems can be perturbed by relaxation-induced strains and by thermal expansion. In the case of graphene, which exhibits a large in-plane stiffness, such strains are severely limited and will mainly influence only the higher-order approximants, i.e. large distances over which deformations tend to accumulate. In both cases, R0 and R30, deviations from this simple sinusoidal model can be attributed to the non-rigid nature of the simulated GNRs, and to the fact that the uncompensated GNR length does not contribute precisely as a sine of L. We have repeated the friction simulations with rigid GNRs, with the atomic reciprocal positions frozen in their configuration fully relaxed in vacuum, i.e. away from the gold surface. The computed F_s^{tot} values are indeed quite similar, with typical deviations of the order of 10%. One should not take the oscillating function of eq. (4.1) as a serious model predicting the precise frictional force experienced by a GNR of a given length, but rather as a simple interpolating formula expressing the main message of the present work: the total static friction force needed to set a GNR in motion is totally edge-related, and does not grow

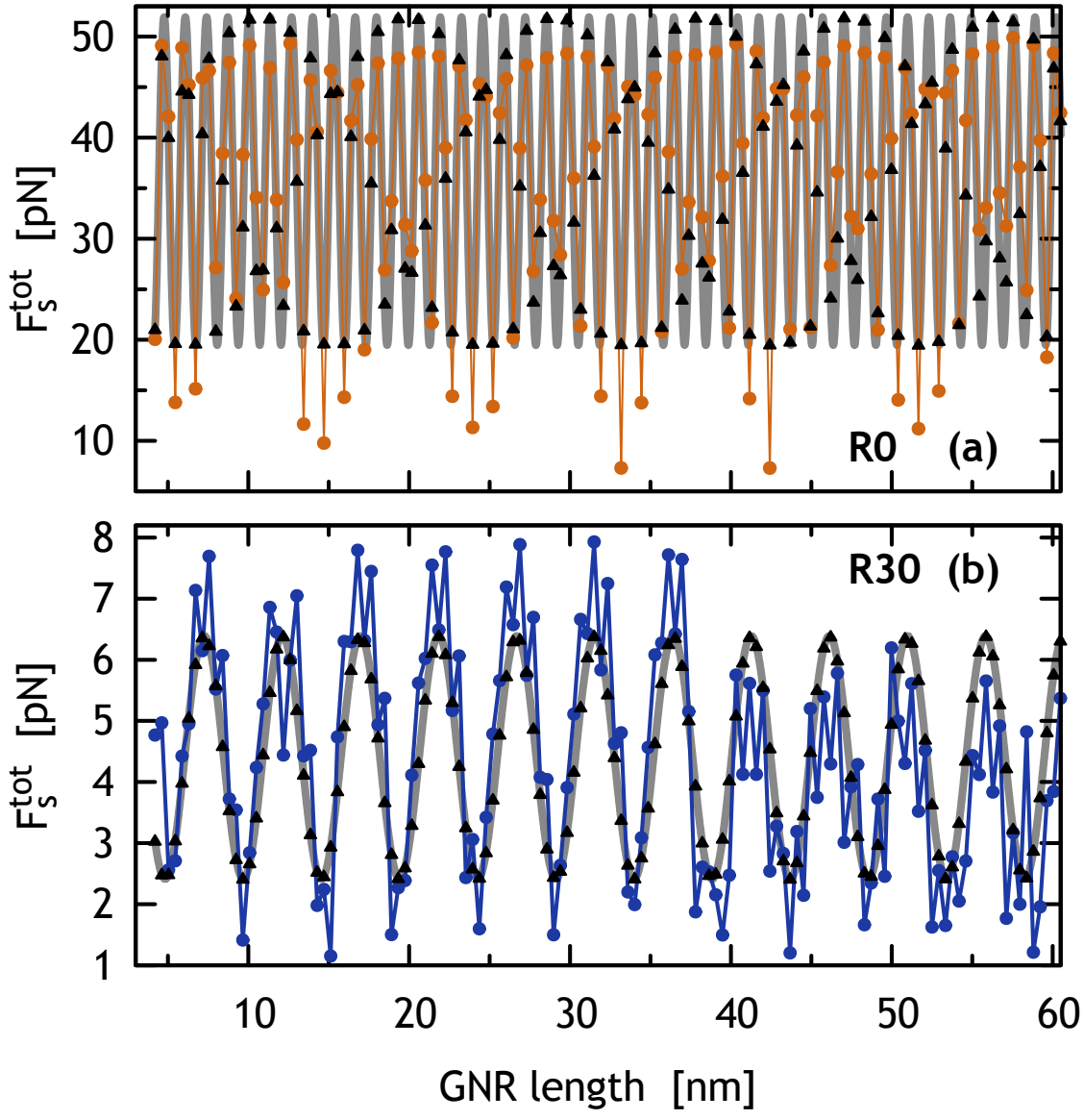

Figure 4.5: A comparison of the L-dependence of the total static friction force F_s (as in Fig. 4.3a) for (a) R0 and (b) R30 orientation (circular dots), with the best-fitting curves of 4.1 (gray) evaluated at the lengths of actual GNRs (triangles).

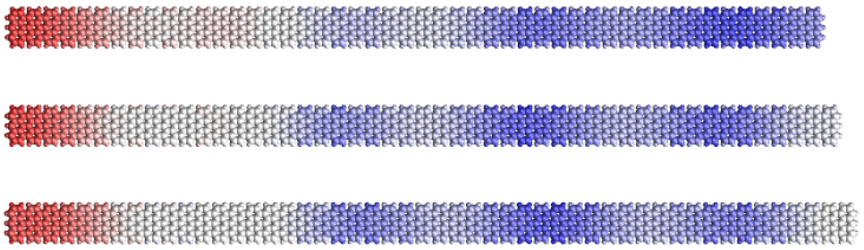

Figure 4.6: Colored strain maps for three R30 GNR of $L \simeq 20{-}20.8\,\mathrm{nm}$ ($N_\mathrm{C} = 672, 686, 700$), highlighted by red symbols in Fig. 4.3a. The map portrays the atomic displacement component (red = small displacement, blue = large displacement) in the pulling-force direction, relative to the fully-relaxed initial configuration evaluated, for each GNR, under an uniform external force strength equaling 75% of the corresponding static friction threshold F_s^tot as reported in Fig. 4.3a. While the central "bulk" GNR region clearly exhibits a large mobility, reflecting structural lubricity, shear resistance and pinning are localized at the nanoribbon ends (here, the GNR tails). The calculated static friction threshold turns out to be roughly proportional to the extension of this boundary red-blended region of the GNR, originating from the corresponding uncompensated part of the moiré superstructure of the relaxed configurations.

with its length, but rather oscillates as the residual length of the end section of the GNR exceeding an integer number of moiré wavelengths.

4.3.3 The pinning centers: the role of the edge

As a confirmation that the main actors responsible for GNR friction are the end sections, responsible for the uncompensated part of the moiré pattern, Fig. 4.6 shows the atomic displacements of the GNR atoms in the pulling direction when the applied driving has reached 75% of the depinning threshold of each of the three GNRs. In this picture, the red-colored regions are those resisting shear. These sections of $\sim \frac{1}{2}\lambda_m \simeq 1{-}2\,\mathrm{nm}$ near one or both of the GNR short ends (depending on the moiré of starting relaxed configuration) show up as the main responsible for GNR pinning. The blue-colored central "bulk" GNR region is ready to slide freely if it was not retained by the stiff elastic interaction with the pinned end section. It is therefore established that the short ends, the front end and the trailing end, represent the source of GNR pinning. Their relative effectiveness and positioning (front versus tail) depends on the GNR length in determining how well the matching conditions are realized at and near these edges. Similarly to what observed in other investigated tribological systems, yet with different geometries [70, 104, 162, 163, 164, 165, 166], we have a final confirmation that the approximately periodic oscillatory trend of F_s^tot as a function of L shown in Fig. 4.3 is a consequence of the periodically varying size of the pinning end region.

4.3.4 Depinning

As soon as the pulling force exceeds the threshold F_s^tot, the GNR starts to move. While this depinning occurs uneventfully in the R30 orientation, we observe, interestingly, that the GNR initially aligned at R0 twists away from the $\theta = 0$ orientation, choosing randomly a small (few degrees) clockwise or counterclockwise angle θ. While twisting, and subsequently in the depinned state, GNRs start to slide at an angle $\pm 30°$ away from the pulling force, namely along one of the Au$[-1, 0, 1]$ directions, which is the same direction where R30-aligned GNRs are pulled. For the

shorter GNRs, this twisting at depinning is an essentially rigid rotation, while it involves small but visible elastic deformations of GNRs with length $L > 30\,\mathrm{nm}$. The reason for this directional locking is that the small twist promotes the formation of 30°-oriented flat "channels" or "troughs" in the 2D translational energy profile for the center of mass of the GNR, which is then led to follow these channels where it encounters quite small barriers against sliding [167]. Experimentally, such predicted tendency to directional locking could be challenging to observe with an AFM, whose force cannot easily be applied to the center of mass. If observed, it would be remarkable.

4.4 Conclusions

In [36] we have presented a study of the static sliding friction of graphene nanoribbons on a metal surface, performed by classical MD simulations. Although with no pretense of quantitative predictive power, our model study appears to capture the essence of their depinning physics. Paralleling experimental results such as those by Kawai *et al.* [34], we find a small friction, strongly-oscillating and basically periodic with zero average increase upon increasing GNR length, supporting superlubricity in this system. The GNR static friction is entirely edge-related, whereas the GNR interior is superlubric, much like in a finite-size FK chain [70, 164, 165], or in other incommensurate interfaces [104, 162, 163, 166]. Specifically, simulations allow us to correlate the periodicity of frictional oscillations to the characteristic length of the moiré pattern, and in particular to the oscillating size of incomplete periods, namely the front and tail edges, which are responsible for the friction. This interpretation suggests that GNRs of certain "magic" lengths matching an integer number of moiré wavelengths λ_m could be selected for ultra-low-friction applications.

Chapter 5

Lifted GNRs: from smooth sliding to multiple stick-slip regimes

In chapter 4 we study the superlubricity of GNRs on gold and explain how this intriguing frictional phenomenon is closely connected to the static "equilibrium" properties of the interface, such as the moiré pattern compensation and the edge-related nature of the static friction barrier.

In this chapter instead, we study the frictional non-equilibrium properties of the GNRs, i.e. the dynamics that arises as a consequence of a lateral driving of the GNRs. To this purpose, we conduct classical simulations of frictional manipulations for a 30 nm long GNR, one end of which is pushed or pulled horizontally while held at different heights above the Au surface, so as to mimick the nanomanipulation provided in the experiments [34] by an AFM tip.

We predict a remarkable transition from smooth sliding to atomic stick-slip, characterized initially by single slips, and then by multiple slips at larger lifting heights. Specifically, the periodicity of the stick-slip dynamics is dominated by the bending elasticity of the GNR, which enables larger slip distances at larger heights. Moreover, the onset of an asymmetric dynamical behavior between forward and backward sliding is explained in terms of the augmented softness of the GNR at larger heights, which plays opposite roles for the two driving directions, decreasing (forward) and increasing (backward) the GNR/substrate adhesion.

This chapter is based on the published paper *Lifted graphene nanoribbons on gold: from smooth-sliding to multiple stick-slip regimes*, Nanoscale, **10**, 2073-2080, 2018 [37].

5.1 Introduction and experimental motivations

The science of nanoscale friction, a property of moving nanometer-sized interfaces widely investigated experimentally by atomic force microscopy (AFM), is progressively unveiling the detailed mechanisms which affect the mechanical energy dissipation in well-controlled frictional setups [1, 2, 5, 122, 169]. Graphene is an important actor in this quest, because its strong resilient structure makes it possible to push and slide flakes and planes once deposited on suitable well-defined surfaces [126]. Graphene nanoribbons (GNRs) too can be created and physisorbed on Au(111) surfaces, by means of clever in-situ molecular-assembly techniques [77, 168]. Once there,

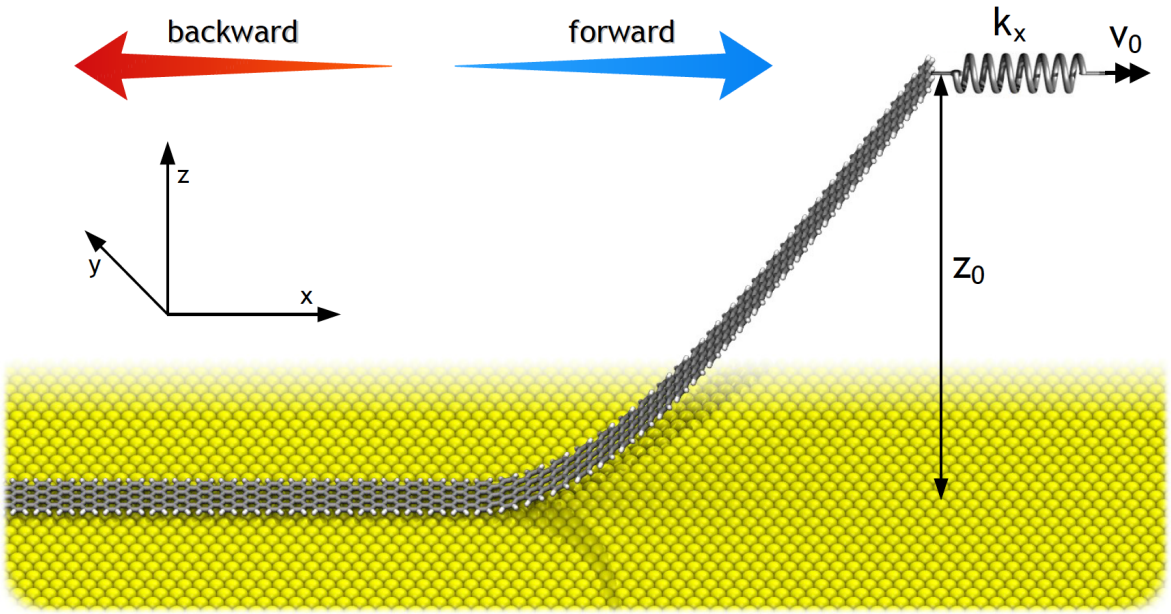

Figure 5.1: Schematic description of the setup used to simulate the AFM tip lifting the GNR at one end and pulling it laterally. One side of a soft spring is attached to the lifted end of the GNR, the other side is moving at constant positive or negative velocity, thus dragging the GNR forward or backward. The height z_0 of the lifted end is kept fixed in the simulations (see Method).

they can be picked up at one extreme and forced to slide by a moving tip [34]. The dynamics of the GNR once dragged forward and backward (calling forward the pulling, backward the pushing, as sketched in Fig. 5.1) may show distinct regimes of motion depending on the lifting height, z_0. At small lifting heights ($z_0 = 1$–3 nm) there is an almost symmetric behavior between forward and backward scans, not unlike that observed experimentally for the low-lifted GNR [34]. At larger heights ($z_0 = 4$–5 nm), different stick-slip patterns and periodicities emerge with a substantial asymmetry between the two (see Fig. 5.2).

The present theoretical study aims at understanding the main features of frictional dissipation in these systems.

Anticipating our final conclusions, the forward-backward symmetric frictional response at small lifting heights stems from the limited extent of elastic deformations accumulated by the GNR when pulled against an energy barrier. At increasing lifting height, the bending energy required to deform the GNR decreases and the mechanical response under driving becomes different for the two opposite scan directions. Once the GNR reaches the minimum energy needed to initiate sliding (the Peierls-Nabarro barrier [70]), its dynamics starts to develop asymmetric features in the emerging stick-slip regime for forward and backward pulling. The main effects of this enhanced elastic deformation are an increased period of the stick-slip motion and the occurrence of a possible "peeling" effect in the backward trace for increasing lifting height.

Since thermal effects are always expected to be quite relevant when dealing with nanoscale systems and depinning mechanisms, we recall that the very low experimental temperature ($T = 4.8$ K) [34], excludes here a possible significant thermal contribution in the observed phenomenology.

In addition, we show that the peaks of the time-resolved frictional force traces depend critically on the effective contact length of the GNR section still adhering to the substrate. The force peak

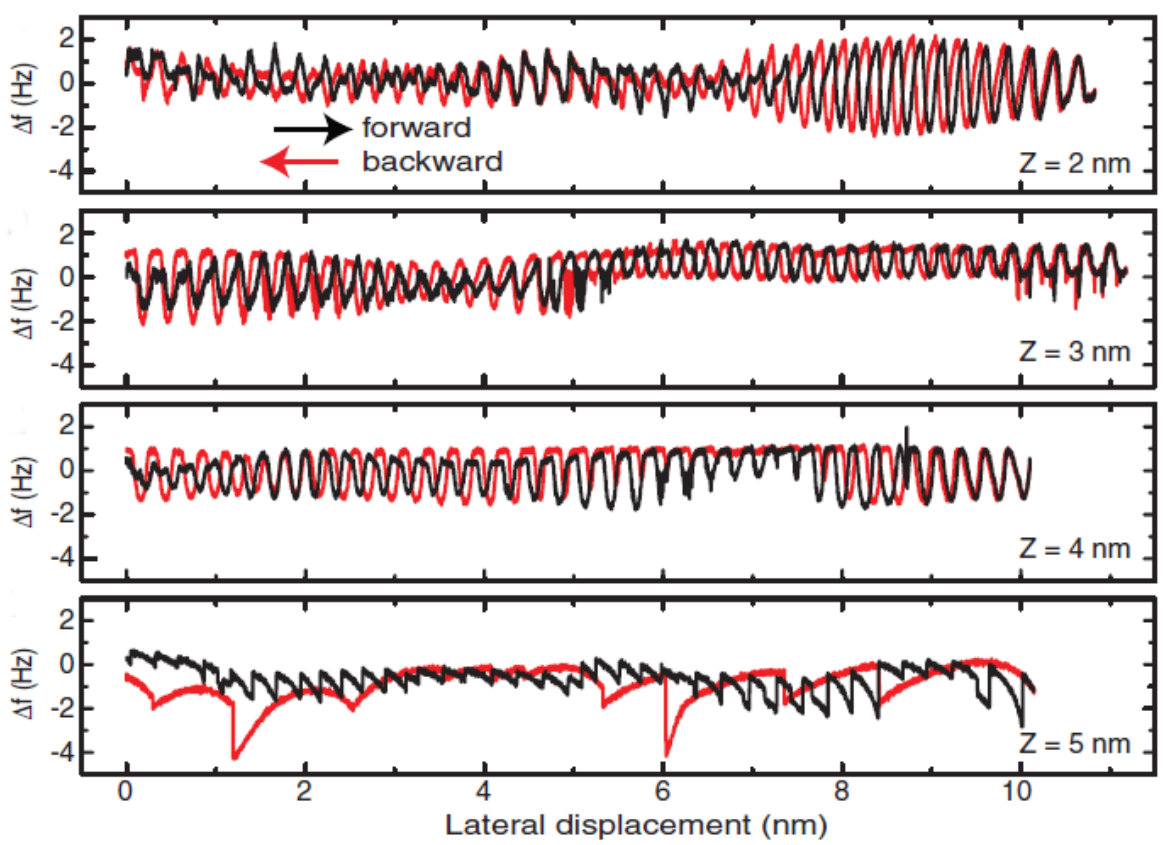

Figure 5.2: Frequency shift traces recorded for lifted GNRs in [34] at four distinctive lifting heights: $z_0 = 2, 3, 4, 5$ nm. The traces indicate a symmetric sliding between the forward and backward sliding up to 4 nm of height, while at 5 nm an asymmetry between the two sliding directions emerges. The long-wavelength modulation of this frequency shift traces is due to the gold substrate reconstruction.

amplitudes exhibit an oscillation versus effective length of the GNR, mostly due to the imperfect compensation of the moiré superstructure at the two ends of the physisorbed part of the GNR. This effect is also related to the oscillatory behavior of the static friction force versus size reported in the past for totally adhering GNRs [36].

5.2 Lateral sliding of a GNR - simulation details

We simulate a $N = 7$ armchair GNR, consisting of a stripe of alternating triplets and pairs of carbon hexagons, of width $\sim 0.7\,\mathrm{nm}$ and length $\sim 30.2\,\mathrm{nm}$, namly a factor $\simeq 5$ longer than in our reference experiment [34]. This length enables us at the same time to reproduce qualitatively the behavior of the force traces at small lifting height z_0 obtained experimentally with a much shorter GNR, and to anticipate phenomena that should come into play when the lifting height is sufficiently large ($z_0 > 5\,\mathrm{nm}$), a regime where GNRs will undergo important elastic deformations. All the edge C-atoms at the periphery of the GNR are passivated with hydrogens, in order to reproduce faithfully the experimental conditions [34], and to obtain realistic peripheral C-C bond lengths, which are sensitive to saturation effects.

The simulated GNR is deposited on an unreconstructed Au(111) surface along the R30 direction, i.e. the GNR long axis lies parallel to the Au$[-1, 0, 1]$ crystallographic direction [36]. The atomistic dynamics of the GNR is simulated using the LAMMPS package [159] by means of a REBO force field [78] for C-C and C-H interaction, plus 2-body C-Au and H-Au interactions of the (6-12) Lennard-Jones (LJ) type, as parametrized in [36]. In the following we refer to these energy contributions to the total energy as V_{REBO} and V_{LJ}, respectively.

Starting from a fully relaxed GNR configuration, we lift progressively one end row (three C atoms) of the GNR through a fictitious ultra-hard spring ($k_z = 1.6 \cdot 10^5\,\mathrm{N/m}$), producing unilateral detachment up to a desired height $z_0 = 1$–$13\,\mathrm{nm}$, followed by a further relaxation in the lifted geometry. We note that the assumption of a very stiff normal spring k_z, representing experimentally the effective spring constant of the "series" of the cantilever vertical mode, of the tip apex elasticity, and of the tip-GNR bonds, allows us to better highlight the distinct dynamical behaviors of the system at almost constant values of the vertical z-coordinate. Numerical simulations with much softer k_z values (see Sec. 5.4) show, anyway, equivalent tribological trends.

z_0 is defined relative to the unlifted GNR configuration. After lifting, the mean coordinate of the lifted end of the GNR, while held all the time at its fixed height z_0, is connected to a soft horizontal pulling spring ($k_x = 1.5\,\mathrm{N/m}$) and dragged forward or backward with constant velocity $v_0 = \pm 0.5\,\mathrm{m/s}$. This procedure aims at mimicking, at least qualitatively, the lateral manipulation of a GNR, as done in AFM experiments [34].

While the real-time evolution of the underlying Au substrate is not explicitly simulated, the GNR C and H atoms obey a dissipative Langevin dynamics, at zero temperature and damping parameter $\gamma = 0.01\,\mathrm{ps}^{-1}$, which prevents the externally-driven nanoribbon from heating up. We checked that the specific adopted γ value ensures a realistic relative balance of inertial and dissipative terms. Still, simulations with no external damping show that the stick-slip behavior of the GNR has no clear periodicity, due to the visible longitudinal oscillations of the GNR after the slip events. These undamped oscillations cause heating up of the interface and destroy the stick-slip periodicities. On the contrary, simulations performed with a much larger damping hide the observed

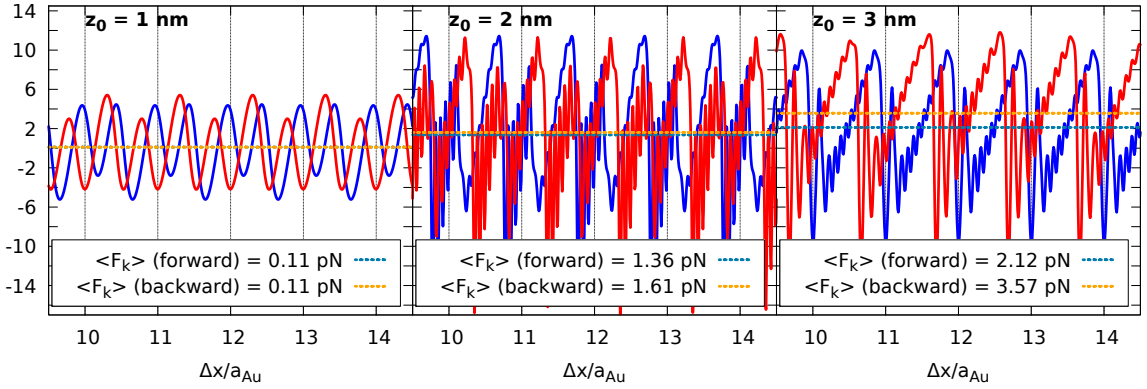

Figure 5.3: Frictional force for GNR sliding at relatively small lifting heights $z_0 = 1$–$3\,\mathrm{nm}$. The blue and red solid curves refer to the forward and backward sliding, respectively. Dotted curves report the corresponding average frictional values.

competition between local bending and corrugation of the interface. In fact, high damping produces an unphysical viscous motion of the GNR at all heights, completely destroying the transition from smooth sliding to stick-slip. The γ value does not significantly affect the qualitative outcome of the simulated tribological response within a quite broad range of values.

The equation of motion for each of the three C atoms of the lifted edge reads:

$$m_{\mathrm{C}}\ddot{\mathbf{r}}_i = -m_{\mathrm{C}}\gamma\dot{\mathbf{r}}_i - k_z(z_i - z_0)\hat{\mathbf{z}} - k_x(x_i - v_0 t)\hat{\mathbf{x}} - \nabla_{\mathbf{r}_i} V(\mathbf{r}_i, \{\mathbf{R}_{\mu'}\})\,. \tag{5.1}$$

$\mathbf{r}_i = (x_i, y_i, z_i)$ $(i = 1, 2, 3)$ are the positions of the three C-atoms of the lifted edge. $\hat{\mathbf{x}}$ and $\hat{\mathbf{z}}$ the unit vectors directed along the x- and z-axis. $V(\mathbf{r}_i, \{\mathbf{R}_{\mu'}\}) = V_{\mathrm{REBO}}(\mathbf{r}_i, \{\mathbf{R}_{\mu'}\}) + V_{\mathrm{LJ}}(\mathbf{r}_i, \{\mathbf{R}_{\mu'}\})$ is the total potential energy including the interaction among all GNR particles and between particles and substrate. The equation of motion for all the other atoms with coordinates $\mathbf{R}_\mu$ is

$$m_\mu\ddot{\mathbf{R}}_\mu = -m_\mu\gamma\dot{\mathbf{R}}_\mu - \nabla_{\mathbf{R}_\mu} V(\mathbf{r}_i, \{\mathbf{R}_{\mu'}\})\,. \tag{5.2}$$

5.3 Results and discussion

5.3.1 The frictional force traces

We extract the instantaneous simulated frictional force as the elastic force that the soft pulling spring exerts on the GNR

$$F_{\mathrm{k}}(t) = 3k_x\,[v_0 t - x_{end}(t)] \tag{5.3}$$

where $x_{end}(t) = \sum_{i=1}^{3} x_i(t)/3$ is the mean x-coordinate of the lifted end of the GNR, obtained by averaging the coordinates $x_i(t)$ of the three lifted-edge C atoms.

For each given lifting height z_0, the simulated AFM force trace is a plot of $F_{\mathrm{k}}(t)$ as a function of time, or equivalently of the displacement of the fixed-speed end of the spring $\Delta x(t) = |v_0|t$. For ease of comparison, we express this displacement in units of the lattice spacing of the gold substrate in the pulling direction, $a_{\mathrm{Au}} = 2.8838\,\text{Å}$.

Discarding initial transients, Figs. 5.3 and 5.4 show the steady-state simulated frictional forces

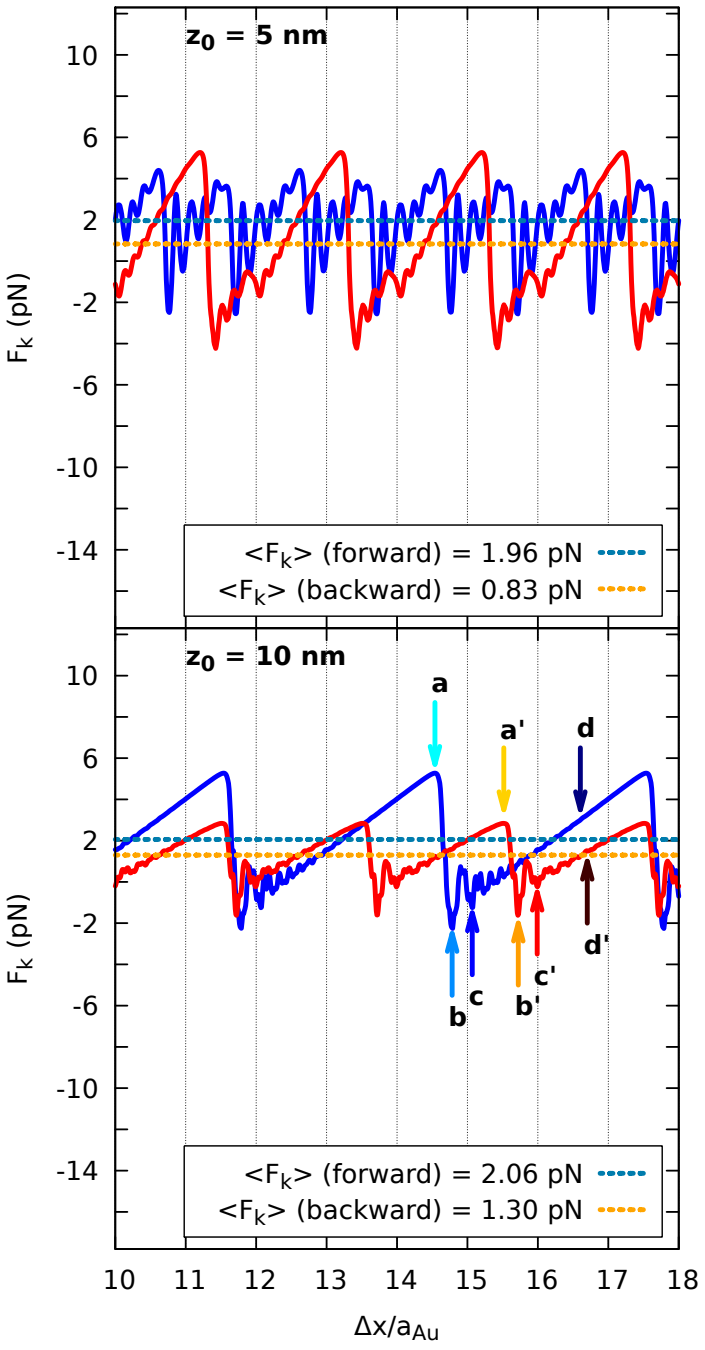

Figure 5.4: Frictional force for GNR sliding at relatively large lifting heights $z_0 = 5$ and 10 nm. The blue and red solid curves refer to the forward and backward sliding, respectively. Dotted curves report the corresponding average frictional values. Arrows identify some characteristic GNR configurations during the motion at $z_0 = 10$ nm: (a) the end of the stick phase, (b) the end of the slip phase, (c) the beginning of stick, (d) half-stick. Non-primed and primed letters are for forward and backward motion, respectively. The GNR geometries for the configurations marked by arrows are depicted in Fig. 5.5 below.

for lifting heights $z_0 = 1 - 3\,\text{nm}$, and $5 - 10\,\text{nm}$, respectively. For a direct comparison highlighting intrinsically different features between the forward (blue solid curves) and backward (red dashed curves) traces we show the backward forces reversed in sign and plotted as a function of positive (i.e. reversed) displacements. As a consequences, Figs. 5.3 and 5.4 do not display the typical dissipation frictional loop usually reported for standard AFM back-and-forth scans. At low lifting heights, $z_0 = 1 - 3\,\text{nm}$, Fig. 5.3, the computed force traces for the forward and backward scans exhibit a symmetric response, as observed in experiment [34]. Note that the experimental traces also contain a long-wavelength modulation (see Fig. 5.2) due to the Au-substrate reconstruction, here neglected. At the small lifting of $z_0 = 1\,\text{nm}$ the sliding force oscillation reflecting the atomic corrugation on Au(111) is smooth in both directions. As a result, the average frictional force ($0.1\,\text{pN}$) is close to zero, confirming the superlubric characteristic of the interface. We note that, due to the lattice mismatch between the GNR structure and the underneath substrate along the considered R30 direction, there exist two inequivalent good matching interface configurations, shifted almost by one half Au lattice spacing,: this condition gives rise to an approximate period doubling in the force traces.

5.3.2 Height-dependence of the sliding dynamics: from smooth sliding to stick-slip

The frictional evolution for increasing lifting height is remarkable. A first change in the dynamical response appears between 1 and 2 nm lifting. At $z_0 = 2\,\text{nm}$ the smooth sliding is replaced by atomic stick-slip with the same periodicity of the smooth oscillations at 1 nm. With the occurrence of this intermittent dynamics, usually marking in tribological systems the demise of superlubricity [1], we very reasonably find that friction rises by an order of magnitude. It can be noted that at the end of each slip the instantaneous force oscillates considerably, in both forward and backward traces, due to inertial overshooting. At higher lifting height $z_0 = 3$ a similar atomic stick slip is again observed, but without the delicate superimposed period duplication observed at smaller z_0.

A different scenario emerges for higher lifting, such as $z_0 = 5$ and 10 nm, Fig. 5.4. Forward and backward traces are not symmetric anymore, and multiple jumps [61] start to show up, contrasting the basically single stick-slip regime observed at small lifting. The slip distance depends quite generally on the lifting height, which controls the mechanical softness of the lifted part, and on the pulling direction. For instance, at $z_0 = 5\,\text{nm}$ the forward force trace is single slip, while that of the corresponding backward scan becomes double. Conversely, at $z_0 = 10\,\text{nm}$ the forward trace shows a stick-slip period of three lattice spacings, as opposed to two lattice spacings in the backward case.

Such asymmetric response, as we shall see, is determined by the interplay of two main effects. Firstly, forward and backward configurations imply different effective contact areas between the GNR and the substrate. Since the static friction oscillates widely with GNR contact length L_c [36], small differences in the effective contact length can lead in general to quite different static-friction thresholds. As a result, small differences in z_0 may lead to quite different dynamical friction patterns.

Secondly, as detailed in Sect. 5.3.3 below, the interplay between bending energy and adhesion differs strongly in the two pulling directions.

A first insight in the different forward and backward GNR dynamics can be obtained by exam-

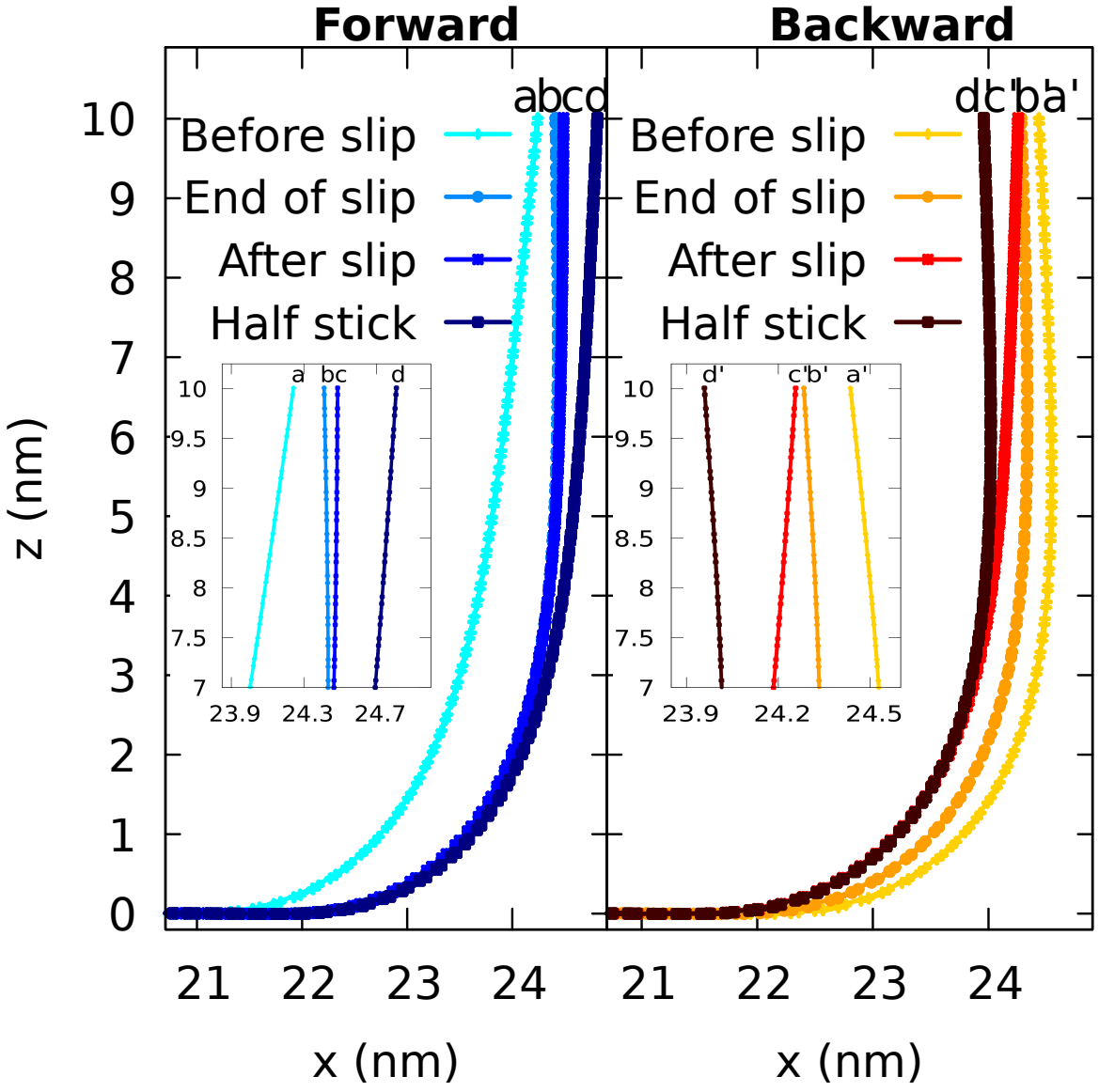

Figure 5.5: The GNR lateral profile at $z_0 = 10\,\text{nm}$ during the forward (left panel) and backward (right panel) motion for the four successive states marked by arrows in Fig. 5.4. The two insets help in highlighting the distinct GNR configurations near the lifted edge, during the stick-slip regime.

ining the characteristic shape of the GNR at specific instants during the stick-slip motion. Fig. 5.5 shows the lateral profile of the GNR in the forward and backward motion at $z_0 = 10\,\text{nm}$, at four distinct instants marked by arrows in Fig. 5.4. The main features of the stick-slip dynamics in the forward and backward motion are very similar. Once the spring reaches the critical elongation to overcome the Peierls-Nabarro barrier (a/a'), a slip event occurs: the physisorbed section sprints forward/backwards and reaches a new pinned position (b/b'). The GNR deformation occurring at slip leads to an *increase* (in the forward motion) / *decrease* (in the backward motion) of the GNR bending energy. This elastic energy is then progressively *released*/*absorbed* during the subsequent stick phase (c→d / c'→d').

5.3.3 Energy considerations

It is instructive to analyse how the individual energy contributions coming from the elastic bending of the GNR and from the adhesion to the substrate evolve during the stick-slip frictional dynamics. Consider for instance the motion of the GNR at large $z_0 = 10\,\mathrm{nm}$. The total GNR potential energy V is the sum of an intra-ribbon term, V_{REBO} from the C-C and C-H bonds, which controls the planar and bending stiffness, plus a second term, V_{LJ}, stemming from the C-Au and H-Au interactions which controls the adhesion of the unlifted part of the GNR. The time variation of V with respect to our reference configuration at $t = 0$, (a relaxed GNR with one lifted end), can be written as

$$\Delta V(t) = \Delta V_{\mathrm{REBO}}(t) + \Delta V_{\mathrm{LJ}}(t)\,. \tag{5.4}$$

For forward and backward motion, Fig. 5.6 compares the frictional force evolution (already displayed in Fig. 5.4) and that of the potential energy terms ΔV_{REBO}, ΔV_{LJ} and ΔV. Note the opposite contributions to the total GNR energy for forward and backward sliding. In the forward scan, the intra-ribbon contribution ΔV_{REBO} is negative, with an energy gain due to the decrease of GNR curvature in the detached part, as discussed in Sect. 5.3 above. At the same time, the system loses adhesive energy, not just because the external force works to overcome the static friction energy barrier which blocks the sliding, but mainly because the physisorbed section shortens in length as the GNR end is pulled forward (see also the zoomed-in GNR z-profile in Fig. 5.7), causing an increase of ΔV_{LJ}. Exactly the opposite occurs for backward sliding, where ΔV_{REBO} is positive, owing to the curvature increase of the detached part, whereas ΔV_{LJ} is negative reflecting a corresponding improvement of adhesion due to an increased contact length L_c (see again Fig. 5.7). For completeness, we note that, at even larger z_0 values, the backward-driven GNR may initiate to peel off the Au surface during the stick phase, thus starting decreasing the ΔV_{LJ} adhesive contribution.

There is a clear correspondence between the general energy evolution described above and the lifted nanoribbon geometry. Fig. 5.7 compares the shape profile $z = z(x)$ of the GNR near the detachment point, just before the slip either forward or backward. By comparison with the relaxed, static shape (zero force), the curvature and the physisorbed section of the GNR are respectively smaller in the forward case, and larger in the backward case.

5.3.4 Role of the ribbon short edge and uncompensated moiré pattern

As was observed in our previous study of the fully adhering – non-lifted – GNRs [36], the 2D "bulk" of the GNR/Au(111) interface is incommensurate and structurally lubric ("superlubric"). Like in other superlubric systems, the static friction – the minimal force required to set the interface into sliding motion – does not grow (on average) as much as the contact area. Specifically, for a non-lifted GNR, the static friction oscillates around a fairly constant mean value as a function of the nanoribbon length [36]. This indicates that the edges, here the short ones, are mostly responsible for pinning, as we have shown in chapter 4. The strong oscillation of the static friction F_{s} around the constant average trend as a function of the GNR length is related to the "uncompensated" moiré pattern near the GNR ends, i.e. the residual of L_c divided by the moiré-pattern wavelength. This friction oscillation may involve variations in F_{s} comparable with the average [163]. This appears to be the case also with lifted GNRs, where the effective contact length L_{eff}, defined below, varies

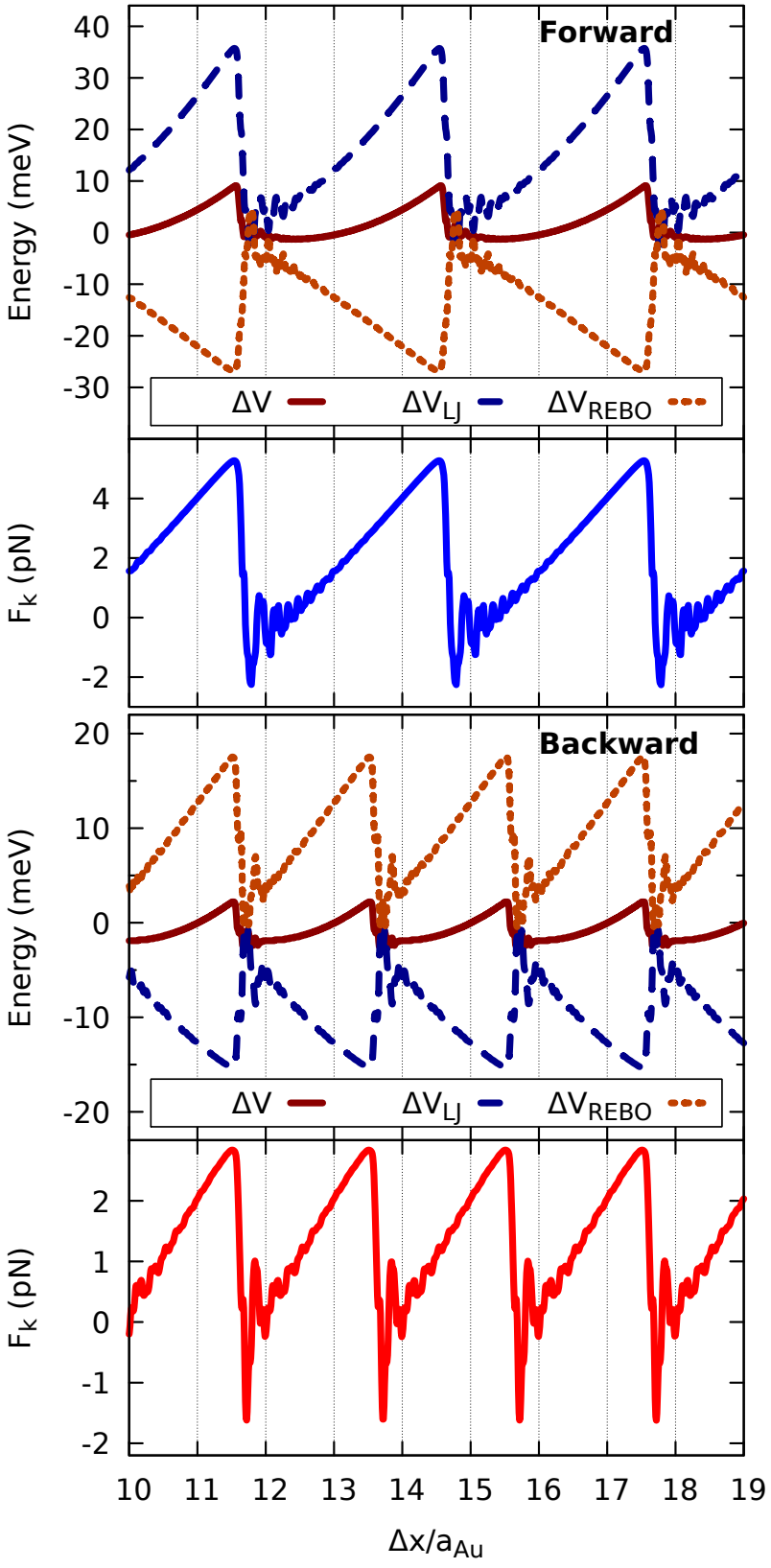

Figure 5.6: Comparison between the frictional force and the variation of the elastic intra-ribbon V_{REBO} and adhesive ribbon-substrate V_{LJ} contributions to the GNR total energy in the stick-slip motion at $z_0 = 10\,\mathrm{nm}$.

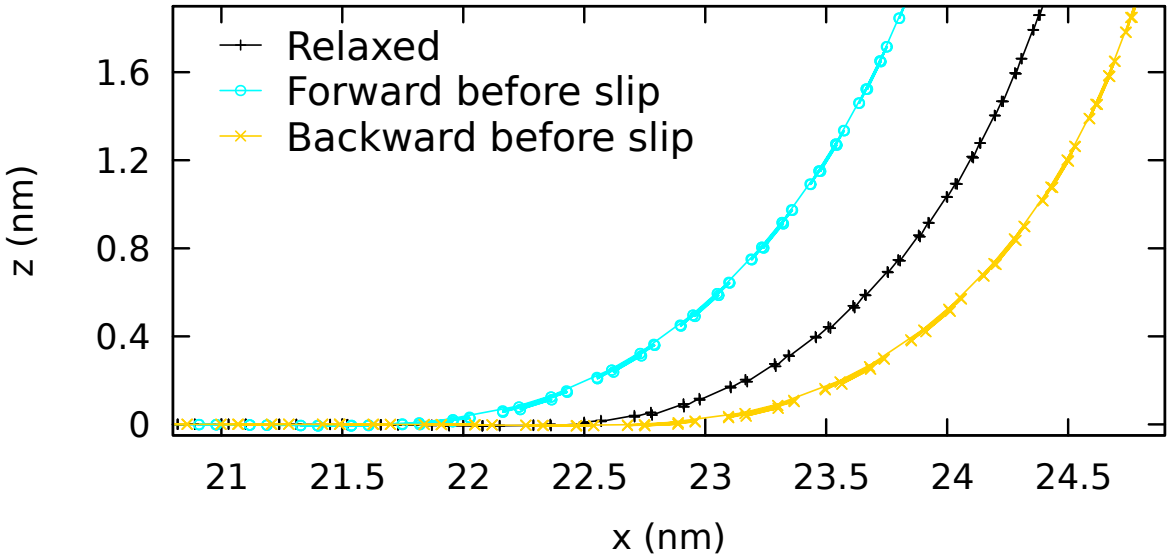

Figure 5.7: GNR lateral profile closed to the detachment region in the forward (cyan line) and backward motion (yellow line) just before the slip. The configuration of the relaxed GNR at rest (black line) is included as reference.

as a function of z_0 and changes dynamically in time.

By lifting the GNR at successively increasing heights, the effective contact length L_{eff} will change, giving rise to minima/maxima of the static friction force. We define the effective contact length L_{eff} of a lifted GNR by dividing V_{LJ} by the same quantity per unit length of an infinite-length simulated GNR with periodic boundary conditions, V_{LJ}^{∞}:

$$L_{\text{eff}}(z_0, t) = \frac{V_{\text{LJ}}(z_0, t)}{V_{\text{LJ}}^{\infty}}\,, \tag{5.5}$$

where $V_{\text{LJ}}(z_0, t)$ is the total interaction energy between the GNR and the substrate at the lifting height z_0 and at time t. It turns out that for lifting heights between $z_0 = 7.5\,\text{nm}$ and $z_0 = 12.5\,\text{nm}$ we cover one complete period of the static friction [36]. Fig. 5.8 shows the force traces corresponding to lifting heights $z_0 = 7.5$, 9.9, and 12.5 nm, the first and the last ones corresponding to expected local maxima of the oscillating static friction versus effective size, the second to a local minimum, along with the corresponding change in time of the effective contact length $L_{\text{eff}}(z_0, t)$ of eq. (5.5). As expected, the peaks in F_{k} and the mean friction forces are larger at lifting heights that correspond to the expected local maxima of static friction, namely $z_0 = 7.5\,\text{nm}$ and $z_0 = 12.5\,\text{nm}$, than at the expected local minimum, namely $z_0 = 9.9\,\text{nm}$.

For a grid of lifting heights z_0, Fig. 5.9 reports the maximum force $F_{\text{k}}^{\max}$ obtained from the peaks just before slip once a steady stick-slip regime is established versus the effective contact length L_{eff} for that height. The best fitting sinusoids of the form

$$F_{\text{k}}^{\max}(L) = \alpha + \beta \sin\left(\frac{2\pi L}{\lambda_m} - \delta\right), \tag{5.6}$$

for both the forward and backward motion, are also drawn as reference. α, β, λ_m, δ are fitting parameters. The values and the $\lambda_m = 4.86\,\text{nm}$ period oscillation of the lifting-dependent maximum

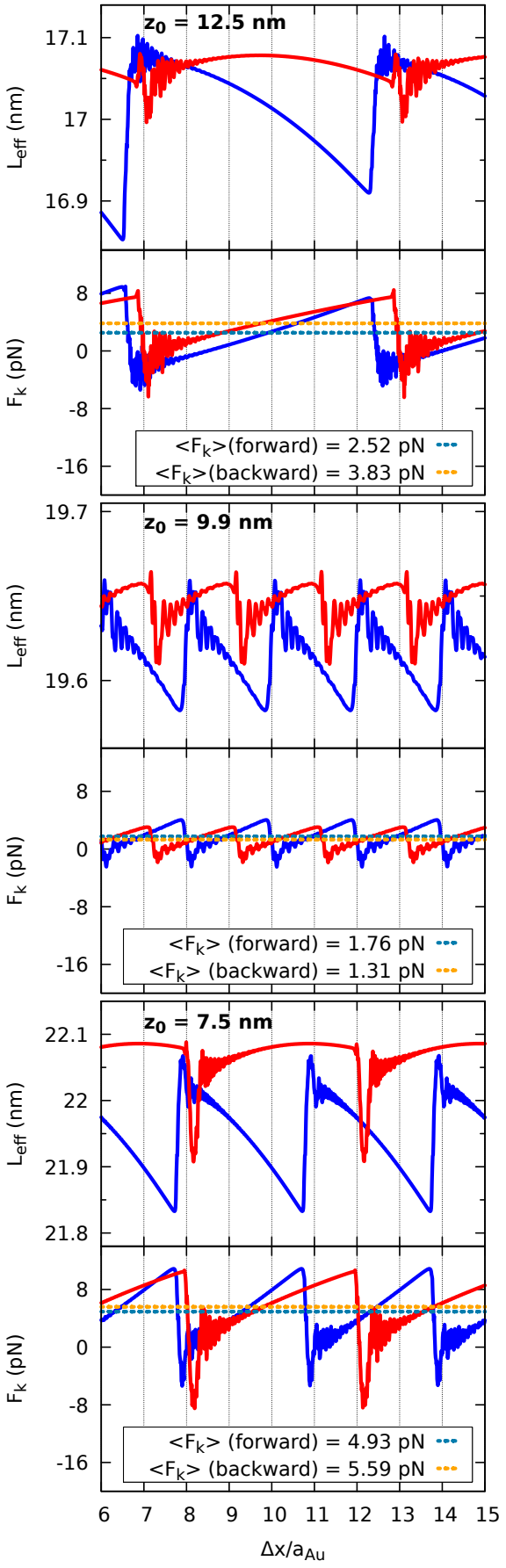

Figure 5.8: Comparison between the friction-force traces for three large lifting heights, $z_0 = 7.5$, 9.9 and 12.5 nm, and the change of the effective instantaneous contact length L_{eff} between the GNR and the substrate. As previously, blue and red solid curves refer to forward and backward sliding, respectively, and dotted curves report the corresponding average values.

force compares reasonably well with the established static friction trend as a function of the non-lifted GNR length [36]. Somewhat larger in magnitude, both forward and backward maximum forces share the same oscillation as the static friction of the non-lifted GNR with length equal to the effective lifted GNR length L_{eff}. This result further confirms that the uncompensated, edge-related, part of the moiré pattern determines the magnitude of the maximum kinetic-friction force before slip.

Fig. 5.9 compares the maximum kinetic friction $F_{\text{k}}^{\text{max}}$ with the static friction F_{s} obtained for fully adhering GNRs [36]. For a given system in the underdamped regime, the two quantities should match in the limit of vanishing driving velocity v_0. At finite velocity it is generally expected that $F_{\text{s}} > F_{\text{k}}^{\text{max}}$, with static friction always exceeding dynamic one. Here, naively, we observe the opposite. This might look counterintuitive, as one might expect a larger friction for fully adhering GNRs. However, as pointed out above, static friction is dominated by the two GNR short-ends in this superlubric system. The two short-edges are equivalent in the unlifted case, and are responsible for the frictional oscillations as a function of L_c [36]. By contrast, in the case of lifted GNR the bending at the leading edge produces a termination which is strongly inequivalent to that of the trailing edge. As a result, cancellation of the lateral forces acting on the two ends is more problematic, yielding generally an overall larger friction.

It is also worth asking if GNRs might show any tendency to peel off the substrate when driven backward at large lifting heights. As seen in Figs. 5.6 and 5.7, the backward stick-slip motion is accompanied by an *increase* of adhesion in the stick state, while a *decrease* of adhesion is seen in the forward motion. In Fig. 5.8, $z_0 = 9.9\,\text{nm}$, this fact is confirmed by the increase of L_{eff} in the stick state of the backward motion. In these cases no tendency to peel off is registered. In contrast, at a lifting height of 12.5 nm, we notice that in the backward motion the adhesive length increases up to a maximum and then decreases again with a sort of parabolic trend. This indicates that the spring initially pushes the physisorbed atoms adjacent to the bent GNR section down in closer contact with substrate, promoting an increased adhesion. Once the extension of the driving spring is sufficiently large, the GNR starts to detach from the substrate, causing a loss of adhesion. This analysis shows that, depending on the lifting height z_0 and the precise value of the static friction barrier at that height, the GNR can indeed start to peel off from the substrate. In all simulated cases, as backward pulling continued, a slip event would release the bending stress before the peeling instability would fully develop and lead the GNR to a complete peel off. As a general rule, peeling is more pronounced for those combinations of z_0 and GNR length leading to those L_{eff} producing the largest possible static friction threshold, and generally for larger lifting height, because of the softer GNR elasticity and greater mechanical advantage.

5.4 The effect of the LJ amplitudes and the vertical spring stiffness

As pointed out in Sec. 4.2.2, the outcome of an MD simulation and the related frictional response observed for a specific simulated interface closely depends on the specific values of the parameters of the simulation setup. This introduces a degree of an arbitrariness in the simulation, which we can remove by showing that a change of those parameters does not consistently modify the dynamics over a broad range of values.

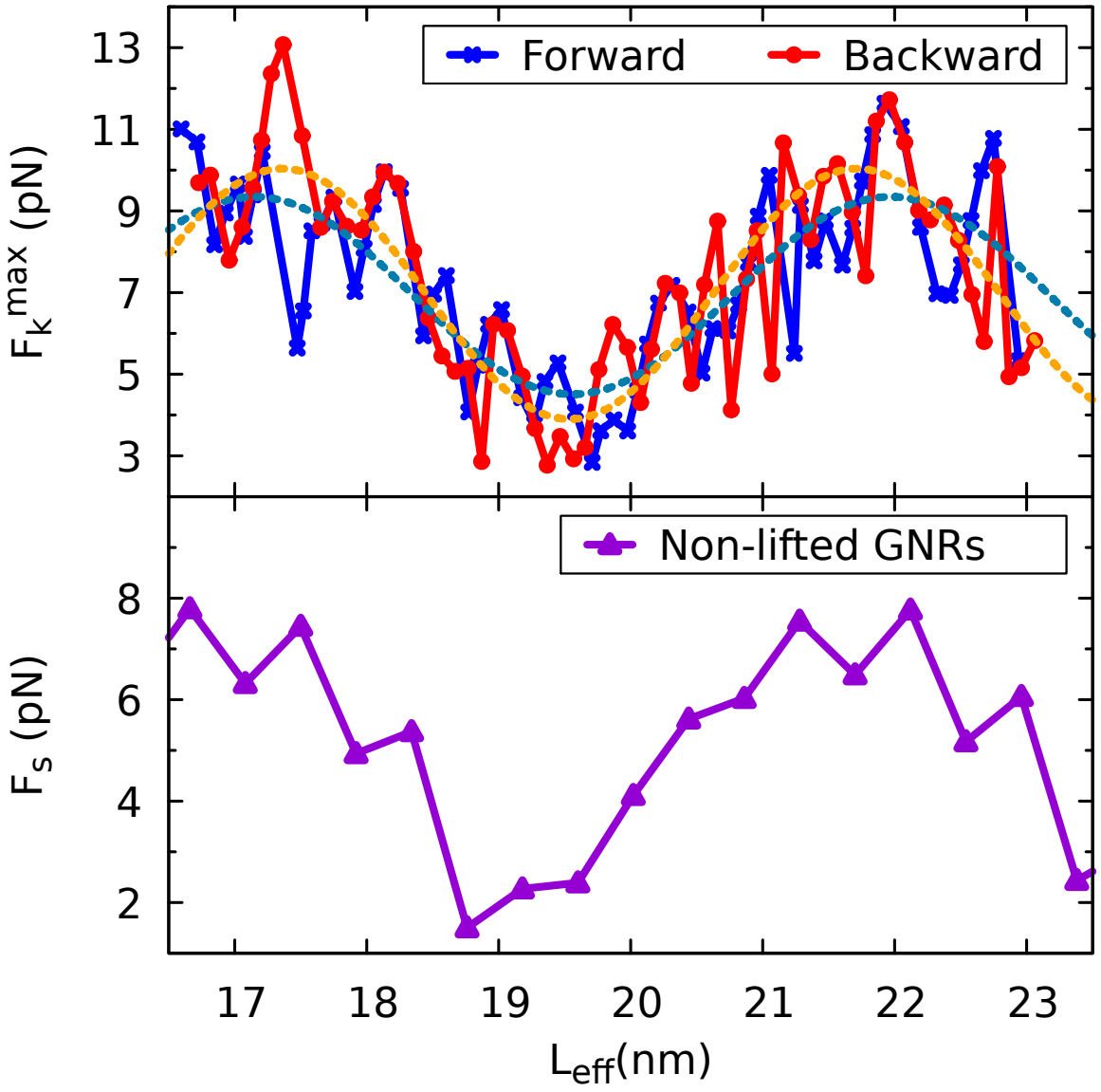

Figure 5.9: Comparison between the static friction force of non-lifted GNRs [36] (lower panel), and the maximum kinetic force (upper panel), as a function of the effective contact length L_{eff}, varied by repeating the simulations for many lifting heights z_0. The dotted cyan and orange lines are the corresponding best fitting curves of Eq. (5.6) to the $F_{\text{k}}^{\text{max}}$ data.

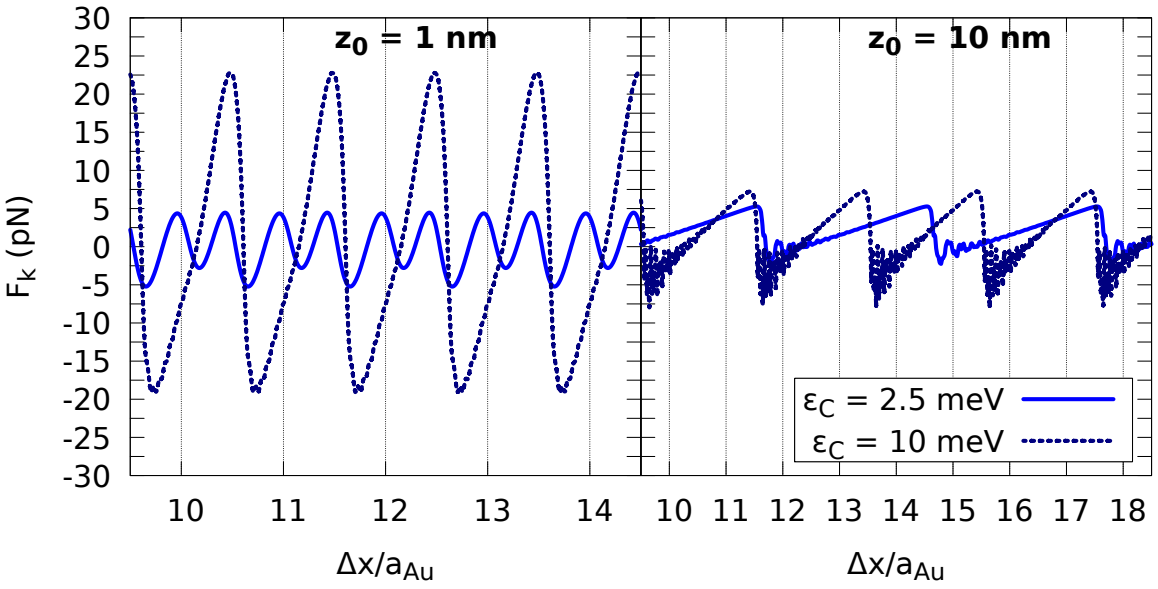

Figure 5.10: Comparison between the GNR sliding dynamics for two different values of the C-Au interaction amplitudes $\epsilon_C = 2.5\,\text{meV}$ and $\epsilon_C = 10\,\text{meV}$ (the H-Au interaction amplitude is scaled proportionally) for $z_0 = 1.0\,\text{nm}$ and $z_0 = 10\,\text{nm}$ in the forward motion.

In the case of the lateral sliding dynamics of the GNRs on gold, we investigate the role of the stiffness of the vertical spring k_z that is used to constrain the height of the lifted edge of the GNR and the value of the LJ amplitudes ε_C and ε_H.

Fig. 5.10 shows a comparison between the GNR lateral force dynamics for two different values of the C-Au interaction amplitude $\varepsilon_C = 2.5\,\text{meV}$ and $\epsilon_C = 10\,\text{meV}$ (the H-Au interaction amplitude is scaled proportionally) for $z_0 = 1.0\,\text{nm}$ and $z_0 = 10\,\text{nm}$ in the forward motion.

The qualitative system behavior, particularly the emergence of a clear stick-slip dynamics with a z_0-dependent periodicity, is not significantly affected by scaling up the interaction amplitudes by a factor 4. Quantitatively, the observed transitions from smooth sliding to single and multiple stick-slip regimes may occur at slightly different lifting values of the GNR edge due to the different balance between the corrugation of the interface (which increases for larger values of ε_C) and the z_0-depedent bending elasticity of the GNR. The competition of these two energy contributions results in a different critical value of z_0 for which the stick-slip instability can take place.

Fig. 5.11 shows a comparison between the GNR lateral sliding dynamics obtained for both the forward (left panels) and backward (right panels) motion for two different values of the vertical spring stiffness ($k_z^{\text{hard}} = 1.6 \cdot 10^5\,\text{N/m}$ and $k_z^{\text{soft}} = 1.8\,\text{N/m}$). Quite surprisingly, using a spring k_z that is 5 orders of magnitude softer has no substantial effect on the quantitative outcome of the simulation and only results in tiny vertical deformations (of the order of some pms) of the softer spring, as marked by the oscillation amplitude shown by the spring elongation $\Delta l(t) - \Delta l(0)$ in the upper panels of Fig. 5.11.

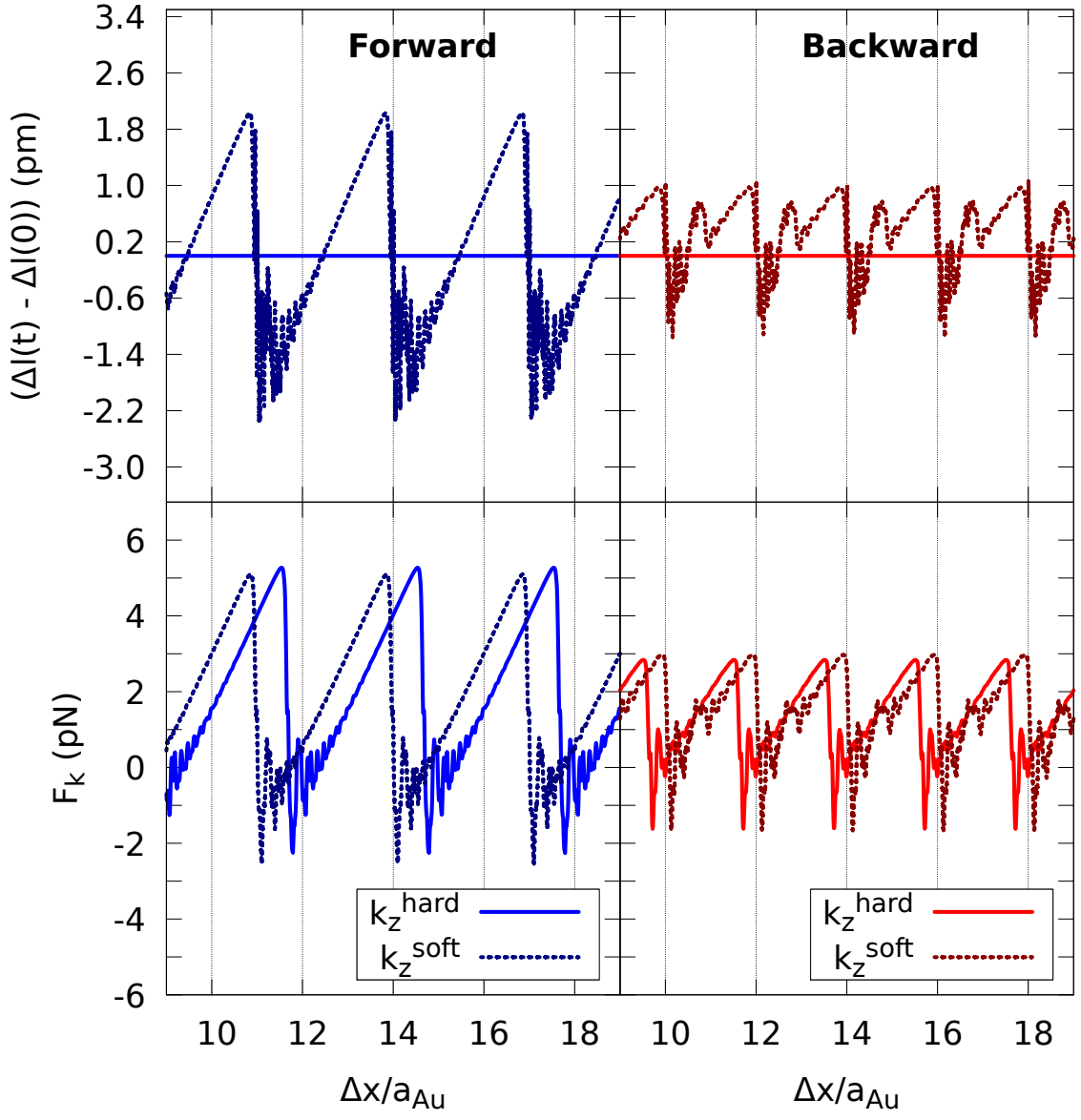

Figure 5.11: Comparison between the GNR sliding dynamics for $z_0 = 10\,\text{nm}$ with two different vertical springs ($k_z^{\text{hard}} = 1.6 \cdot 10^5\,\text{N/m}$ and $k_z^{\text{soft}} = 1.8\,\text{N/m}$). The lower panels show the force traces in the forward (left) and backward (right) motion, while the upper panels show the time variation of the vertical spring elongation with respect to the equilibrium configuration of the lifted GNR.

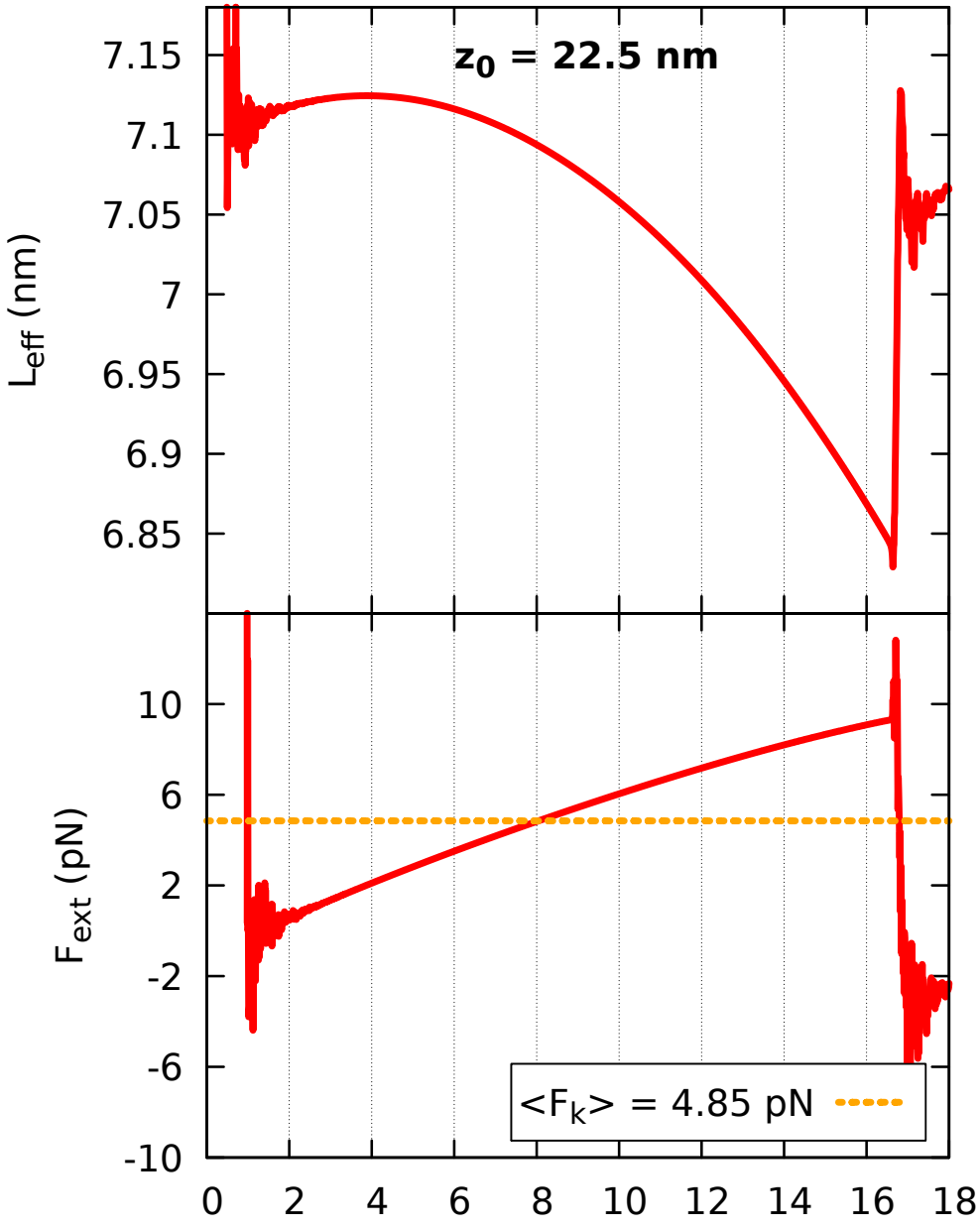

Figure 5.12: Time-evolution of the kinetic friction force $F_{\rm k}$ (lower panel) and the effective GNR-substrate contact length $L_{\rm eff}$ (upper panel), as defined in Eq. (5.5), for high lifting ($z_0 = 22.5\,$nm).

5.5 Peeling of the GNR at large heights

In Fig. 5.8 we have observed that the GNR can show a slight peel-off effect from the substrate in the backward motion. Indeed, as the value of z_0 is increased, the augmented softness of the GNR enables larger elastic deformations in the stick phase, which can even produce a decrease of the effective contact length with the substrate, calculated via Eq. (5.5).

We have further investigated this point by performing a simulation of backward sliding of the GNR at a large lifting height $z_0 = 22.5\,\text{nm}$ corresponding to a GNR adhered length smaller than one third of the total GNR length. The peel-off dynamics of the GNR from the substrate is signaled in Fig. 5.12 by the large decrease of L_{eff} in the stick phase, followed after the instability by a large slip with a total length of even 16 lattice spacings of the gold substrate.

This evident peeling of the GNR at these large heights and the connection with existing experimental data regarding the lift-off dynamics of single physisorbed molecular chains [35] inspires our latest work on the detachment mechanisms of the GNRs on gold (see chapter 6).

5.6 Conclusions

Mimicking the experimental setup of Kawai *et al.* [34] we reproduce and interpret the observed frictional regimes of the GNR as a function of the lifting height z_0. For increasing z_0, we predict a remarkable transition from smooth sliding to atomic stick-slip, characterized initially by single slips, and then by multiple slips at larger heights. Specifically, the periodicity of the stick-slip dynamics is dominated by the bending elasticity of the GNR, which enables larger slip distances at larger heights. The augmented softness, introduced by bending of the GNR as z_0 increases, plays opposite roles for the two driving directions, decreasing (forward) and increasing (backward) the GNR/substrate adhesion. The lifting-dependent amplitude of the instantaneous friction force is not a "bulk" feature, and is entirely determined by the short edges of the GNR – in the lifted case as well as in the non-lifted case.

We find an oscillation of friction with lifting height. That in turn is related, via identification of an effective GNR contact length of the physisorbed GNR section, to the moiré-pattern lack of compensation close to the edges, qualitatively similar but quantitatively different to that occurring in the static friction of unlifted GNRs [36]. Past experiments on lifted GNR sliding [34] have not yet explored the new regime which we describe here, essentially due to the relatively small length of the GNR used there (6.28 nm only), whereby the GNR lifted at 5 nm was almost completely detached from the Au-substrate, very nearly peeled off. Our much longer – 30 nm – simulated GNR, only approaches peeling at lifting heights larger than $\sim 10\,\text{nm}$, as shown by the time evolution of the effective contact length. Present predictions about the sliding should be borne out by future experiments, hopefully on longer GNRs, as well as on more general physisorbed flakes of graphene and other 2D materials. In these systems, we predict that it should be possible to observe a transition from smooth sliding to stick-slip for increasing lifting height, an asymmetric forward/backward friction, and a peel-off instability.

Chapter 6

Detachment dynamics of GNRs on gold

Metal-surface physisorbed graphene nanoribbons (GNRs) constitute mobile nanocontacts whose interest is simultaneously mechanical, electronic, and tribological. Previous work showed that GNRs adsorbed on Au(111) generally slide smoothly and superlubrically owing to incommensurability of their structures. We address here the nanomechanics of detachment, such as realized when one end is picked up and lifted by an AFM cantilever. AFM nanomanipulations and molecular-dynamics (MD) simulations identify two successive regimes, characterized by (i) a progressively increasing local bending, accompanied by the smooth sliding of the adhered part, followed by (ii) a stick-slip dynamics involving sudden bending relaxation associated to intermittent jumps of the remaining adhered GNR segment and tail end. AFM measurements of the vertical force exhibit oscillations which, compared with MD simulations, can be associated to the successive detachment of individual GNR unit cells of length 0.42 nm. Extra modulations within one single period are caused by step-like advancements of the still-physisorbed part of the GNR. The sliding of the incommensurate moiré pattern that accompanies the GNR lifting generally yields an additional long-period oscillation: while almost undetectable when the GNR is aligned in the standard "R30" orientation on Au(111), we predict that such feature should become prominent in the alternative rotated "R0" orientation on the same surface, or on a different surface, such as perhaps Ag(111). This chapter is part of the paper *Detachment dynamics of graphene nanoribbons*, in press in the journal ACSNano.

6.1 Introduction

Understanding the adhesive and frictional properties of nanosystems, such as molecules, 3D nanoclusters or 2D adsorbates, polymeric chains, etc., on structurally well-characterized crystalline substrates [34, 35, 36, 37, 75, 104, 134, 166, 170, 171, 172, 173, 174, 175, 176, 177, 178] is of key importance for both fundamental sciences, as e.g. contact mechanics and nanotribology, and technological applications. Indeed, controlled nanomanipulation of deposited nano-objects, in terms of positioning, adhesion, depinning and sliding, can be used to build new molecular superstructures,

to explore the influence of the environment on individual molecules, or to perform engineering operations at the ultimate, molecular, limit of fabrication for novel hi-tech nanodevices.

Mostly due to the extremely large surface-to-volume ratio, the peculiar behavior of these nanosystems may present properties that vary dramatically with size. Atomically precise synthesis techniques [168, 179], experimentally tuning their physical and chemical characteristics during the preparation procedure, may assemble structurally similar geometries, with quite distinctive features influencing the system in terms of adhesive and friction-related response.

With their strong resilient structure and the experimental possibility to be picked up at one edge, dragged laterally and/or lifted up vertically by atomic force microscopy (AFM) techniques, graphene nanoribbons (GNRs) physisorbed on Au(111) surfaces do represent an important actor in this exploration.

AFM-driven sliding displacements have been already exploited to probe the frictional properties of this interface at very-low temperature [34], providing initial evidence for a weak length dependence of the static friction of armchair nanoribbons. Paralleling those experimental results, subsequent numerical simulations [36] have confirmed a frictionally superlubric regime characterized by small friction, strongly oscillating and basically periodic with no average increase upon increasing the GNR length. With a static friction trend dictated by the characteristic periodicity of the graphene-gold interface moiré pattern, the simulated dissipative behavior already highlighted the occurrence of different dynamical regimes, ranging from smooth sliding to multiple stick-slip friction depending on the vertical height of the lifted, and laterally pulled, end [37].

In the present work, by means of non-equilibrium atomistic MD simulations and AFM manipulation data, we investigate the detailed mechanisms of detachment of a 30-nm-long armchair GNR from the Au(111) surface upon vertical lifting of one end. Depending on the actual configuration at the nanoribbon/gold interface, the combined theoretical and experimental analysis sheds light, at a molecular level, on the manner in which adhesion and lateral corrugation of the nanocontact determine the characteristic periodicities observed in the lifting force and its z-derivative during the progressive detachment process upon lifting.

6.2 Detachment dynamics at R30

6.2.1 Detachment in the experiment

Seven carbon atoms wide ($n = 7$) armchair GNRs are synthetized on a clean Au(111) surface at 4.8 K in UHV, as detailed in Appendix A. We control the Au-covered AFM tip so that it picks up a $\sim$ 25 nm-long GNR at one end, producing unilateral detachment as sketched in Fig. 6.1a. Fig. 6.1b shows a STM topography of the surface before performing the manipulation of that GNR aligned along the $[-1, 0, 1]$ direction of the gold substrate, also called R30. This is, within the herringbone reconstruction of Au(111), the spontaneous orientation adopted by the GNR. In the specific case, the GNR adsorbs on a single fcc terrace, between two subsequent fcc-hcp discommensurations. The tip is positioned at one GNR end, with a low bias voltage ($\sim$ 2 mV). When the junction between the tip and the GNR is established, an abrupt change in the tunneling current is detected. Subsequently, a dynamical AFM mode is turned on, with a vertical oscillation amplitude $\simeq$ 43 pm. The tip is then slowly retracted while recording the frequency shift (Fig. 6.1d)

as well as the energy dissipation (see Fig. 6.5). Fig. 6.1c shows the STM topography taken after the full detachment of that GNR, followed by tip cleaning outside the scan area. Fig. 6.1d shows the measured frequency shift, i.e. the variation of the resonance frequency of the AFM force sensor upon vertical lifting of the GNR, as a function of the height z. This frequency shift is proportional to the derivative of the vertical force that the tip exerts on the GNR: dF_{ext}/dz. [35] This force gradient measurement with a stiff cantilever realizes a high sensitivity measurement while avoiding a typical mechanical instability, which can be caused in the quasi-static force measurement with a soft cantilever [180, 181]. After an initial steep increase of the frequency shift, due to the GNR curvature build-up, an oscillating signal is observed, with a main periodicity $\simeq 0.40\,\text{nm}$.

6.2.2 Simulation details and physical observables

. In order to shed light on the physical mechanisms that come into play in the detachment dynamics, we simulate this same system with non-equilibrium molecular dynamics (NEMD). We construct a $n = 7$ armchair GNR, consisting of a stripe of alternating triplets and pairs of carbon hexagons, of width $\simeq 0.7\,\text{nm}$ and length $\simeq 30.2\,\text{nm}$, where all the peripheral C-atoms are passivated with hydrogens [36, 37]. All carbon atom coordinates are fully mobile. The Au(111) substrate consists of two unreconstructed layers, also fully mobile, on top of one rigid layer, with fcc stacking. The lifting effect of the AFM tip on the first row of three C-atoms is simulated by means of a vertical spring with an effective elastic constant $k_z = 1800\,\text{N/m}$. One end of this spring moves vertically with constant velocity $v_0 = 0.5\,\text{m/s}$ along the z-axis of Fig. 6.1a. Although much larger than the experimental speed, $\simeq 1\,\mu\text{m/s}$, we verified that the simulated lifting speed is still small enough to yield meaningful, speed-independent results. The spring is attached to the three C atoms in the first row. The in-plane coordinates (x, y) of these three atoms are kept fixed during detachment, so that the lifting is vertical. The simulation proceeds until complete detachment of the GNR is achieved. To gain insight into the physics of this system, we are interested in comparing the time-evolution (or equivalently the evolution against the z-coordinate of the driving spring end) of the following quantities:

- the instantaneous vertical force acting along the pulling direction, namely

$$F^z_{\text{ext}}(t) = 3k_z\,[v_0 t - z_{\text{end}}(t)] \tag{6.1}$$

  where $z_{\text{end}}(t) = \sum_{i=1}^{3} z_i(t)/3$ is the average z-coordinate of the lifted end of the GNR;
- the vertical force gradient dF_{ext}/dz, directly comparable to measurements, where it is proportional to the frequency shift $\delta f(z)$:

$$dF_{\text{ext}}/dz = \kappa\,\delta f(z) \tag{6.2}$$

  where $\kappa = 0.15\,\text{N m}^{-1}\text{Hz}^{-1}$ is a conversion factor [34];
- the deviations of the GNR-substrate total adhesive energy $\Delta E_{\text{adh}}(t)$ and the gold-gold total potential energy $\Delta E_{\text{Au-Au}}(t)$ away from their linear behaviour

$$E(t) = E^0 - Pt \tag{6.3}$$

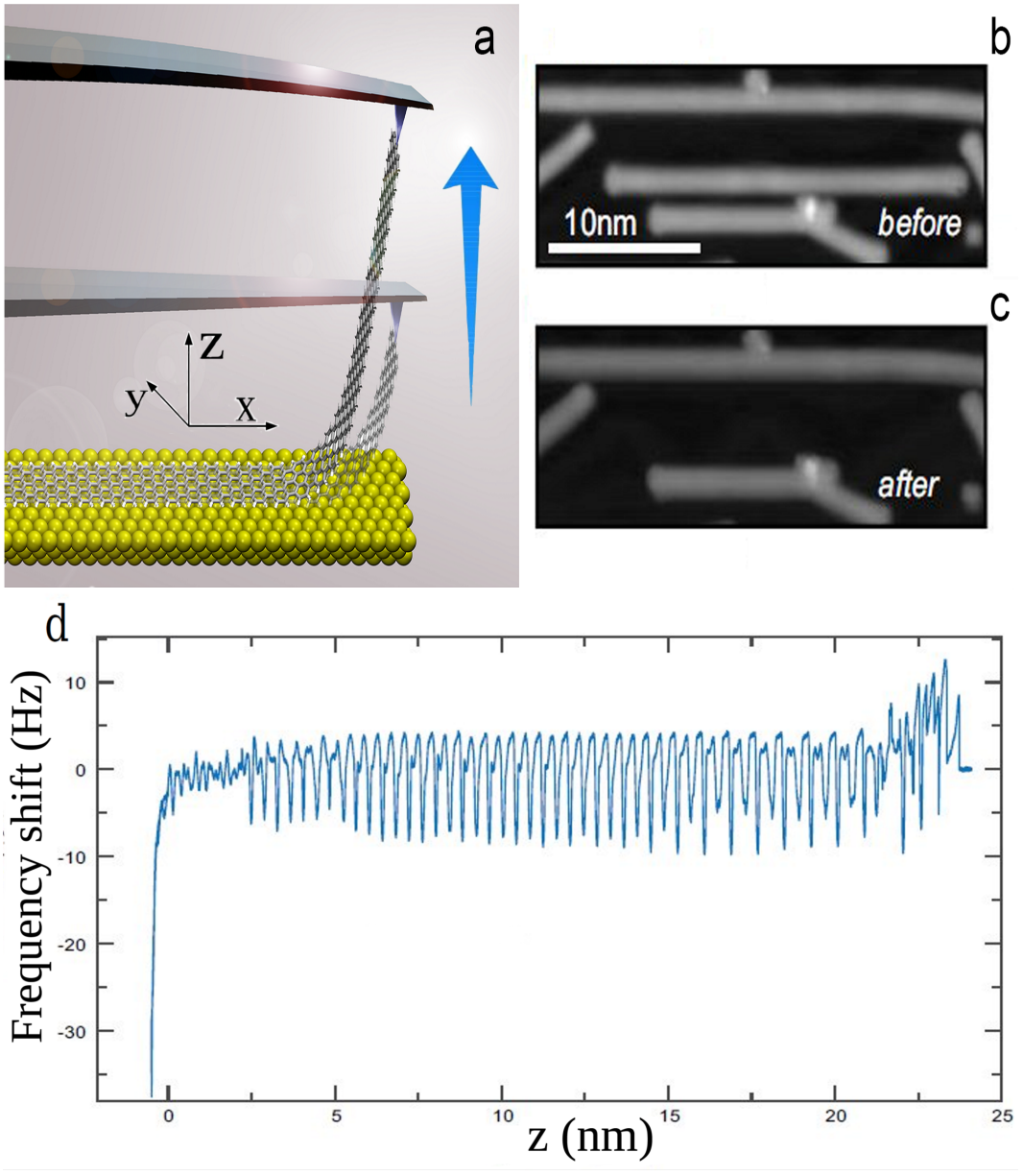

Figure 6.1: Panel a: a sketch of the tip-GNR setup in two distinct configurations of the GNR during detachment. Panel b, c: two STM scans taken before and after detachment. Panel d: the experimental frequency-shift trace recorded as the GNR is lifted up until detachment.

where P and E^0 are fitting parameters [1];

- the total variation of the intra-GNR carbon-carbon and carbon-hydrogen potential energy $\Delta E_{\mathrm{GNR}}(t) = E_{\mathrm{GNR}}(t) - E_{\mathrm{GNR}}(0)$. The value at $t = 0$ corresponds to an unlifted relaxed GNR on gold;
- the horizontal advancement of the trailing end of the GNR along the x-axis

$$\Delta x_{\mathrm{tail}}(t) = x_{\mathrm{tail}}(t) - x_{\mathrm{tail}}(0) \tag{6.4}$$

The quantity $x_{\mathrm{tail}}(t) = \sum_{j=1}^{3} x_j(t)/3$ is obtained by averaging the instantaneous x-coordinate of the end row of C-atoms, the last ones to get lifted up at complete peel-off.

These physical observables are conveniently reported as functions of the dimensionless vertical displacement z/a_{GNR}, where $a_{\mathrm{GNR}} = 0.42\,\mathrm{nm}$ equals one GNR unit cell length, and the reference coordinate $z = 0$ is taken at the average vertical position of the C atoms of the fully relaxed GNR on the substrate in the unlifted configuration.

6.2.3 Detachment of GNRs with MD

The detachment dynamics of the GNR occurs following two successive regimes. In the first regime at low lifting for $z < 3\,\mathrm{nm}$, the vertical motion of the AFM initially builds up the GNR detachment and curvature, marked by an increase of the GNR bending energy, due besides the C-Au detachment, to the lifted GNR curvature against its bending rigidity. The bending energy rise is consistent with the initial upswing of the experimental frequency shift of Fig. 6.1d. The GNR-Au(111) corrugation energy is small compared to the system bending elasticity, so that the first relevant, yet gradual, build-up of the GNR curvature results in a smooth sliding of the still attached GNR tail. For $z \simeq 3\,\mathrm{nm} \simeq 7\,a_{\mathrm{GNR}}$, the frequency-shift profile reaches a plateau with a superimposed oscillation. This second regime corresponds to a steady peeling. Fig. 6.2 shows that in this second regime both the experimental and the theoretical force derivative curves. The simulated force derivative is smaller in magnitude and not identical in lineshape to the experimental one. In that respect, one must recall that the force fluctuations represent only a small deviation relative to the total lifting force, a very large background quantity which is unaccessible experimentally but dominating in simulation.

The level of quantitative agreement between theory and experiment is limited by the use of simple two-body Lennard-Jones potentials to describe simultaneously adhesive interactions and the interface corrugation. The specific values of the LJ parameters adopted in the present work represent the best possible compromise to reproduce at the same time the correct order of magnitude of the adhesive forces for carbon/metal interactions and the crucial features of the lifting dynamics associated to lateral corrugation.

First, the main periodicity is equal to the GNR unit length a_{GNR}, consistent with the observation that the vertical motion of the spring induces a sequence of discrete detachments of GNR sections with the size of one GNR unit cell, until complete pull-off. Secondly, within one single period of this vertical lifting the detachment force experiences significant and roughly periodic drops, that

[1] Since the external spring drives the GNR away from the substrate at an average constant velocity, we expect the GNR-substrate potential energy to increase linearly in time on average. Also, the detachment of the GNR causes the substrate layers to relax around the detachment region, causing the Au-Au potential energy to decrease linearly with time until after complete detachment the Au surface reaches its fully relaxed ground-state energy.

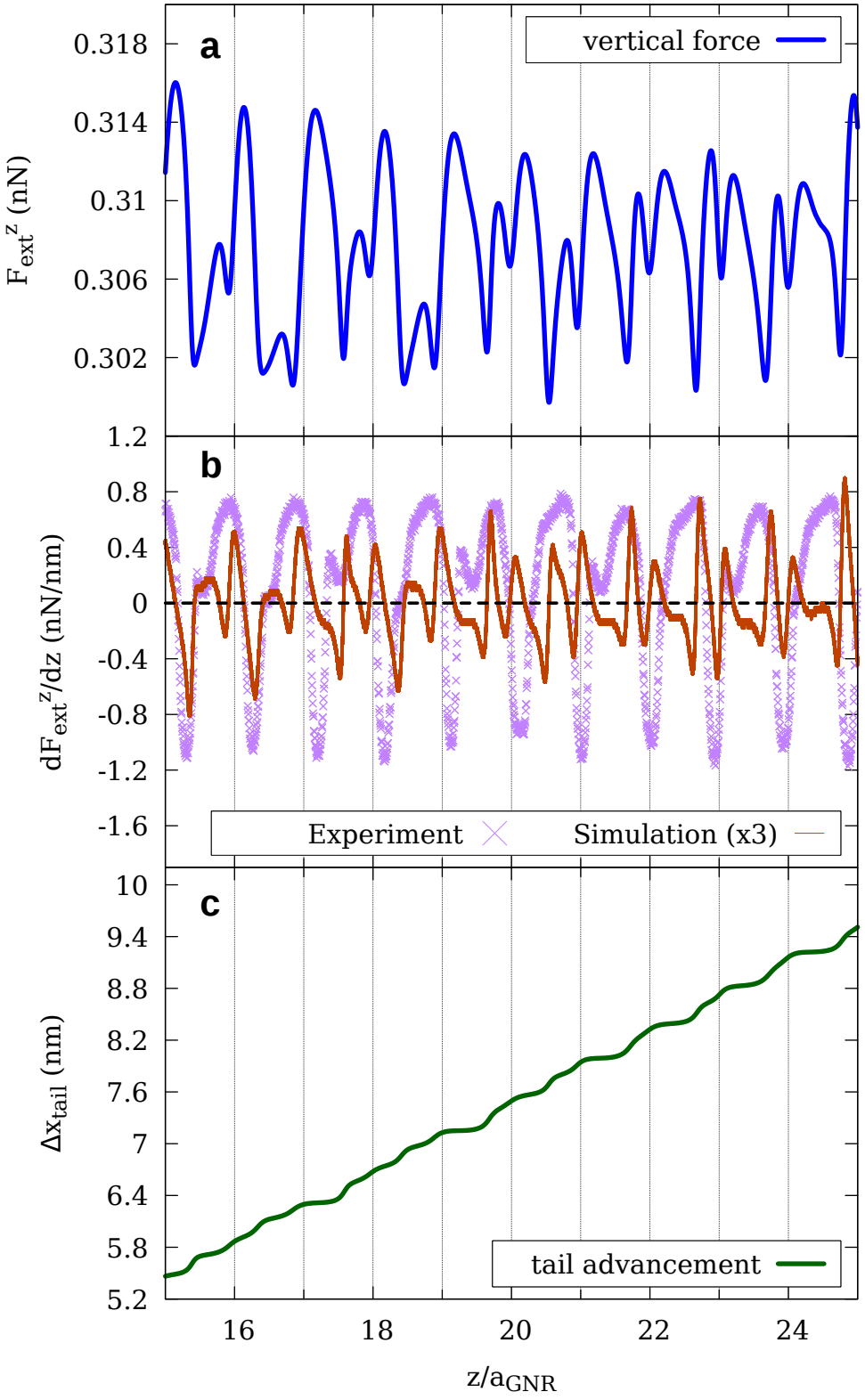

Figure 6.2: Detachment dynamics of the R30-oriented GNR/Au(111) in the height range $15\,a_{\mathrm{GNR}} < z < 25\,a_{\mathrm{GNR}}$. The simulated lifting speed is $v_0 = 0.5\,\mathrm{m/s}$, the experimental speed is much smaller. Comparison of (a) the simulated external lifting force, (b) the experimental and the simulated force gradient magnified by three times, and (c) the tail end x-advancement. The spacing of the vertical grid equals $a_{\mathrm{GNR}} = 0.42\,\mathrm{nm}$ corresponding to one unit cell length of the GNR (one triplet plus one doublet of carbon hexagons).

occur in coincidence with step-like slips of the still-physisorbed section of the GNR, as illustrated by small steps advancement of the tail in Fig. 6.2c. We verified that the force drops are enhanced by the gold mobility by repeating the entire detachment simulation with a substrate consisting of gold atoms frozen in their crystalline arrangement. The importance of the gold mobility, an element not discussed before, is also confirmed by the behavior of the fluctuations of the gold-gold potential energy of Fig. 6.3b: they are small, but not entirely negligible compared to the variations of the other energy terms of the system.

Focusing on just four a_{GNR} lifting periods for heights $15\,a_{\mathrm{GNR}} < z < 19\,a_{\mathrm{GNR}}$, Fig. 6.3 provides further insight into the detachment. This zoomed-in detail shows that the main periodicity of $F^z_{\mathrm{ext}}(t)$ corresponds to the detachment of a full GNR unit cell. As in experiment, that main period is additionally decorated by superimposed oscillating features. These finer force derivative features do not arise, as one might have initially suspected, from the progressive detachment of the $n = 7$ armchair GNR sub-structures (e.g. the alternating rows of 2 and 3 carbon hexagons). Instead, these secondary force derivative features actually arise from the slips, during the detachment dynamics, of the nanoribbon tail, against the lateral corrugation of the gold substrate. The intrinsic incommensurability between $a_{\mathrm{GNR}} = 0.42\,\mathrm{nm}$ and $a_{\mathrm{Au}} = 0.288\,\mathrm{nm}$ would in principle permit a frictionless, superlubric sliding. However, the trailing end interrupts the GNR-Au(111) moiré pattern, giving rise to an uncompensated region which breaks superlubricity causing a frictional barrier against sliding, capable of causing an unexpected stick-slip. That, together with the role played by the GNR bending elasticity makes the recorded profile of the lifting force quite complex and rich. More information about this interplay of different length scales can be inferred from the behavior of the individual potential energy terms controlling the system dynamics. First, we observe that the adhesive energy and bending energy variations for increasing z are anti-correlated. Indeed, during the sticking intervals where the physisorbed tail section remains approximately but not exactly immobile (quasi-horizontal steps of Fig. 6.3c), ΔE_{adh} increases, corresponding to a decreasing adhesive energy due to the creeping detachment of one GNR unit cell. In the same time intervals, there is a gain in ΔE_{GNR}, mainly due to a decrease in the bending cost of the GNR curvature. Once the detachment of one unit cell is complete, the lifted part of the GNR reaches a larger inclination, thus producing an increased lateral x-directed force component, driving the physisorbed section of the GNR forward. This force component is generally strong enough to exceed the tenuous lateral Peierls-Nabarro barrier [70] against sliding of the physisorbed section, thus inducing its advancement, signaled by a slip of the tail, and correspondingly by a drop in $F^z_{\mathrm{ext}}(t)$. This dynamics upon strictly vertical lifting is similar to that observed for the case of laterally-sliding lifted GNRs [37]. Since $a_{\mathrm{GNR}} \simeq 1.46\,a_{\mathrm{Au}}$, during each main a_{GNR} period corresponding to detachment of one GNR unit, the simulation exhibits a rather irregular sequence of one or two horizontal-slip events, with the corresponding force drops.

6.2.4 The emergence of hysteresis

Fig. 6.4 shows a frictional loop corresponding to a cycle of detachment/re-attachment: the GNR is first lifted up to a nearly detached configuration ($z_{\mathrm{max}} = 28\,\mathrm{nm}$), then the spring advancement is stopped and the whole system is relaxed in the lifted configuration. Finally the spring motion is reversed until complete re-attachment is achieved. The dynamics in both directions is characterized by similar sequences of attachments/detachments, accompanied by an increase/decrease of the

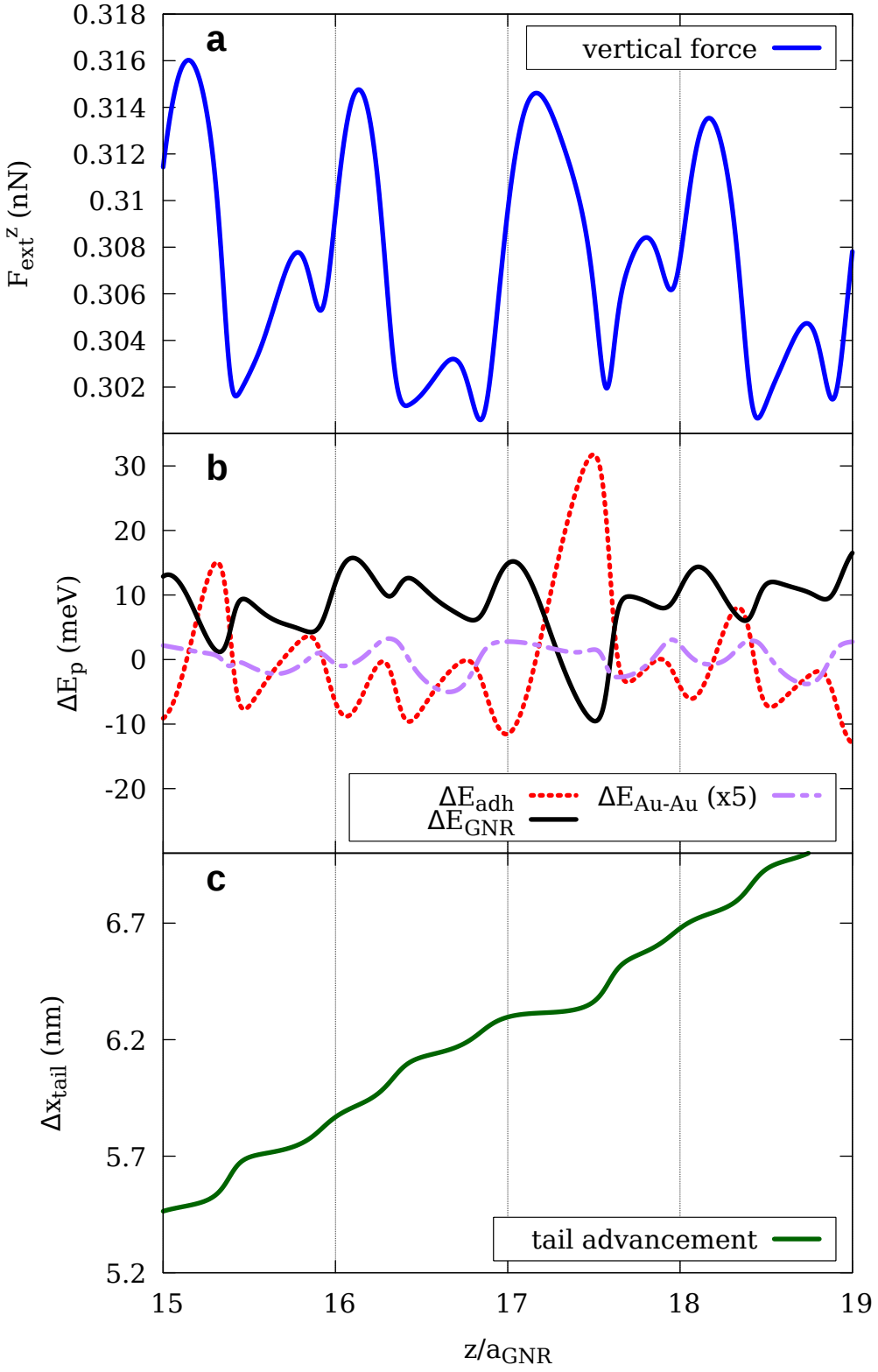

Figure 6.3: Detail of four periods in the simulated detachment dynamics, in the steady-state regime. Comparison of: (a) the vertical force; (b) the individual potential energy terms: the adhesive energy fluctuations ΔE_{adh} (red dotted line), the total variations of the C-C intra-GNR potential energy ΔE_{GNR} (black solid line), and the Au-Au potential energy $\Delta E_{\mathrm{Au\text{-}Au}}$ (purple dashed line); (c) the x-advancement of the physisorbed GNR body tail. An offset $\Delta = -600\,\mathrm{meV}$ has been applied to the ΔE_{GNR} curve for better comparison with the other terms.

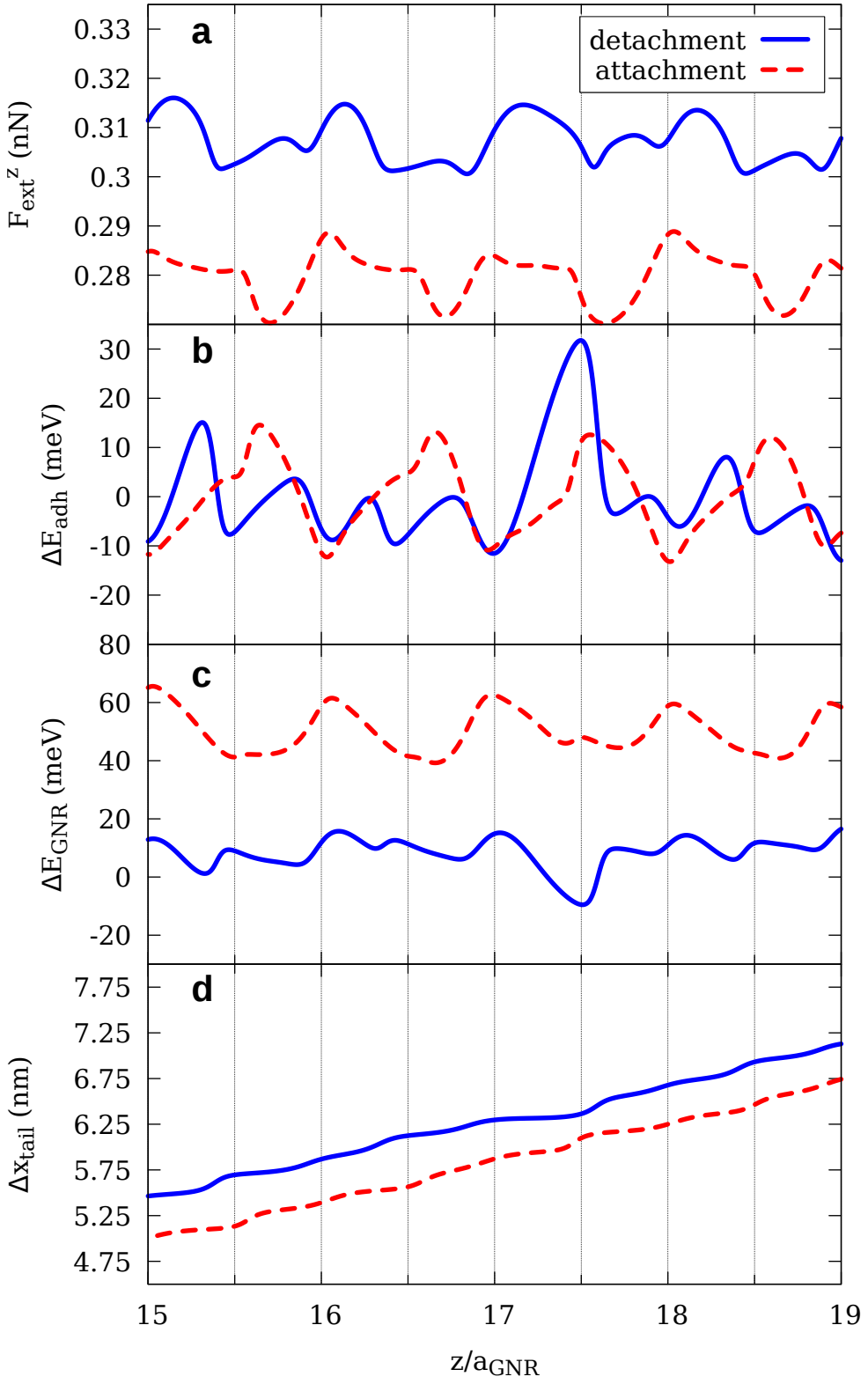

Figure 6.4: Comparison between the detachment (blue solid lines) and the re-attachment (red dashed lines) dynamics of the GNR in four selected periods. (a) The pulling force, larger in detachment than in re-attachment. The area between the two curves represents the total work done by the moving spring along one detachment-reattachment cycle. (b, c) The main potential energy contributions ΔE_{adh} and ΔE_{GNR} respectively. An offset $\Delta = -600\,\mathrm{meV}$ is applied to the ΔE_{GNR} as in Fig. 6.3. (d) The tail x-advancement.

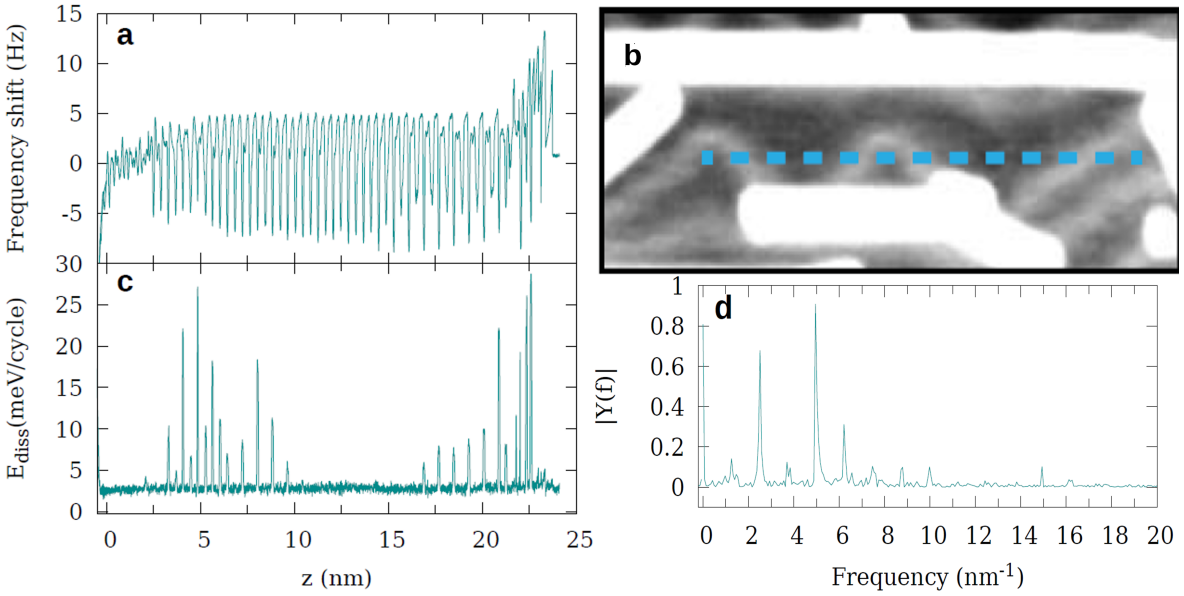

Figure 6.5: Comparison between the experimental frequency shift trace (panel a) and the measured energy dissipation per cycle (panel c), where one cycle corresponds to one complete oscillation of the AFM at the given height. Peaks of dissipation are present when detachment of the single unit cells of the GNR occur, as stated in the main paper and confirmed by simulations (see Figure 4). The emergence of the two extended dissipative regions roughly in the intervals $3\,\text{nm} < z < 10\,\text{nm}$ and $z > 17\,\text{nm}$ arises because the specific GNR manipulated in the experiment crosses the herringbone reconstruction of the gold (111) substrate, as shown in the STM image of panel b, in two equally extended areas. During edge-lifting, as soon as the GNR tail slides across the fcc/hcp boundary regions, the dissipative signal increases due to stronger adsorbate/substrate interaction, still exhibiting the evenly spaced characteristic peaks of the GNR unit cell detachment. The blue dashed line in panel b identifies the GNR position before the vertical lifting nanomanipulation. Panel d highlights the behavior of the single-sided Fourier spectrum of the experimental frequency shift of panel a.

GNR curvature, and followed by one or two slips of the GNR tail. Unsurprisingly, the vertical force is systematically larger in the detachment curve than in re-attachment. If the adhesive GNR/substrate potential energy barrier had been the only one to be overcome by the moving spring and if the ribbon motion had been perfectly adiabatic, one might have expected no hysteresis, with the total energy spent for the detachment completely recovered during the re-attachment, because the adhesive forces are conservative. In actual fact, in our simulations we observe a significant hysteresis, with two different effects: first of all the *average* vertical force in detachment is larger, and secondly there are force peaks (in detachment) and force drops (in re-attachment) due to the sudden detachment/attachment of individual units of the GNR and consequent bending relaxations and tail slips along the upward and downward tracks. These events correspond to intrinsic mechanical instabilities of the system, that would hence be obtained even in the limit $v_0 \to 0$. The difference between the average forces, responsible for the total work of the external force along the up-down cycle is due to the dissipation in the $T = 0$ Langevin thermostat, which is the only term that makes the overall dynamics non conservative. The dynamical AFM mode that we adopt for our measurements, explores steadily a small portion of the histeretic cycle of Fig. 6.4, but at a far smaller speed $\simeq 1\,\mu$m/s than in simulations. As a result, experiment is far closer to the adiabatic regime, and finds significant dissipation practically only in correspondence to the detachments/re-attachments of the GNR unit sections. The resulting experimental energy

dissipation curve is reported in Fig. 6.5.

As a final observation, Fig. 6.4c shows that the GNR internal energy ΔE_{GNR} is systematically larger during re-attachment than during detachment. This is due to an extra forced bending produced by the spring pushing the GNR down toward the substrate during the re-attachment rather than pulling it up as during detachment.

6.3 Moiré pattern signatures - detachment at R0

In the previous section we clarified the main features of the GNR dynamics, determined by the successive detachment of the GNR individual unit sections. By contrast, as pointed out in our previous works [36, 37], the dependence of the static friction on the size of the GNRs and the sliding dynamics upon lateral pulling was strongly affected by other GNR characteristics, such as the moiré-pattern primary periodicity, which gives rise to regions of local registry match/mismatch between the GNR and the substrate.

Surprisingly, no sign of this kind of feature has been observed so far either in the liftoff experiment or in the simulations. We are therefore interested in understanding by MD simulations whether this feature could naturally emerge by changing the relative strength between the adhesion of the GNR, which governs the detachment of the GNR unit cells, and the corrugation, which contrasts lateral motions and tunes the moiré pattern force contribution [36].

In our model, one can for example reduce the characteristic distance σ used in the Lennard-Jones (LJ) potential to describe the GNR/substrate interaction (see Appendix A). Fig. 6.6 shows the vertical force profile obtained by reducing this distance from the standard $\sigma = 0.342\,\mathrm{nm}$ of all previous calculations to $\sigma = 0.274\,\mathrm{nm}$. This yields a stronger lateral corrugation, which enhances the contrast between matching and mismatched regions of the moiré pattern [36]. Superimposed to the usual a_{GNR} periodicity of the GNR unit cells detachment, the lifting force now exhibits a second long-wavelength modulation, which can be fitted by a simple sinusoidal function of the form

$$F(z) = F_0 + F_1 \cos\left(\frac{2\pi}{\lambda_m} z + \varphi\right) , \tag{6.5}$$

F_0 being the average vertical force, F_1 the amplitude of the force oscillation, λ_m its wavelength, and φ its phase. The resulting $\lambda_m = 4.86\,\mathrm{nm}$ corresponds to the moiré pattern wavelength in the R30 alignment [36]. This is consistent with the subsequent detachment of regions with better adsorption energy, with good local registry between the GNR and the substrate, and regions of poorer adsorption energy with mismatched registry. Since by artificially enhancing the substrate corrugation the moiré pattern periodicity becomes evident in the force profile, a similar enhancement could in principle occur by choosing in principle a different GNR orientation on the substrate. On Au(111) all GNR orientations different from R30 are disfavored by the herringbone reconstruction of Au(111), as mentioned above. Au(111) could in principle be replaced by a different substrate, such as perhaps Ag(111) or Cu(111) or others, that are not reconstructed, theoretically permitting different orientations and/or different adhesion energies and different moiré pattern periodicities.

For a qualitative impression of the kind of changes expected, we simulate the detachment of a GNR deposited along the $[1\bar{1}0]$, or R0, alignment, of our hypothetically unreconstructed Au(111). Both adhesion and corrugation are larger in that GNR alignment, compared to the real R30

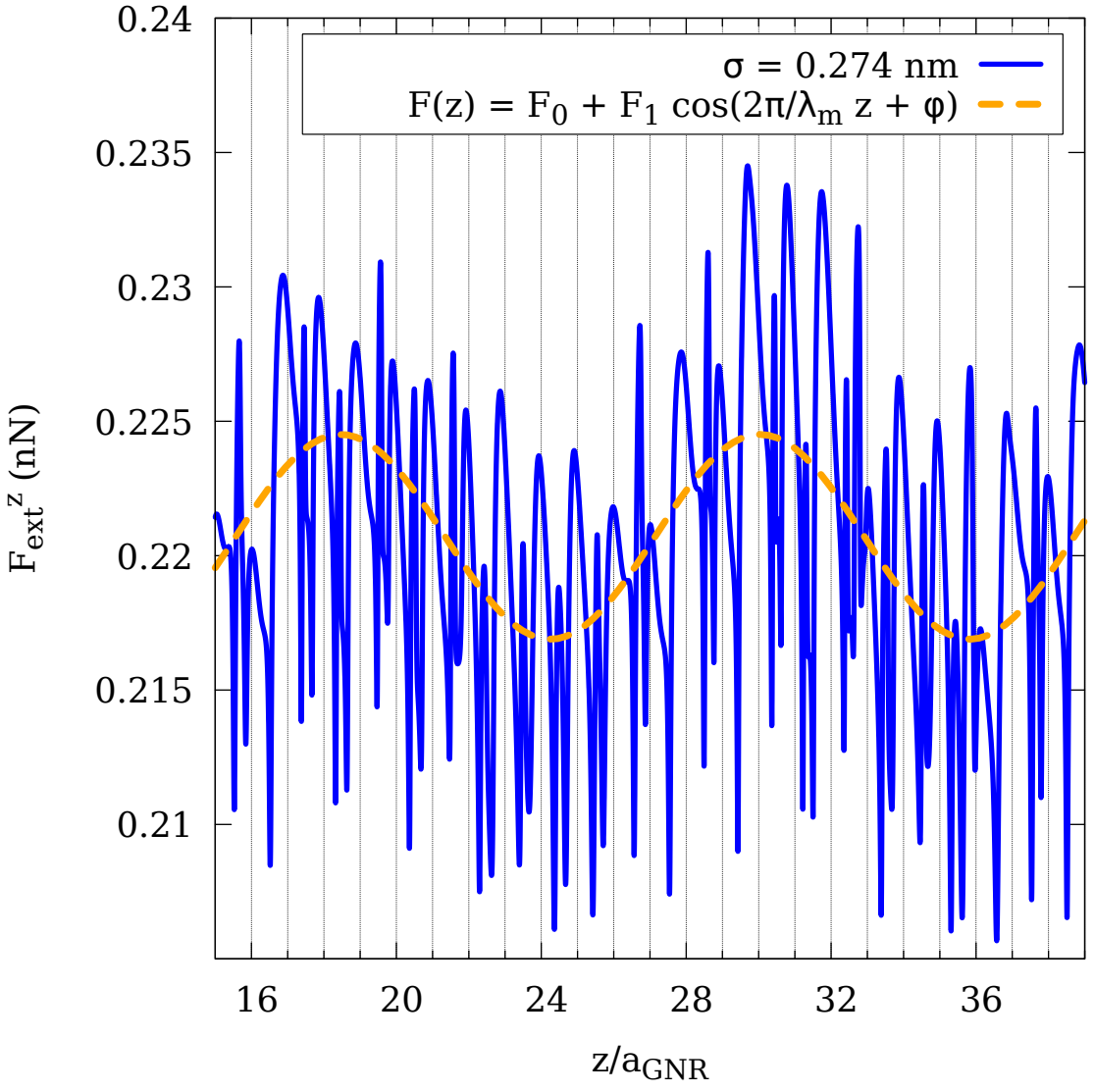

Figure 6.6: Vertical force profile obtained by artificially modifying the LJ distance σ from the regular value $\sigma = 0.342\,\text{nm}$ to a smaller one $0.274\,\text{nm}$ (blue solid curve). The fitting function of Eq.(6.5) (yellow dashed curve) emphasizes the long-wavelength periodicity, now visible due to the detachment of moiré pattern units, at this artificially larger interaction strength.

alignment addressed above and earlier [36].

Fig. 6.7 shows the detachment traces from simulations of GNR/Au(111) for the R0 orientation. In this alignment, the substrate periodicity $a_{\mathrm{Au}} = 0.499\,\mathrm{nm}$ generates a moiré pattern with primary periodicity $\lambda_m^{\mathrm{R0}} = 1.32\,\mathrm{nm}$ due to its zig-zag shape [36]. With the main periodicity now determined by the moiré pattern, the signature of the detachment of the single unit cells of the GNR almost disappears. For this reason we express the quantities of interest as a function of $z/\lambda_m^{\mathrm{R0}}$. In R0 alignment, the dynamics consists of successive detachment of entire moiré pattern units, as indicated by peaks in the adhesive fluctuations, followed by multiple slips-like advancements of the physisorbed tail, that are accompanied by wide oscillations of the vertical force. Finding no way yet to realize the GNR R0 alignment in experiment, otherwise observed in other graphene/metal interfaces [150], the status of the results summarized in Fig. 6.7 is that of an interesting theoretical prediction, deserving future experimental investigation.

6.4 Discussion and Conclusions

We have described extensive non-equilibrium molecular dynamics (NEMD) simulations of detachment dynamics by vertical lifting of a graphene nanoribbon adsorbed on Au(111), along with experimental data of the tip-applied force derivative. Results show that the steady state of this vertical dynamics is characterized by the detachments of the individual physisorbed units of the GNR, with the GNR unit cell 0.42 nm periodicity, in both the experimental tip frequency shift and the simulated vertical-force profiles. These detachments are accompanied by an intermittent stick-slip-like, stop-and-go motion of the tail, which is responsible for extra vertical-force drops that are visible within the main periods.

A qualitatively similar phenomenology is observed during re-attachment, where a sequence of unit cell attachments and tail slips still takes place. The frictional loop corresponding to one detachment/re-attachment cycle also shows that a nonadiabatic partial detachment/re-attachment of the GNR is a non-negligible source of energy dissipation. A non-negligible contribution to the detachment force evolution and to the dissipation comes from the deformability of the Au substrate. Theory overall parallels closely the experimental data, despite quantitative discrepancies due to the impossibility to reproduce in simulations the very low speed as well as the finest adsorbtion details of the experimental system. Importantly, we have shown that the detachment dynamics can be affected by different competing periodicities depending on the relative strength between the total adhesion and the corrugation of the interface. Enlarging our view, we have explored the simulated detachment for the R0 alignment. Here the larger corrugation leads to an almost complete disappearance of the GNR unit-cell detachments in favor of moiré-pattern features, the detachment now involving moiré-pattern periods as entire units. Like the R30 case, the detachment of one complete unit is then followed by sudden multiple slips of the tail.

Further investigations of these observations could involve a theoretical and experimental investigation of this type of nanomanipulation either by changing the GNRs orientation on a possibly unreconstructed gold substrate, or possibly by considering different substrates without reconstructions and/or larger corrugations, such as possibly silver, copper, or others.

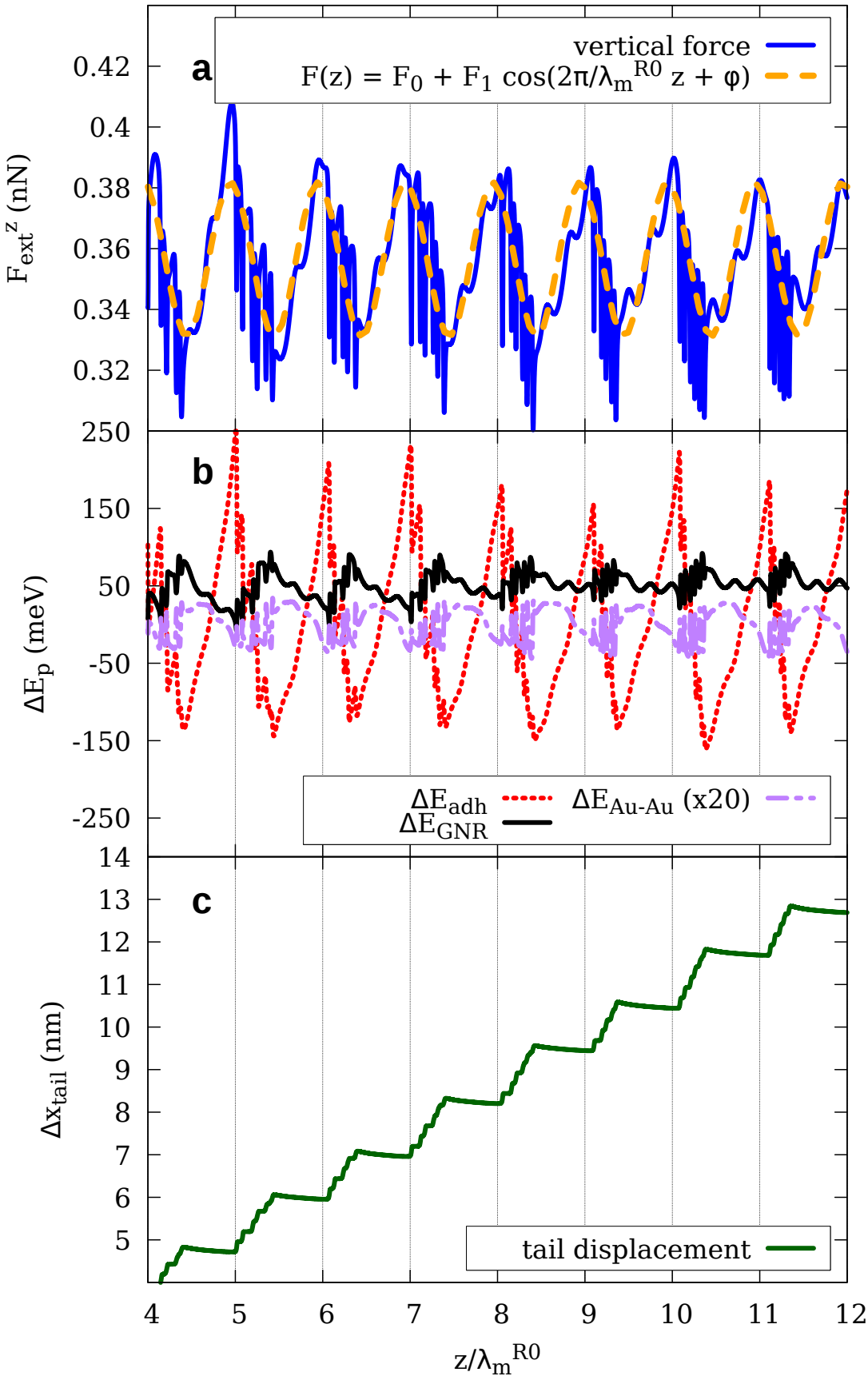

Figure 6.7: GNR/Au(111) detachment dynamics for the R0 alignment. The fit of the vertical pull-off force with the function of Eq.(6.5) (yellow dashed curve) highlights the moiré pattern periodicity.

Chapter 7

Conclusions and perspectives

In this Thesis, the study of the frictional features of a specific nanoscale interface, characterized by graphene nanoribbons (GNRs) on gold, is presented.

In chapters 1 and 2 we presented an overview of the field of nanofriction, with a strong focus on the theoretical modeling and the experimental techniques that are currently used to study the friction of nanoscale interfaces and relate it to the complex molecular mechanisms that are at play within these systems.

The results that we have presented in chapters 4, 5 and 6 concern both the static properties of the GNRs and their dynamics under the action of external drivings, used to mimick the nanomanipulations that are realized experimentally to produce lateral sliding (see chapter 5) and vertical detachment (see chapter 6) of the GNRs.

Our study indicates that the GNR/gold interface is structurally lubric, with a resulting very low friction (in the range of some pNs) and with a basically zero average increase upon increasing the GNR length. In addition, the oscillating behavior of the static friction force as a function of the GNR length is explained in terms of moiré pattern features, highlighting the importance of the geometric interlocking between the slider and the substrate in determining the frictional response.

In chapter 5 we have shown that this system is also suitable to obtain a dynamical transition between a smooth sliding state and violent stick-slip regimes, by lifting one short edge of the GNR at increasing heights. This result showed the intrinsic relation between friction and the out-of-plane softness of the GNR, a feature which is also confirmed by the asymmetry of the frictional response between pulling and pushing of the edge.

Finally, in chapter 6 the dynamical response of the GNR against vertical pulling of one edge is studied. By a direct quantitative comparison between the outcome of the MD simulations and AFM measurements of the GNR detachment, it is shown that the vertical dynamics is dominated by the detachment of individual unit cells of the GNR accompanied by a stick-slip behavior of the tail. The complex interplay between these two effects gives rise to the observed double-periodicities of the vertical force traces within single periods.

Moreover, it is shown that the change of the relative strength between the corrugation and the adhesion of the interface, by artificially modifying the GNR/gold interaction strength or by changing their relative orientation can substantially affect the features of the detachment dynamics. In this context, an interface with larger corrugation may exhibit moiré related periodicities in the

vertical force profiles, due to the detachment of entire moiré supercells.

Future perspectives and developments of this work should involve the observation of the effects mentioned in this Thesis on new types of graphene/metal interfaces, which could be obtained by using a different metallic substrate, such as Ag(111), or by realizing a different GNR alignment, with the final aim of modifying the relative strength between corrugation and adhesion. Such experimental studies are expected to confirm the theoretical predictions of this Thesis, in particular the existence of moiré pattern features in the detachment dynamics.

The study of the GNR/gold interface, which is central in this Thesis, was carried out via MD simulations, with all its positives and drawbacks. From a theoretical point of view, the study of the frictional properties of this system could then serve as a benchmark for the application of more sophisticated techniques to address friction, such as machine-learning and clustering techniques, that do not need the resolution of the full "all-atom" Newtonian dynamics to obtain information about the steady state and the excited states of the system.

Appendices

Appendix A

Experimental and MD setup for GNR detachment

In this appendix, details about the MD simulations and the experiment that were carried out in chapter 6 are presented.

Experiment. All measurements were performed with a commercially available Omicron low-temperature scanning tunneling microscopy (STM)/atomic force microscopy (AFM) system, operating in ultra-high vacuum at 4.8 K. We used a tuning fork with a chemically-etched tungsten tip as a force sensor [182]. The resonance frequency and the mechanical quality factor are 23026 Hz and 19974, respectively. The high cantilever stiffness of 1800 N/m realizes a stable operation with a small amplitude of 43 pm [181]. The frequency shift, caused by the tip-sample interaction, was measured with a commercially available digital phase-locked loop (Nanonis: OC-4 and Zurich Instruments: HF2-LI and HF2-PLL) [180]. For the STM measurement, the bias voltage was applied to the tip while the sample was electronically grounded. The tungsten tip of a tuning fork sensor was sharpened *ex-situ* by focused ion beam milling technique and was then covered *in-situ* with Au atoms by contacting to the sample surface. A clean gold tip was formed *in situ* by indenting the Au sample surface and applying a pulse bias voltage between tip and sample several times. Clean Au(111) surfaces were prepared *in situ* by repeated cycles of standard Ar^+ sputtering (3×10^{-6} mbar, 1000 eV, and 15 min) and annealing at 750 K. As precursors to the GNRs synthesis, 10,10'-dibromo-9,9'-dianthryl molecules were deposited on the substrate from a Knudsen cell crucible, heated resistively at 135 °C. Subsequently, the samples were annealed at 200 °C and 400 °C to synthetize graphene nanoribbons on Au(111) [143, 144]. The STM topographic images were taken in constant current mode. Measured images were partially analyzed using the WSxM software [183].

Theoretical modeling. All MD simulations of detachment are performed using the LAMMPS package [184]. The GNR atoms and the two gold mobile layers obey a $T = 0$ dissipative Langevin dynamics, with a damping parameter $\gamma = 1.0\,\mathrm{ps}^{-1}$, which has been adjusted in order to highlight the stick-slip behavior of the GNR in the steady state. The force fields used to simulate the dynamics of the mobile gold layers and the GNR are the Embedded Atom Method (EAM) potential [185, 186] and the Adaptive Intermolecular Reactive Empirical Bond Order (AIREBO) potential [78] respectively.

The C-Au and the H-Au adhesive interactions are modelled with (6,12) LJ potentials of the form

$$V(r) = 4\epsilon \left[\left(\frac{\sigma}{r}\right)^{12} - \left(\frac{\sigma}{r}\right)^{6} \right] \tag{A.1}$$

We adopted $\epsilon = 8\,\mathrm{meV}$ for the C-Au interaction and $\epsilon = 3.2\,\mathrm{meV}$ for the H-Au interaction. The adhesive energy per C-atom that we obtain with these values of the LJ amplitudes for flat GNRs on gold is compatible with previous DFT estimates for graphene/metal interfaces [154, 155] and experimental results on graphite/graphite and graphene/silicon contacts [156, 157]. However, we tested that the qualitative features of the dynamics are not significantly affected by variations of the LJ parameters in a suitable range of values. These more realistic energies are larger than those adopted in previous work [34, 36, 37]. The adsorption distances for carbon and hydrogens is set by a common $\sigma = 0.342\,\mathrm{nm}$. This parametrization yields a good match between the shape of the experimental frequency shift profile and the simulated vertical force gradient for the R30 alignment (see Fig. 6.2b). The same parameters were also used for the simulation of detachment in the R0 alignment.

As discussed above, for the calculations reported in Fig. 6.6 the lateral corrugation was enhanced artificially by changing the value of σ to $0.274\,\mathrm{nm}$, while keeping all other parameters unchanged.

Chapter 8

Acknowledgements

First of all, I would like to thank my supervisors dott. Andrea Vanossi and prof. Erio Tosatti for having guided me all along my PhD project with patience and encouragement. It was a pleasure to work under their supervision in the Nanofriction group at SISSA, for the constant exchange of ideas that we always had and for the fruitful discussions that led us to the publication of the articles presented in this Thesis. I was always encouraged to take part to the group discussions and to constantly present my latest results, helping me to grow up a lot, both as a researcher and as a person. I also thank prof. Nicola Manini and dott. Roberto Guerra from Milan for the constant collaboration that we had throughout my PhD.

Finally, my special thanks go to my family, especially my parents Elisabetta and Franco, who always supported me with great effort during these years.

Bibliography

[1] A. Vanossi, N. Manini, M. Urbakh, S. Zapperi and E. Tosatti, *Modeling friction: from nanoscale to mesoscale* Rev. Mod. Phys., **85**, 2 (2013)

[2] N. Manini, G. Mistura, G. Paolicelli, E. Tosatti and A. Vanossi, *Current trends in the physics of nanoscale friction* Adv. Phys. X, **2**, 3, 569-590 (2017)

[3] B.N.J. Persson, *Sliding friction - Physical principles and applications* Springer, Berlin (1998)

[4] B.N.J. Persson and E. Tosatti, *Physics of sliding friction* Springer Science & Business Media (1996)

[5] N. Manini, O. M. Braun, E. Tosatti, R. Guerra and A. Vanossi, *Friction and nonlinear dynamics* J. Phys. Cond. Mat., **28**, 293001 (2016)

[6] E. Gnecco and E. Meyer, *Fundamentals of Friction and Wear on the Nanoscale - Second Edition* Springer, NanoScience and Technology, Switzerland (2015)

[7] G. Binnig, C. F. Quate and Ch. Gerber, *Atomic Force Microscope* Phys. Rev. Lett., **56**, 9 (1986)

[8] R. Buzio, A. Gerbi, S. Uttiya, C. Bernini, A. E. Del Rio Castillo, F. Palazon, A. S. Siri, V. Pellegrini, L. Pellegrino and F. Bonaccorso, *Ultralow friction of ink-jet printed graphene flakes* Nanoscale, **9**, 7612-7624 (2017)

[9] J. S. Choi, J. S. Kim, I.-S. Byun, D. H. Lee, M. J. Lee, B. H. Park, C. Lee, D. Yoon, H. Cheong, K. H. Lee, Y.-W. Son, J. Y. Park and M. Salmeron, *Friction Anisotropy-Driven Domain Imaging on Exfoliated Monolayer Graphene* Science, **333**, 607-610 (2011)

[10] C. Lee, Q. Li, W. Kalb, X.-Z. Liu, H. Berger, R. W. Carpick and J. Hone, *Frictional Characteristics of Atomically Thin Sheets* Science, **328**, 76-80 (2010)

[11] M. B. Elinski, B. D. Menard, Z. Liu and J. D. Batteas, *Adhesion and Friction at Graphene/Self-Assembled Monolayer Interfaces investigated by Atomic Force Microscopy* J. Phys. Chem. C, **121**, 10 (2017)

[12] D. Frenkel, B. Smit, *Understanding Molecular Simulations (2nd Edition)* Academic Press, Orlando (2001)

[13] M. H. Müser, M. Ferrario, G. Ciccotti, K. Binder *Computer Simulations in Condensed Matter Systems: from Materials to Chemical Biology - Vol. 2* Springer, Heidelberg (2006)

[14] O. M. Braun, Y. S. Kivshar, *Nonlinear dynamics of the Frenkel-Kontorova model* Phys. Rep., **306**, 1-108 (1998)

[15] L. Prandtl, Z. Angew. Math. Mech., **8**, 85 (1928)

[16] G. A. Tomlinson, Philos. Mag., **7**, 5 (1929)

[17] V. L. Popov and J. A. T. Gray, *Prandtl-Tomlinson model: History and applications in friction, plasticity and nanotechnlogies* Jour. Appl. Math. and Mech., **92**, 9 (2012)

[18] J. Frenkel and T. Kontorova, Phys. Z. Sowjetunion, **13**, 1 (1938)

[19] A. Vanossi, J. Röder, A. R. Bishop and V. Bortolani, *Underdamped commensurate dynamics in a driven Frenkel-Kontorova-type model* Phys. Rev. E Stat. Nonlin. Soft Matter Phys., **67**, 016605 (2003)

[20] R. Guerra, A. Vanossi, and M. Ferrario, *Nonlinear mobility of a driven system: temperature and disorder effects* Surf. Sci., **601**, 3676 (2007)

[21] M. Urbakh, J. Klafter, D. Gourdon and J. Israelachvili, *The nonlinear nature of friction* Nature, **430**, 525-528 (2004)

[22] V. Bormuth, V. Varga, J. Howard and E. Schäffer, *Protein Friction Limits Diffusive and Directed Movements of Kinesin Motors on Microtubules* Science, **325**, 870 (2009)

[23] T. Filleter, J. McChesney, A. Bostwick, E. Rotenberg, K. Emstev, T. Seyller, K. Horn and R. Bennewitz, *Friction and Dissipation in Epitaxial Graphene Films*, Phys. Rev. Lett., **102**, 086102 (2009)

[24] H. Lee, N. Lee, Y. Seo, J. Eom and S. Lee, *Comparison of frictional forces on graphene and graphite* Nanotechnology, **20**, 32 (2009)

[25] W. K. Kim and M. L. Falk, *Role of intermediate states in low-velocity friction between amorphous surfaces* Phys. Rev. B, **84**, 165422 (2011)

[26] T. Bohlein, J. Mikhael and C. Bechinger, *Observation of kinks and antikinks in colloidal monolayers driven across ordered surfaces* Nature Mater., **11**, 126-130 (2012)

[27] M. P. N. Juniper, A. V. Straube, R. Besseling, D. Aarts and R. Dullens, *Microscopic dynamics of synchronization in driven colloids* Nature Comm., **6**, 7187 (2015)

[28] P. Egberts, G. H. Han, X. Z. Liu, A. T. C. Johnson and R. W. Carpick, *Frictional Behavior of Atomically Thin Sheets: Hexagonal-Shaped Graphene Islands Grown on Copper by Chemical Vapor Deposition* ACS Nano, **8**, 5010-5021 (2014)

[29] G. Paolicelli, M. Tripathi, V. Corradini, A. Candini and S. Valeri, *Nanoscale frictional behavior of graphene on SiO2 and Ni(111) substrates* Nanotechnology, **26**, 5 (2015)

[30] M. Tripathi, F. Awaja, G. Paolicelli, R. Bartali, E. Iacob, S. Valeri, S. Ryu, S. Signetti, G. Speranza and N. M. Pugno, *Tribological characteristics of few-layer graphene over Ni grain and interface boundaries* Nanoscale, **8**, 12 (2016)

[31] C. Lee, Q. Li, W. Kalb, X.-Z. Liu, H. Berger, R. W. Carpick and J. Hone, *Frictional characteristics of atomically thin sheets* Science, **328**, 5974 (2010)

[32] M. Dienwiebel and R. Bennewitz, *Fundamentals of Friction and Wear on the Nanoscale, 2nd Edition* Springer, Berlin (2015)

[33] W. Gao and A. Tkatchenko, *Adhesion-dependent negative friction coefficient on chemically modified graphite at the nanoscale* Phys. Rev. Lett., **114**, 096101 (2016)

[34] S. Kawai, A. Benassi, E. Gnecco, H. Söde, R. Pawlak, X. Feng, K. Müellen, D. Passerone, C. Pignedoli, P. Ruffieux, R. Fasel and E. Meyer, *Superlubricity of graphene nanoribbons on gold surfaces* Science, **351**, 6276 (2016)

[35] S. Kawai, M. Koch, E. Gnecco, A. Sadeghi, R. Pawlak, T. Glatzel, J. Schwartz, S. Gödecker,

S. Hecht, A. Baratoff, L. Grill and E. Meyer, *Quantifying the atomic level mechanics of single long physisorbed molecular chains* PNAS, **111**, 11, 3968-3972 (2014)

[36] L. Gigli, N. Manini, A. Benassi, E. Tosatti, A. Vanossi and R. Guerra, *Graphene nanoribbons on gold: understanding superlubricity and edge effects* 2D Mat., **4**, 4 (2017)

[37] L. Gigli, N. Manini, E. Tosatti, R. Guerra and A. Vanossi, *Lifted graphene nanoribbons on gold: from smooth sliding to multiple stick-slip regimes* Nanoscale, **4**, 2073-2080 (2018)

[38] Ian M. Hutchings, *Leonardo da Vinci's studies of friction* Elsevier, Wear, Volume 360-361, 51-66 (2016)

[39] D. Dowson, *History of Tribology - Second Edition* Longman, London (1998)

[40] Y. Desplanques, *Amontons-Coulomb Friction Laws, A Review of the Original Manuscript* SAE Int. J. Mater. Manf., **8**, 1, 98-103 (2015)

[41] F. P. Bowden and D. Tabor, *The area of contact between stationary and moving surfaces* Proc. R. Soc. Lond. A, **169**, 391 (1939)

[42] S.Y. Krylov and J.W.M. Frenken, *The physics of atomic-scale friction: Basic considerations and open questions* Phys. Stat. Solid. B, **251**, 4, 711-736 (2014)

[43] T. Baumberger, P. Berthoud and C. Caroli, *Physical analysis of the state- and rate-dependent friction law. II. Dynamic friction.* Physical Review B, **60**, 3928 (1999)

[44] J. N. Israelachvili, *Adhesion forces between surfaces in liquids and condensable vapours* Surf. Sci. Rep., **14**, 109 (1992)

[45] M. Ruths, S. A. Sukhishvili and S. Granick, *Static and Dynamic Forces between Adsorbed Polyelectrolyte Layers (Quaternized Poly-4-vinylpyridine)* J. Phys. Chem. B, **105**, 6202-6210 (2001)

[46] J. Klein, D. Perahia and S. Warburg, *Forces between polymer-bearing surfaces undergoing shear* Nature, **352**, 143-145 (1991)

[47] E. Riedo, E. Gnecco, R. Bennewitz, E. Meyer and H. Brune, *Interaction Potential and Hopping Dynamics Governing Sliding Friction* Phys. Rev. Lett., **91**, 084502 (2003)

[48] E. Gnecco, R. Bennewitz, T. Gyalog, Ch. Loppacher, M. Bammerlin, E. Meyer, and H.-J. Güntherodt, *Velocity Dependence of Atomic Friction* Phys. Rev. Lett., **84**, 1172 (2000)

[49] A. Schirmeisen, L. Jansen, H. Hölscher, and H. Fuchs, *Temperature dependence of point contact friction on silicon* Appl. Phys. Lett., **88**, 123108 (2006)

[50] X. Zhao, S. R. Phillpot, W. G. Sawyer, S. B. Sinnott and S. S. Perry, *Transition from thermal to athermal friction under cryogenic conditions* Phys. Rev. Lett., **102**, 186102 (2009)

[51] Z. Tshiprut, S. Zelner and M. Urbakh, *Temperature-Induced Enhancement of Nanoscale Friction* Phys. Rev. Lett., **102**, 136102 (2009)

[52] O. Y. Fayardo and J. J. Mazo, *Effects of surface disorder and temperature on atomic friction* Phys. Rev. B, **82**, 035435 (2010)

[53] P.E. Sheehan and C.M. Lieber, *Nanotribology and nanofabrication of MoO_3 structures by atomic force microscopy* Science, **272**, 1158-1161 (1996)

[54] C. Ritter, M. Heyde, B. Stegeman, K. Rademann and U.D. Schwarz, *Contact-area dependence of frictional forces: Moving adsorbed antimony nanoparticles* Phys. Rev. B, **71**, 085405 (2005)

[55] D. Dietzel, C. Ritter, T. Mönninghoff, H. Fuchs, A. Schirmeisen and U.D. Schwarz, *Frictional*

Duality Observed during Nanoparticle Sliding Phys. Rev. Lett., **101**, 125505 (2008)

[56] D. Dietzel, M. Feldmann, U.D. Schwarz, H. Fuchs, and A. Schirmeisen, *Scaling Laws of Structural Lubricity* Phys. Rev. Lett., **111**, 235502 (2013)

[57] E. Cihan, S. Ipek, E. Durgun and M.Z. Baykara, *Structural lubricity under ambient conditions* Nature Comm., **7**, 12055 (2016)

[58] M. H. Müser, L. Wenning, and M. O. Robbins, *Simple Microscopic Theory of Amontons's Laws for Static Friction* Phys. Rev. Lett., **86**, 1295 (2001)

[59] Y. Shibuta and J. A. Elliott, *Interaction between two graphene sheets with a turbostratic orientational relationship* Chem. Phys. Lett., **512**, 146-150 (2011)

[60] A. S. de Wijn, C. Fusco and A. Fasolino, *Stability of Superlubric Sliding on Graphite* Phys. Rev. E, **81**, 046105 (2010)

[61] S. Medyanik, W.K. Liu, I.-H. Sung and R.W. Carpick, *Predictions and Observations of Multiple Slip Modes in Atomic-Scale Friction* Phys. Rev. Lett., **97**, 136106 (2006)

[62] A. Socoliuc, R. Bennewitz, E. Gnecco and E. Meyer, *Transition from Stick-Slip to Continuous Sliding in Atomic Friction: Entering a New Regime of Ultralow Friction* Phys. Rev. Lett., **92**, 134301 (2004)

[63] S. Y. Krylov, K. B. Jinesh, H. Valk, M. Dienwiebel and J. W. M. Frenken, *Thermally induced suppression of friction at the atomic scale* Phys. Rev. E, **71**, 065101 (2005)

[64] F. Pellegrini, E. Panizon, G. Santoro and E. Tosatti, *Thermolubricity and the Jarzynski equality* arXiv:1809.01609 [cond-mat.stat-mech] (2018)

[65] Y. Sang, M. Dubè and M. Grant, *Thermal Effects on Atomic Friction* Phys. Rev. Lett., **87**, 174301 (2001)

[66] S. C. Ying, *Structure and Dynamics of a Submonolayer Film Adsorbed on Solid Surfaces* Phys. Rev. B, **3**, 4160 (1971)

[67] J. B. Sokoloff, *Sliding charge-density waves in periodic and disordered lattices* Phys. Rev. B, **16**, 3367 (1977)

[68] S. Aubry and P.Y. Le Daeron, *The discrete Frenkel-Kontorova model and its extensions: I. Exact results for the ground-states* Phys. D: Nonlinear phenomena, **8**, 3 (1983)

[69] S. Aubry, *Solitons and Condensed Matter Physics* Springer series in solid state sciences, **8**, 264-277 (1978)

[70] L. M. Floria and J. J. Mazo, *The pulled Frenkel-Kontorova chain* Adv. Phys., **45**, 505 (1996)

[71] M. Paliy, O. M. Braun, T. Dauxois and B. Hu, *Dynamical phase diagram of the dc-driven underdamped Frenkel-Kontorova chain* Phys. Rev. E, **56**, 4025 (1997)

[72] D. Mandelli, A. Vanossi, M. Invernizzi, S. V. Paronuzzi, N. Manini and E. Tosatti, *Superlubric-pinned transition in sliding incommensurate colloidal monolayers* Phys. Rev. B, **92**, 134306 (2015)

[73] T. Brazda, A. Silva, N. Manini, A. Vanossi, R. Guerra, E. Tosatti and C. Bechinger, *Experimental Observation of the Aubry Transition in Two-Dimensional Colloidal Monolayers* Phys. Rev. X, **8**, 011050 (2018)

[74] R. Car and M. Parrinello, *Unified Approach for Molecular Dynamics and Density-Functional Theory* Phys. Rev. Lett., **55**, 2471 (1985)

[75] R. Guerra, E. Tosatti and A. Vanossi, *Slider thickness promotes lubricity: from 2D islands to the 3D clusters* Nanoscale, **8**, 21, 11108-11113 (2016)

[76] M. S. Daw, S. M. Foiles and M. I. Baskes, *the embedded-atom method: a review of theory and applications* Mat. Sci. Rep., **9**, 7-8, 251-310 (1993)

[77] L.-F. Wang, X. Shu, G.-H. Lu and F. Gao, *Embedded-atom method potential for modeling hydrogen and hydrogen-defect interaction in tungsten* J. Phys. Cond. Mat., **29**, 453401 (2017)

[78] D. W. Brenner, O. A. Shenderova, J. A. Harrison, S. J. Stuart, B. Ni and S. B. Sinnott, *A second-generation reactive empirical bond order (REBO) potential energy expression for hydrocarbons* J. Phys. Cond. Mat., **14**, 783-802 (2002)

[79] A. C. T. van Duin, S. Dasgupta, F. Loranta and W. A. Goddard, *ReaxFF: A Reactive Force Field for Hydrocarbons* J. Phys. Chem. A, **105**, 9396 (2001)

[80] G. Bussi, D. Donadio and M. Parrinello, *Canonical sampling through velocity-rescaling* Jour. Chem. Phys., **126**, 014101 (2007)

[81] D. J. Evans and B. L. Holian, *The Nosè-Hoover thermostat* Jour. Chem. Phys., **83**, 4069 (1985)

[82] G. Bussi and M. Parrinello, *Accurate sampling using Langevin dynamics* Phys. Rev. E, **75**, 056707 (2007)

[83] P. A. Thompson and M. O. Robbins, *Origin of stick-slip motion in boundary lubrication* Science, **250**, 4982, 792-794 (1990)

[84] M. O. Robbins and P. A. Thompson, *Critical velocity of stick-slip motion* Science, **253**, 916 (1991)

[85] M. J. Stevens and M. O. Robbins, *Simulations of shear-induced melting and ordering* Phys. Rev. E, **48**, 3778-3792 (1993)

[86] M. Cieplak, E. D. Smith and M. O. Robbins, *Molecular origins of friction: the force on adsorbed layers* Science, **265**, 5176 (1994)

[87] P. A. Thompson, M. O. Robbins and G. S. Grest, *Structure and shear response in Nanometer-thick films* Isr. Jour. of Chemistry, **35**, 1 (1995)

[88] A. Benassi, A. Vanossi, G. E. Santoro and E. Tosatti, *Parameter-free dissipation in simulated sliding friction* Phys. Rev. B, **82**, 081401 (2010)

[89] A. Benassi, A. Vanossi, G. E. Santoro and E. Tosatti, *Optimal energy dissipation in sliding friction simulations* Tribol. Lett., **48**, 41 (2012)

[90] L. Kantorovich and N. Rompotis, *Generalised Langevin Equation for solids: II. Stochastic Boundary Conditions for non-equilibrium molecular dynamics simulations.* Phys. Rev. B, **78**, 094305 (2008).

[91] L. Stella, C. D. Lorenz, and L. Kantorovich, *Generalized Langevin equation: An efficient approach to nonequilibrium molecular dynamics of open systems* Phys. Rev. B, **89**, 134303 (2014).

[92] H. Ness, L. Stella, C. D. Lorenz, and L. Kantorovich, *Applications of the generalized Langevin equation: Towards a realistic description of the baths* Phys. Rev. B, **91**, 014301 (2015).

[93] H. Ness, A. Genina, L. Stella, C.D. Lorenz, and L. Kantorovich, *Nonequilibrium processes from generalized Langevin equations: Realistic nanoscale systems connected to two thermal*

baths Phys. Rev. B, **93**, 174303 (2016).

[94] J. Krim, D. H. Solina and R. Chiarello *Nanotribology of a Kr monolayer: A Quartz-Crystal Microbalance Study of Atomic-Scale Friction* Phys. Rev. Lett., **91**, 66 (1991)

[95] J. Krim, *QCM tribology studies of thin adsorbed films* Nano Today, Elsevier, **2**, 5 (2007)

[96] E. D. Smith and M. O. Robbins, *Friction on adsorbed monolayers* Phys. Rev. B, **54**, 11 (1996)

[97] P. A. Thompson and M. O. Robbins, *Shear flow near solids: Epitaxial order and flow boundary conditions* Phys. Rev. A, **41**, 6830 (1990)

[98] W. A. Steele, *The physical interaction of gases with crystalline solids. I. Gas-solid energies and properties of isolated absorbed atoms* Surf. Sci., **36**, 317-352 (1973)

[99] C. K. Majumdar and I. Ramarao, *Critical parameters of a Lennard-Jones gas* Phys. Rev. A, **14**, 1452 (1976)

[100] B. N. J. Persson, *Theory of friction and boundary lubrication* Phys. Rev. B, **48**, 18140-18158 (1993)

[101] B. N. J. Persson, *Theory and Simulation of Sliding Friction* Phys. Rev. Lett., **71**, 1212-1215 (1993)

[102] A. Liebsch, S. Gonçalves and M. Kiwi, *Electronic vs. Phononic Friction of Xenon on Silver* Phys. Rev. B, **60**, 5034-5043 (1999)

[103] M. S. Tomassone, J. B. Sokoloff, A. Widom and J. Krim, *Dominance of Phonon Friction for a Xenon Film on a Silver (111) Surface* Phys. Rev. Lett., **79**, 4798-4801 (1997)

[104] N. Varini, A. Vanossi, R. Guerra, D. Mandelli, R. Capozza and E. Tosatti, *Static friction scaling of physisorbed islands: the key is the edge* Nanoscale, **7**, 2093-2110 (2015)

[105] M. O. Robbins and M. H. Müser, *Computer simulations of friction, lubrication and wear* Modern Tribology Handbook I, CRC Press, Boca Raton, 715-765 (2001)

[106] M. R. Sørensen, K. W. Jacobsen and P. Stolze, *Simulations of atomic-scale sliding friction* Phys. Rev. B, **53**, 2101-2113 (1996)

[107] K. W. Jacobsen, J. K. Norskov and M. J. Puska, *Interatomic interactions in the effective-medium theory* Phys. Rev. B, **35**, 7423-7442 (1987)

[108] F. P. Bowden and D. Tabor, *The Friction and Lubrication of Solids* Oxford University, New York (1950)

[109] U. Tartaglino, T. Zykova-Timan, F. Ercolessi and E. Tosatti, *Melting and Nonmelting of solid surfaces and nanosystems* Phys. Rep., **411**, 291 (2005)

[110] L. Kuipers and J. W. M. Frenken, *Jump to Contact, Neck Formation and Surface Melting in the Scanning Tunneling Microscope* Phys. Rev. Lett., **70**, 3907 (1993)

[111] T. Zykova-Timan, D. Ceresoli and E. Tosatti, *Peak Effect versus Skating in High Temperature Nanofriction* Nature Mat., **6**, 230 (2007)

[112] R. Guerra, U. Tartaglino, A. Vanossi and E. Tosatti, *Ballistic nanofriction* Nature Mat., **9**, 634-637 (2010)

[113] R. W. Carpick and M. Salmeron, *Scratching the Surface: Fundamental Investigations of Tribology with Atomic Force Microscopy* Chem. Rev., **97**, 4 (1997)

[114] S. Fujisawa, Y. Sugawara, S. Ito, S. Mishima, T. Okada and S. Morita, *The two-dimensional*

stick-slip phenomenon with atomic resolution Nanotechnology, **4**, 138-142 (1993)

[115] C. M. Mate, G. M. McClelland, R. Erlandsson and S. Chiang *Atomic-scale friction of a tungsten tip on a graphite surface* Phys. Rev. Lett., **59**, 1942 (1987)

[116] H. Bluhm, U. D. Schwarz, K.-P. Meyer and R. Wiesendanger, *Anisotropy of sliding friction on the tryglicine sulfate (010) surface* Appl. Phys. A, **61**, 5 (1995)

[117] C. Yu and Q. J. Wang, *Friction Anisotropy with Respect to Topographic Orientation* Sci. Rep., **2**, 988 (2012)

[118] P. Frantz, N. Agrait and M. Salmeron, *Use of Capacitance to Measure Surface Forces. 1. Measuring Distance of Separation with Enhanced Spatial and Time Resolution* Langmuir, **12**, 3289-3294 (1996)

[119] J. Klein and E. Kumacheva, *Simple liquids confined to molecularly thin layers. I. Confinement-induced liquid-to-solid phase transitions* Jour. Chem. Phys., **108**, 6996 (1998)

[120] A. L. Damirel and S. Granick, *Glasslike Transition of a Confined Simple Fluid* Phys. Rev. Lett., **77**, 2261 (1996)

[121] Y. Zhu and S. Granick, *Rate-Dependent Slip of Newtonian Liquid at Smooth Surfaces* Phys. Rev. Lett., **87**, 096105 (2001)

[122] J. Y. Park and M . Salmeron, *Fundamental Aspects of Energy Dissipation in Friction* Chem. Rev., **114**, 1, 677–711 (2014)

[123] M. Hirano and K. Shinjo, *Atomistic locking and friction* Phys. Rev. B, **41**, 11837 (1990)

[124] M. Hirano, K. Shinjo, R. Kaneko, and Y. Murata, *Anisotropy of frictional forces in muscovite mica* Phys. Rev. Lett., **67**, 2642 (1991)

[125] M. Z. Baykara, M. R. Vazirisereshk, and A. Martini, *Emerging superlubricity: A review of the state of the art and perspectives on future research* Appl. Phys. Rev. **5**, 041102 (2018).

[126] M. Dienwiebel, G. S. Verhoeven, N. Pradeep, J. W. M. Frenken, J. A. Heimberg, and H. W. Zandbergen, *Superlubricity of graphite* Phys. Rev. Lett., **92**, 126101 (2004)

[127] X. Feng, S. Kwon, J. Y. Park and M. Salmeron, *Superlubric sliding of graphene nanoflakes on graphene* ACS Nano, **7**, 1718-1724 (2013)

[128] A. Franchini, V. Bortolani, G. Santoro and M. Brigazzi, *Thermal effects in static friction: thermolubricity* Phys. Rev. E Stat. Nonlin. Soft Matter Phys., **78**, 046107 (2008)

[129] Y. Dong, H. Gao and A. Martini, *Suppression of atomic friction under cryogenic conditions: The role of athermal instability in AFM measurements* Europhys. Lett., **98**, 1 (2012)

[130] Y. Zhang, M. Dong, B. Gueye, Z. Ni, Y. Wang and Y. Chen, *Temperature effects on the friction characteristics of graphene* Appl. Phys. Lett., **107**, 011601 (2015)

[131] S. Y. Krylov and J. W. M. Frenken, *Superlubricity of dry nanocontacts* New J.. Phys., **9**, 398 (2007)

[132] L. Bardotti, P. Jensen, A. Hoareau, M. Treilleux, B. Cabaud, A. Perez and F. Cadete Santos Aires, *Diffusion and aggregation of large antimony and gold clusters deposited on graphite* Surf. Sci., **367**, 3, 276-292 (1996)

[133] K. Mougin, E. Gnecco, A. Rao, M. T. Cuberes, S. Jayaraman, E. W. McFarland, H. Haidara and E. Meyer, *Manipulation of Gold Nanoparticles: Influence of Surface Chemistry, Temperature, and Environment (Vacuum versus Ambient Atmosphere)* Langmuir, **24**, 1577 (2008)

[134] G. Paolicelli, K. Mougin, A. Vanossi and S. Valeri, *Adhesion detachment and movement of gold nanoclusters induced by dynamic atomic force microscopy* Nanotechnology, **20**, 11 (2008)

[135] G. Paolicelli, M. Rovatti, A. Vanossi and S. Valeri, *Controlling single cluster dynamics at the nanoscale* Appl. Phys. Lett., **95**, 143121 (2009)

[136] A. Schirmeisen and U. D. Schwarz, *Measuring the friction of nanoparticles: a new route towards a better understanding of nanoscale friction* ChemPhysChem., **10**, 2373 (2009)

[137] D. Dietzel, M. Feldmann, C. Herding, U. D. Schwarz and A. Schirmeisen, *Quantifying Pathways and Friction of Nanoparticles during controlled manipulation by Contact-Mode Atomic Force Microscopy* Tribol. Lett., **39**, 273-281 (2010)

[138] J. Brndiar, R. Turanský, D. Dietzel, A. Schirmeisen and I. Štich, *Understanding frictional duality and bi-duality: Sb-nanoparticles on HOPG* Nanotechnology, **22**, 8 (2011)

[139] W. D. Luedtke and U. Landman, *Slip Diffusion and Lévy Flights of an Adsorbed Gold Nanocluster* Phys. Rev. Lett., **82**, 3835 (1999)

[140] L. J. Lewis, P. Jensen, N. Combe and J-L. Barrat, *Diffusion of gold nanoclusters on graphite* Phys. Rev. B, **61**, 16084 (2000)

[141] Y. Maruyama, *Temperature dependence of Lévy-type stick-slip diffusion of a gold nanocluster on graphite* Phys. Rev. B **69**, 245408 (2004)

[142] A. Erdemir and J.-M. Martin, *Superlubricity* Elsevier, Amsterdam (2007)

[143] P. Ruffieux, S. Wang, B. Yang, C. Sánchez-Sánchez , J. Liu, T. Dienel, L. Talirz, P. Shinde, C. A. Pignedoli, D. Passerone, T. Dumslaff, X. Feng, K. Müllen and R. Fasel, *On-surface synthesis of graphene nanoribbons with zigzag edge topology* Nature, **531**, 489 (2016)

[144] R. M. Jacobberger, B. Kiraly, M. Fortin-Deschenes, P. L. Levesque, K. M. McElhinny, G. J. Brady, R. Rojas Delgado, S. Singha Roy, A. Mannix, M. G. Lagally, P. G. Evans, P. Desjardins, R. Martel, M. C. Hersam, N. P. Guisinger and M. S. Arnold, *Direct oriented growth of armchair graphene nanoribbons on germanium* Nature Comm., **6**, 8006 (2015)

[145] A. D. Novaco and J. P. McTague, *Orientational Epitaxy—the Orientational Ordering of Incommensurate Structures* Phys. Rev. Lett., **38**, 1286 (1977)

[146] F. Grey and J. Bohr, *A Symmetry Principle for Epitaxial Rotation* Europhys. Lett., **18**, 717 (1992)

[147] Ch. Wöll, S. Chiang, R. J. Wilson and P. H. Lippel, *Determination of atom positions at stacking-fault dislocations on Au(111) by scanning tunneling microscopy* Phys. Rev. B, **39**, 7988 (1989)

[148] J. V. Barth, H. Brune, G. Ertl, and R. J. Behm, *Scanning tunneling microscopy observations on the reconstructed Au(111) surface: Atomic structure, long-range superstructure, rotational domains, and surface defects* Phys. Rev. B, **42**, 9307 (1990)

[149] D. Fujita, K. Amemiya, T. Yakabe, H. Nejoh, T. Sato, and M. Iwatsuki, *Anisotropic Standing-Wave Formation on an Au(111)- (*$23 \times \sqrt{(}3$*) Reconstructed Surface* Phys. Rev. Lett., **78**, 3904 (1997)

[150] J. M. Wofford, E. Starodub, A. L. Walter, S. Nie, A. Bostwick, N. C. Bartelt, K. Thürmer, E. Rotenberg, K. F. McCarty and O. D. Dubon, *Extraordinary epitaxial alignment of graphene islands on Au(111)* New J. Phys., **14** (2012)

[151] S. Nie, N. C. Bartelt, J. M. Wofford, O. D. Dubon, K. F. McCarty and K. Thürmer, *Scan-*

ning tunneling microscopy study of graphene on Au(111): Growth mechanisms and substrate interactions Phys. Rev. B, **85**, 205406 (2012)

[152] M. Ma, A. Benassi, A. Vanossi and M. Urbakh, *Critical Length Limiting Superlow Friction* Phys. Rev. Lett., **114**, 055501 (2015)

[153] Y. Li, W. Zhang, M. Morgenstern and R. Mazzarello, *Electronic and magnetic properties of zigzag graphene nanoribbons on the (111) surface of Cu, Ag and Au* Phys. Rev. Lett., **110**, 216804 (2013)

[154] G. Giovannetti, P. A. Khomyakov, G. Brocks, V. M. Karpan, J. van den Brink, and P. J. Kelly, *Doping graphene with metal contacts* Phys. Rev. Lett., **101**, 026803 (2008)

[155] M. Vanin, J. J. Mortensen, K. A. Kelkkanen, J. M. García Lastra, K. S. Thygesen and K. W. Jacobsen, *Graphene on metals: A van der Waals density functional study* Phys. Rev. B, **81**, 081408 (2010)

[156] E. Koren, E. Lörtscher, C. Rawlings, A. W. Knoll and U. Duerig, *Adhesion and friction in mesoscopic graphite contacts* Science 348, **6235** (2015)

[157] Z. Zong, C.-L. Chen, M. R. Dokmeci and K. Wan, *Direct measurement of graphene adhesion on silicon surface by intercalation of nanoparticles* J. Appl. Phys., **107**, 026104 (2010)

[158] I. Leven, T. Maaravi, I. Azuri, L. Kronik and O. Hod, *Interlayer Potential for Graphene/h-BN Heterostructures* J. Chem. Theo. Comput., **12**, 6 (2016)

[159] S. Plimpton, *Fast Parallel Algorithms for Short-Range Molecular Dynamics* J. Comp. Phys., **117**, 1 (1995)

[160] A. Vanossi, N. Manini, G. Divitini, G.E. Santoro and E. Tosatti, *Exactly Quantized Dynamics of Classical Incommensurate Sliders* Phys. Rev. Lett., **97**, 056101 (2006)

[161] M. Yankowitz, J. Xue, D. Cormode, J.D. Sanchez-Yamagishi, K. Watanabe, T. Taniguchi, P. Jarillo-Herrero, P. Jacquod and B.J. LeRoy, *Emergence of superlattice Dirac points in graphene on hexagonal boron nitride* Nature Phys., **8**, 382–386 (2012)

[162] E. Koren and U. Duerig, *Superlubricity in quasicrystalline twisted bilayer graphene* Phys. Rev. B, **93**, 201404 (2016)

[163] E. Koren and U. Duerig, *Moiré scaling of the sliding force in twisted bilayer graphene* Phys. Rev. B, **94**, 045401 (2016)

[164] O. M. Braun and Y. S. Kivshar, *The Frenkel-Kontorova Model: Concepts, Methods, and Applications* Springer, Berlin (2004)

[165] M. Cesaratto, N. Manini, A. Vanossi, E. Tosatti, and G. E. Santoro, *Kink plateau dynamics in finite-size lubricant chains* Surf. Sci., **601**, 3682 (2007)

[166] M. Pierno, L. Bruschi, G. Mistura, G. Paolicelli, A. Di Bona, S. Valeri, R. Guerra, A. Vanossi and E.Tosatti, *Frictional transition from superlubric islands to pinned monolayers* Nature Nanotech., **10**, 8 (2015)

[167] E. Tentori, *Energetica di un nastro di grafene nanoscopico depositato su Au(111), al variare di posizione e allineamento angolare* University Milan, `http://materia.fisica.unimi.it/manini/theses/tentori.pdf`

[168] J. Cai, P. Ruffieux, R. Jaafar, M. Bieri, T. Braun, S. Blankenburg, M. Muoth, A.P. Seitsonen, M. Saleh, X. Feng, K. Müllen and R. Fasel, *Atomically precise bottom-up fabrication of graphene nanoribbons* Nature, **466**, 470–473 (2010)

[169] J. Krim, *Friction and energy dissipation mechanisms in adsorbed molecules and molecularly thin films* Adv. Phys., **61**, 155-323 (2012)

[170] Z. Guo, T. Chang, X. Guo and H. Gao, *Gas-like adhesion of two dimensional materials onto solid surfaces* Sci. Rep., **7**, 159 (2017)

[171] J. G. Vilhena, E. Gnecco, R. Pawlak, F. Moreno-Herrero, E. Meyer and R. Perez, *Stick-slip motion of ssDNA over graphene* J. Phys. Chem. B, **122**, 2 (2018)

[172] Z. Cao and A.V. Dobrynin, *Contact mechanics of nanoparticles: pulling rigid nanoparticles from soft, polymeric surfaces* Langmuir, **31**, 45 (2015)

[173] R. Pawlak, W. Ouyang, A. E. Filippov, L. Kalikhman-Razvozov, S. Kawai, T. Glatzel, E. Gnecco, A. Baratoff, Q.-S. Zheng, O. Hod, M. Urbakh and E. Meyer, *Single Molecule Tribology: Force Microscopy Manipulation of a Porphyrin Derivative on a Copper Surface* ACS Nano, **10**, 713-722 (2016)

[174] R. Pawlak, S. Kawai, T. Meier, T. Glatzel, A. Baratoff and E. Meyer, *Single-molecule manipulation experiments to explore friction and adhesion* J. Phys. D: Appl. Phys., **50**, 113003 (2017)

[175] A. Vanossi, D. Dietzel, A. Schirmeisen, E. Meyer, R. Pawlak, T. Glatzel, M. Kisiel, S. Kawai and N. Manini, *Recent highlights in nanoscale and mesoscale friction* Beilstein J. Nanotech., **9**, 1995 (2018)

[176] W. Ouyang, D. Mandelli, M. Urbakh and O. Hod, *Nanoserpents: Graphene Nanoribbons Motion on Two-Dimensional Hexagonal Materials*, arXiv:1806.09555 [cond-mat.mes-hall] (2018)

[177] M. Miskin, C. Sun, I. Cohen, W. R. Dichtel and P. L. McEuen, *Measuring and Manipulating the Adhesion of Graphene* Nano. Lett., **18**, 449-454 (2018)

[178] M. Koch, Z. Li, C. Nacci, T. Kumagai, I. Franco and L. Grill, *How Structural Defects Affect the Mechanical and Electrical Properties of Single Molecular Wires* Phys. Rev. Lett., **121**, 047701 (2018)

[179] L. Talirz, P. Ruffieux and R. Fasel, *On surface synthesis of atomically precise graphene nanoribbons* Adv. Mat., **28**, 6222 (2016)

[180] T. R. Albrecht, P. Grütter, D. Horne and D. Rugar, *Frequency modulation detection using high-Q cantilevers for enhanced force microscope sensitivity* J. Appl. Phys., **69**, 668 (1991)

[181] F. J. Giessibl, *Advances in atomic force microscopy* Rev. Mod. Phys., **75**, 949-983 (2003)

[182] F. J. Giessibl, *High-speed force sensor for force microscopy and profilometry utilizing a quartz tuning fork* Appl. Phys. Lett., **73**, 3956 (1998)

[183] I. Horcas, R. Fernandez, J.M. Gomez-Rodriguez, J. Colchero, J. Gomez-Herrero and A.M. Baro, *WSXM: A software for scanning probe microscopy and a tool for nanotechnology* Rev. Sci. Instrum., **78**, 013705 (2007)

[184] S. Plimpton, *Fast Parallel Algorithms for Short-Range Molecular Dynamics* J. Comput. Phys., **117**, 1 (1995)

[185] M. S. Daw and M. I. Baskes, *Embedded-atom method: Derivation and application to impurities, surfaces, and other defects in metals* Phys. Rev. B, **29**, 6443 (1984)

[186] M. W. Finnis and J. E. Sinclair, *A simple empirical N-body potential for transition metals* Phyl. Mag. A, **50**, 45 (1984)